

**JOURNAL OF RESEARCH of the National Bureau of Standards**  
**Vol. 87, No. 3, May-June 1982**

**Contents**

	Page
The Density Determination of Small Solid Objects by a Simple Float Method—I. Randall M. Schoonover . . . . .	197
The Density Determination of Small Solid Objects by a Simple Float Method—II. R.S. Davis . . . . .	207
An Absorbed Dose Water Calorimeter: Theory, Design, and Performance. Steve R. Domen . . . . .	211
Torsional Splittings and Assignments of the Doppler-Limited Spectrum of Ethane in the C-H Stretching Region. A.S. Pine and W.J. Lafferty . . . . .	237
Mechanism of the Electrical Conductivity in Potassium Croconate Violet. Lawrence M. Doane and Alexander J. Fatiadi . . . . .	257
Publications of the National Bureau of Standards. . . . .	261

Library of Congress Catalog Card Number: 62-37059

---

For sale by the Superintendent of Documents, U.S. Government Printing Office.  
Washington, DC 20402.

Single copy price \$4.25 Domestic; \$5.35 Foreign.  
Subscription price: \$18.00 a year; \$22.50 for foreign mailing.

UNITED STATES GOVERNMENT PRINTING OFFICE, WASHINGTON: 1982

# The Density Determination of Small Solid Objects by a Simple Float Method—I

Randall M. Schoonover\*

National Bureau of Standards, Washington, DC 20234

January 20, 1982

The density determination of a small solid object with a mass of only a few hundred milligrams is always a difficult and often an elusive measurement. The advent of highly accurate hydrostatic weighing techniques and the density scale based on solid objects are utilized in a two liquid float method presented here that incorporates the advantages of this technology. The resulting measurement is an absolute determination of density with an uncertainty of 500 ppm and has a density range from 2.3 g/cm<sup>3</sup> (silicon) to 21.5 g/cm<sup>3</sup> (platinum). The instrument was used to measure the variation in the alloy density of nickel with respect to phosphorus content and to determine the density of optical fiber glass.

Key words: density measurement; float method; small solid objects; solid object density scale.

## 1. Introduction

The density determination of a small solid object with a mass of only a few hundred milligrams is always a difficult and often an elusive measurement. The advent of highly accurate hydrostatic weighing techniques [1,2]<sup>1</sup> and the density scale based on solid objects [3,4] are utilized in a two liquid float method presented here that incorporates the advantages of this technology. The resulting measurement is an absolute determination of density with an uncertainty of 500 ppm and has a density range from 2.3 g/cm<sup>3</sup> (silicon) to 21.5 g/cm<sup>3</sup> (platinum). The instrument was used to measure the variation in the density of nickel alloys with respect to phosphorus content [9] and to determine the density of "optical-fiber" glass.

### 1.1 Background

In 1923 Foulck [5] suggested that a float similar to an inverted hydrometer would be very sensitive to fluid density changes when the larger portion of the float was immersed in a fluid immiscible with and of different density from the fluid surrounding the stem. Foulck did not foresee the scientific usefulness for such a device and the idea was not applied until H. A. Bowman (formerly of NBS) suggested its use to Franklin and Spal [6] for measuring the density ratio of small samples. An obvious

and very useful application of Foulck's float is to the absolute determination of density for small solid objects as reported here.

## 2. The Method

When the float of figure 1 is immersed in two immiscible liquids of different density the tare weight can be adjusted so that the float is brought into equilibrium. If the solid object, of density  $\rho_{Ge}$ , is removed from the float and replaced by another sample, of density  $\rho_{Si}$ , and likewise a third object of  $\rho_{Ag}$ , and finally a fourth of sample,  $\rho_X$ , and all but the object of density  $\rho_{Si}$  have approximately equal mass, then new equilibrium positions in each case will be established if one of the two following conditions exist:

1. The density gradient in the fluid column is sufficiently large.
2. The geometry of the float possess sufficient compliance.

In practice these conditions can be varied to control the range and sensitivity of the float. The equilibrium equations given below correspond to four cathetometer observations,  $O_{Ge}$ ,  $O_{Si}$ ,  $O_{Ag}$ , and  $O_X$ , of the float's relative elevation, where  $O_{Ge} - O_{Si} = L_1 - L_3$  and  $O_{Ge} - O_{Ag} = L_1 - L_7$  etc.

$$g[\rho_{Ge} - \rho_L]V_{Ge} + F - \rho_L V_F + L_1 - \rho_L V_{L1} + L_2 - \rho_H V_{L2} = 0 \text{ corresponds to } O_{Ge} \quad (1)$$

\*Center for Absolute Physical Quantities, National Measurement Laboratory.

<sup>1</sup>Figures in brackets indicate literature references at the end of this paper.

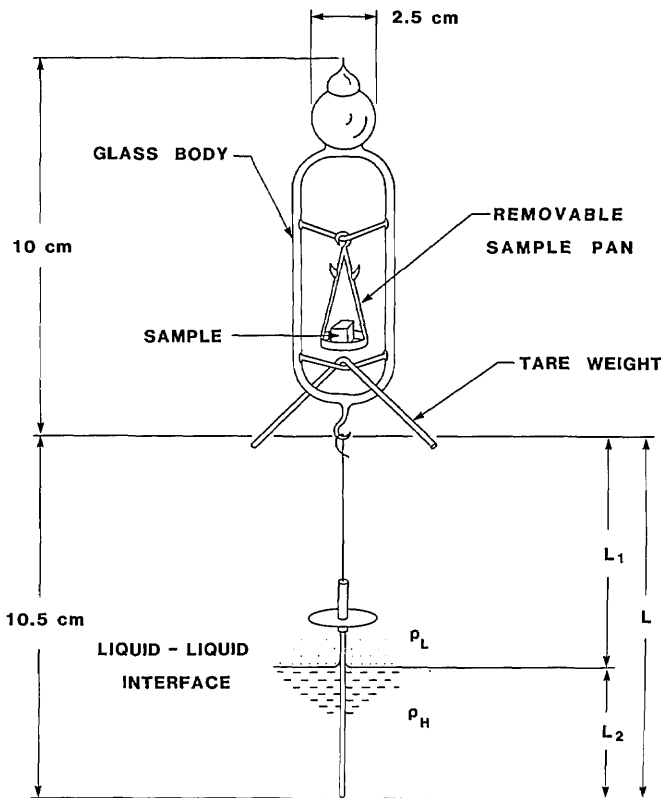


FIGURE 1: A sketch of the float assembly showing all of the components in the proper proportion.

$$g[Si - \rho_L V_{Si} + F - \rho_L V_F + L_3 - \rho_L V_{L3} + L_4 - \rho_H V_{L4}] = 0 \text{ corresponds to } O_{Si} \quad (2)$$

$$g[Ag - \rho_L V_{Ag} + F - \rho_L V_F + L_7 - \rho_L V_{L7} + L_8 - \rho_H V_{L8}] = 0 \text{ corresponds to } O_{Ag} \quad (3)$$

$$g[X - \rho_L V_X + F - \rho_L V_F + L_5 - \rho_L V_{L5} + L_6 - \rho_H V_{L6}] = 0 \text{ corresponds to } O_X \quad (4)$$

The terms Ge, Si, Ag and X are the sample masses corresponding to the volumes  $V_{Ge}$ ,  $V_{Si}$ ,  $V_{Ag}$ ,  $V_X$  with the subscripted L terms representing the mass of the float stem sections above and below the liquid-liquid interface. The less dense liquid has a density of  $\rho_L$ , and the more dense,  $\rho_H$ . Common to each equation are the forces acting on the float body,  $g(F - \rho_L V_F)$ , where F and  $V_F$  are the mass and volume of the float respectively. Equations (1), (3), and (4) are reduced for the unknown volume,  $V_X$  where:

$$V_X = \frac{\left(\frac{O_{Ge} - O_X}{O_{Ag} - O_{Ge}}\right) [Ag - Ge + \rho_L (V_{Ge} - V_{Ag})] + X - Ge}{\rho_L} + V_{Ge} \quad (5)$$

The term,  $\rho_L$ , appears twice in eq (5) and can be determined independently by solving eqs (1), (2), and (3) with the following result:

$$\rho_L = \frac{(Ge - Ag)(O_{Si} - O_{Ge}) + (O_{Ag} - O_{Ge})(Si - Ge)}{(O_{Si} - O_{Ge})(V_{Ge} - V_{Ag}) - (O_{Ag} - O_{Ge})(V_{Ge} - V_{Si})} \quad (6)$$

If the sample masses are sufficiently close then eq (5) reduces to a simpler form eliminating the need to know  $\rho_L$  as follows:

$$V_X = \left(\frac{O_{Ge} - O_X}{O_{Ag} - O_{Ge}}\right) (V_{Ge} - V_{Ag}) + V_{Ge} \quad (7)$$

For this work, the densities  $\rho_{Ge}$  and  $\rho_{Ag}$  are such that  $\rho_{Ge} < \rho_X < \rho_{Ag}$ , with the instrument range thus being established only in the region between  $\rho_{Ge}$  and  $\rho_{Ag}$ . In practice the range in density from 2.3 g/cm<sup>3</sup> for Si and 21.5 g/cm<sup>3</sup> for Pt should include fixed points at 5.3 g/cm<sup>3</sup> (Ge), 10.4 g/cm<sup>3</sup> (Ag), and 16.6 g/cm<sup>3</sup> (Ta), or other suitable materials of similar densities.

A contradictory requirement is placed on the density standards  $\rho_{Ge}$ ,  $\rho_{Si}$ , and  $\rho_{Ag}$  when used to determine,  $\rho_L$ . Since the largest possible buoyant force difference is desired, therefore the sample fabricated from the least dense material,  $\rho_{Si}$ , must have an increased mass that just permits an onscale equilibrium position. That is to say the objects, Ge, Ag, and X are approximately equal in mass, but the mass Si is significantly larger.

### 3. Apparatus

The success of the method described here requires that the apparatus be designed in such a manner as to make a difficult task manageable on a basis that routinely yields consistent and satisfactory results. It is the author's intent to give ample detail, at the expense of brevity, so the device can be duplicated successfully and without great pain by anyone desiring to do so.

#### 3.1 Choosing the Liquids

Fluorocarbon compounds have been used in density measurements for many years [4] because they are inert, their 1.8 g/cm<sup>3</sup> density increases the buoyant force compared to distilled water, they have a low surface tension, and they are not miscible with many common solvents. The requirements necessary for the two liquids used in this application are:

1. extremely low miscibility,
2. low interfacial surface tension and,
3. a large difference in their densities.

A liquid manufactured by the 3M company designated FC-43<sup>2</sup> was chosen as the denser liquid ( $\rho_H$ ). The other liquid selected, methanol, ( $\rho_L$ ) was chosen because it is reported to be immiscible with FC-43, meets the above requirements, and is not extremely hazardous. Early in the instrument development, the interfacial surface tension was measured between FC-75, a liquid with properties similar to FC-43 but not quite as desirable (for this application), and various solvents. Table 1 summarizes the results of that work. A few partially miscible liquids were measured to show that the interfacial surface tension decreases as the liquids partially mix. The interfacial surface tension data tend to verify the manufacturer's data regarding miscibility of various liquids with FC-75.

Although methanol was selected for use as the less dense liquid ( $\rho_L$ ) for the work described here, other liquids should work and would be required if a sample to be measured is soluble in methanol.

### 3.2 The Float

In essence the float is comprised of several components. They are:

1. the main borosilicate glass body
2. sample pan
3. removeable nichrome wire stem assembly
4. tare weight.

Figure 1 is a scale view of the float and figure 2 shows a cross-sectional view of the apparatus proportional to the float.

<sup>2</sup>The identification of trade names and company products in this paper is to adequately specify the experimental conditions. Such identification does not imply recommendation or endorsement by the National Bureau of Standards nor does it imply that these materials are necessarily the best available for the purpose.

The main borosilicate glass body is blown from thin wall borosilicate tubing. The overall mass and displacement volume are made small for improved dynamic response and to provide for a small overall liquid system. Likewise, the sample pan is fabricated from borosilicate glass. The pan has two barbs to accommodate samples of large thin sheets suspended from pan bails.

A stem assembly was devised to permit its easy removal while keeping the float immersed and allows for changing the stem diameter, and hence the instrument range. The disc is captured on the stem by two heat-shrinkable teflon bands as shown in figure 1. This feature prevents the float from rising to the surface during sample exchanges. A joint made of heat-shrinkable teflon permits coupling various diameters of treated nichrome wire [2] for making significant changes in sample mass or float sensitivity. The portion of wire above the joint either remains unchanged or is made nearly identical for each stem assembly.

### 3.3 Wire Treatment

Those experienced in hydrostatic weighing know the beneficial value of an oxide coating placed on the suspension wire that penetrates the air-water interface and connects the immersed load to the balance above. Early experimentation with float and wire stems of 0.008 and 0.012 in. diameter has indicated that coated stems significantly improved the precision as opposed to bare wire stems. Although the coating of nichrome wire is discussed by Bowman and Schoonover, [2], the float application has additional considerations to be concerned with.

In ordinary hydrostatic weighing the coated suspension wire is under enough tension to remove any curvature present, a wire 0.008 inch diameter will safely

TABLE 1. Interfacial surface tension between FC-75 and various liquids considered for the apparatus. The water FC-75 interfacial surface tension was very large and unmeasurable by the apparatus used.

Liquid	Specific Gravity	Surface Tension	Interfacial Tension
Methanol <sup>b</sup>	0.79	22.6 dynes/cm	11.0 dynes/cm
Isopropyl <sup>b</sup>	.68	21.7	6.5
Toluene	.87	28.4	8.0
Benzene	.87	28.9	9.0
Trichloroethylene	1.47		4.5
Acetone	0.79	23.7	7.5
Hexane <sup>a</sup>	.66	18.4	1.0
Heptane <sup>a</sup>	.68		2.2
Water <sup>b</sup>	1.0	72.0	Not Measured
FC-75	1.77	15.0	NA

<sup>a</sup>Partially miscible.

<sup>b</sup>According to the manufacturer not miscible with FC-43.

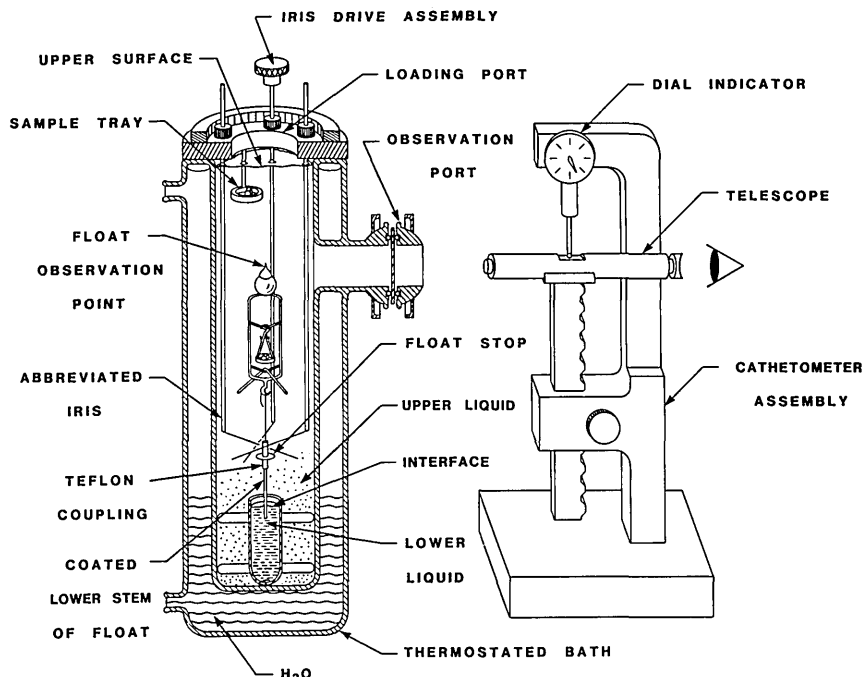


FIGURE 2: An overall schematic view of the density apparatus showing the float proportional to the surrounding chamber.

support a one kilogram mass, and therefore large diameters are not required. The float application here requires the wire to be inherently straight and as a practical matter a wire diameter of 0.062 inch may be desirable. The method of Bowman and Schoonover consists of heating the wire to 800°C in a vacuum (about 50 mTorr) by passing an electrical current through the wire. For the small-diameter wire (0.008-0.020 inch) it was necessary to construct a treatment chamber, as shown in figure 3, that keeps the wire in tension during the coating process, resulting in straight wire suitable for use as a float stem.

Larger diameter wires of 0.020 inch diameter and above required a different approach altogether. These large wires were straightened by stretching the wire beforehand. This was accomplished by reversing the action of a machine shop press. Coating then followed in a chamber designed to open at both ends and to have electrical connectors of higher current capacity. An autotransformer with a 20 A current rating is necessary for heating the larger wires. Near the completion of this work it was discovered the 0.062 inch wire could be coated successfully by merely heating the wire in air, periodically interrupting the process to view the coating density, and then terminating the heating when the coating appears correct (a very uniform pattern such as bark on a tree or a mountain range viewed from high altitudes). Future work may show that heating the wire in vacuum is only required for the smaller diameters.

The desired stem diameter, in centimeters, is calculated for a specified sample mass and density range as follows:

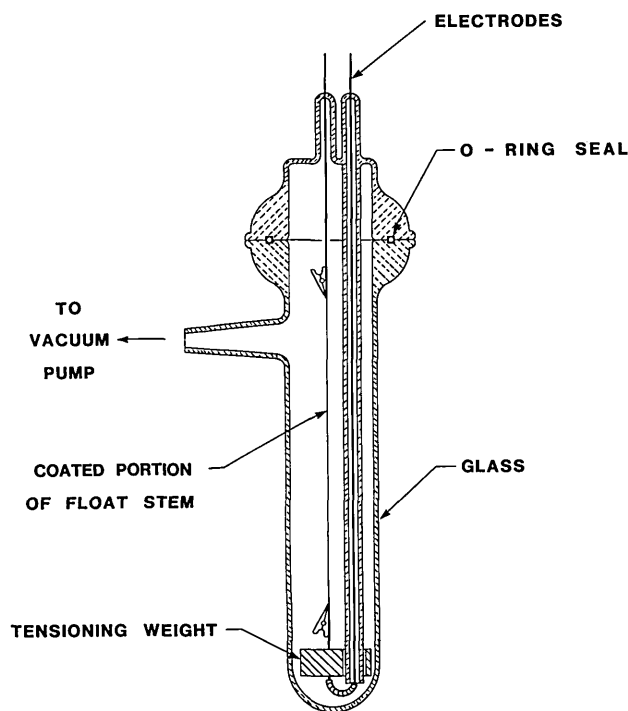


FIGURE 3: Float stem fabrication chamber.

### 3.5 The Iris Diaphragm

$$\text{Dia.} = 2 \left( \frac{\rho_L \Delta V}{2.54\pi(\rho_H - \rho_L)} \right)^{1/2} \quad (\text{cm}) \quad (8)$$

where  $\Delta V$  is the difference in volume between the least dense and most dense standard and, 2.54, is the cathetometer range in centimeters.

#### EXAMPLE 1:

For 0.3 g standards of  $\rho = 2.379 \text{ g/cm}^3$  and  $\rho = 5.327 \text{ g/cm}^3$  and liquid densities of  $\rho_L = 0.79 \text{ g/cm}^3$  and  $\rho_H = 1.88 \text{ g/cm}^3$  the difference in volume is

$$\Delta V = 0.3 \left( \frac{1}{2.329} - \frac{1}{5.327} \right) = .0725 \text{ cm}^3 \quad (9)$$

and the stem diameter is

$$\text{Dia.} = 2 \left( \frac{0.79 \times 0.0725}{2.54\pi \times 1.09} \right)^{1/2} = 0.162 \text{ cm (0.064 in)} \quad (10)$$

The precision in density measurements of a mass,  $X$ , which can reasonably be expected from such a wire can be estimated from the following formula:

$$\text{Precision} \approx \frac{\rho_x}{X} \frac{W(\rho_H - \rho_L)}{\rho_L} \times 3R \quad (11)$$

where  $W$  is the cross-sectional area of the chosen wire and  $R$  is the precision of the cathetometer reading.

#### EXAMPLE 2:

For a 0.2 g sample of unknown density ( $\rho_x \sim 2.3 \text{ g/cm}^3$ ), wire diameter 0.162 cm, and cathetometer precision  $5 \times 10^{-4} \text{ cm}$  the expected precision of a measurement of the unknown density is

$$\begin{aligned} \text{Precision} &\approx \frac{2.3}{0.2} \cdot 2.8 \times 10^{-2} \frac{(1.88 - 0.79)}{0.79} \times 3 \times 5 \times 10^{-4} \\ &\approx 7 \times 10^{-4} \text{ or } \pm 0.002 \text{ g/cm}^3. \end{aligned}$$

### 3.4 Tare Weights

Any major change in operating temperature, float sensitivity, or capacity requires a change in the tare weight, which is readily fabricated from nichrome wire. Each weight is adjusted so that when the float is loaded with the least dense and then the most dense standards, the float tip remains in view through the optical window.

A very important part of the apparatus is the abbreviated iris diaphragm formed by three equally spaced shafts. Each shaft is connected to a ring gear (with internal teeth) by a pinion gear. Thus, driving one shaft causes all three to rotate simultaneously and thereby open or close the wire fingers at the other end. One of these shafts is supported in an eccentric teflon journal bearing that can be rotated to reduce the backlash of all three pinion gears with the ring gear. The iris assembly is visible in figure 2.

Not only does the iris when closed prevent the float stem from leaving the lower liquid completely when the pan is removed from the float but it also serves to center the float after reloading. Details on its use are covered in a later section.

### 3.6 Liquid Cup

It is a very desirable feature of the apparatus to place the FC-43 liquid in a cup that is only a small portion of the surrounding bath volume. Earlier versions of the instrument required difficult and periodic cleaning of the liquid interface. This difficulty is avoided by use of a cup that was found to be self-cleaning if filled to the upper rim with FC-43. Therefore, a cup was designed that could be filled externally and lowered in place by a removeable wire bail. A stream of FC-43 is then released from a syringe from above and the droplets pass through the methanol completing the filling operation. The cup was made with a slight depression in the rim that allows foreign particles to be swept away by turbulence and immediately settle in the less dense methanol. FC-43 is very expensive and its recovery is economically desirable. The cup has the additional advantage of keeping the volume of FC-43 small and easily recoverable.

### 3.7 Temperature-Controlled Bath

Surrounding the float chamber is an outer container of borosilicate glass [4] that is fused at the top to the inner chamber. Figure 2 shows the cross-sectional view of the bath. An optical window with a 3 cm aperture for viewing the float tip was devised by fusing an "O"-ring connector at the proper location to the chamber and clamping a window between a teflon "O"-ring on the inside and an ordinary "O"-ring on the outside, as shown in Figure 2. This arrangement is readily disassembled for cleaning and the seal is virtually impervious to common solvents.

Two additional "O"-ring connections provide ports for circulating temperature controlled water capable of holding the bath temperature to  $\pm 0.003 \text{ }^\circ\text{C/hr}$ . When

the temperature controlled water is initially circulated an air pocket is trapped between the jacket wall at the very top and provides a damping effect on pump pulsation.

### 3.8 Cathetometer

A cathetometer was devised by mounting a dial indicator above a microscope mounted on a vertical guide. The device is shown schematically in figure 2. The microscope contains a "cross-hair" reticle for sighting on the float tip and has a magnification of 15 diameters. The system is back lighted with green light to improve the image.

The dial indicator has a range of 1 in (2.54 cm) and can resolve displacements of 0.0001 in with a nonlinearity less than 0.0001 and a precision of 0.0002 in. The dial indicator can be checked by inserting gauge blocks on the platen under the indicator stylus.

## 4. Sample Handling

To exchange samples carried on the float, the iris is first closed and the pan then removed with a long piece of stiff wire bent to form a V-shaped hook on the immersed end. Several such tools were fabricated from 0.032 inch stainless steel welding rods. The pan was placed on a loading platform (just under the methanol surface) and trapped in a recess such that the pan rim is flush with the sample storage surface. Then samples stored on the same support can be exchanged. This required that a forcep be designed (see fig. 4) for operation through a small aperture. The resulting tool can be opened by pushing the upper end down or closed by pushing the tubular body down. This forcep design has proved to be a great asset to the overall success of the measurement. Observe in figure 4, that the open end of the forceps allows for grasping most irregular shapes.

A storage rack of wire hooks on a cross-tree provides a means to store samples in the form of thin sheets by simply cutting a small hole in the sheet.

### 4.1 Sample Preparation

The standard objects of single crystal silicon, germanium, and silver were acid etched in the appropriate manner to remove work damage, thereby permitting both inspection for cracks that may result from the cutting process and adjustment of the mass. Glass and ceramic samples after cutting can be brought to the desired mass by various abrasion techniques. The extremely thin and brittle nickel-phosphorous alloys were cut from 0.003 in sheets by machining with a high velocity abrasive stream (sand blasting).

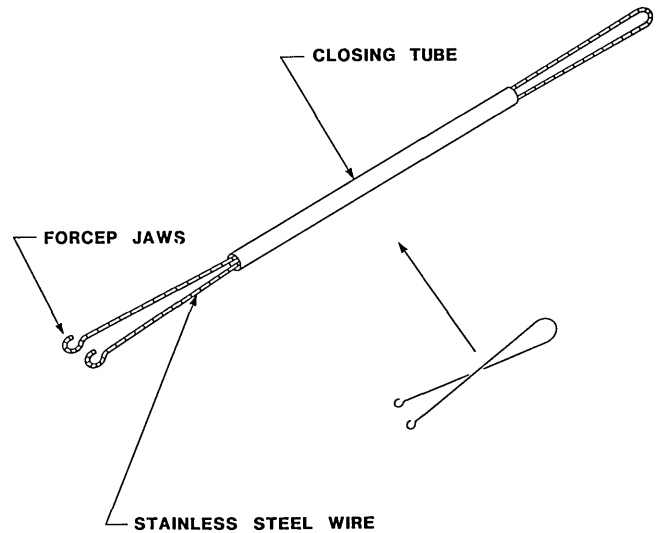


FIGURE 4: The single-handed, self-locking forcep designed for handling small solid samples.

When desired, the unknown sample mass can be adjusted to that of a density standard using a micro balance and the following equation that accounts for the buoyant force of air:

$$M_{Si} \left[ \left( 1 - \frac{\rho_a}{\rho_X} \right) - \left( 1 - \frac{\rho_a}{\rho_{Si}} \right) \right] = \Delta M. \quad (12)$$

Note: for  $\rho_X > \rho_{Si}$ ,  $\Delta M > 0$

where  $M_{Si}$  is the mass of the density standard,  $\rho_{Si}$ ,  $\rho_X$  is the approximate density of the unknown object as determined from a mechanical measurement or a handbook.  $\Delta M$  is the difference that would be indicated on a balance in air between the standard and unknown if these masses are equal in vacuum.

For example, if a silicon density standard having a mass of 0.300000 g is on hand and a germanium standard is to be fabricated to also have a mass of 0.300000 g, then (as indicated by the balance in air) the germanium sample must be 87  $\mu\text{g}$  more than the silicon standard as calculated from the parameters given below:

$$M_{Si} = \text{silicon mass of density, } \rho_{Si} \text{ (2.329 g/cm}^3\text{).}$$

$$\rho_a, \text{ the density of air, is assumed to be .00120 g/cm}^3\text{.}$$

$$\rho_X \text{ is the approximate density of germanium 5.3 g/cm}^3\text{.}$$

Sample masses can be adequately determined on appropriate analytical balances by the method given in [7]. This of course is necessary when one wishes to use the method of eq (5).

## 5. Test Method and Measurements

Initial investigation revealed two measurement requirements: a measurement sequence that eliminated drift and a waiting period of about 6 min before a stable float position is reached after a sample exchange and before the cathetometer observation is made. The waiting period begins when the port opening is closed immediately upon changing float loads. During this period the iris restricts the float position but does not impinge on its freedom to oscillate vertically. Just prior to reading the cathetometer the iris is opened to approximate an equilateral triangle with a base of 1 cm.

The weighing sequence used is illustrated as follows:

Object	Observation	
Germanium std.	$y_1$	
Silicon std.	$y_2$	$Ge = 1/2 (y_1 + y_5)$
Silver std.	$y_3$	$Si = 1/2 (y_2 + y_4)$
Silicon std.	$y_4$	$Ag = y_3$
Germanium std.	$y_5$	
$X_1$	$y_6$	
Silver std.	$y_7$	$Ge = 1/3 (y_5 + y_9 + y_{13})$
$X_2$	$y_8$	$Ag = 1/2 (y_7 + y_{11})$
Germanium std.	$y_9$	$X_1 = 1/2 (y_6 + y_{12})$
$X_2$	$y_{10}$	$X_2 = 1/2 (y_8 + y_{10})$
Silver std.	$y_{11}$	
$X_1$	$y_{12}$	
Germanium std.	$y_{13}$	

Observations  $y_1$  through  $y_5$  determine,  $\rho_L$ , and all but  $y_5$  are omitted if the masses of all objects are nearly identical or an assumed value for  $\rho_L$  is used or both. The equations to the right of the sequence average the cathetometer observations for each object in the sequence. The subscripted  $y$  terms, when averaged, correspond to the cathetometer observations in the equilibrium eqs (1), (2), (3), and (4).

### 5.1 Precision

For the initial precision test a stem diameter of 0.051 in wire was chosen to be used with 200 mg Si and Ge standards. The masses were adjusted close to each other, as were samples of uranium glass and lead glass. Three abbreviated measurement sequences were carried out using the method of eq (7). In the following results, the ranges were used to estimate the standard deviations,  $S$ .

	Test 1	Test 2	Test 3
Uranium			
Glass	2.2665g/cm <sup>3</sup>	2.6655g/cm <sup>3</sup>	2.2640 $S = 0.0015$ g/cm <sup>3</sup>
Lead			
Glass	4.4538	4.4540	4.4500 $S = 0.0024$ g/cm <sup>3</sup>

These data indicate the method has a precision of about 6 parts in 10,000. Note that the precision achieved for uranium glass agrees well with the predicted value (see EXAMPLE 2 above).

### 5.2 Linearity Test

Although the author has no reason to believe that die-drawn nichrome wire is not uniform in diameter to 1 part in 10,000 or better, a linearity test was devised to test the assumption.

Two additional float-equilibrium equations can be written as follows:

$$M_1 - \rho_L V_{M1} + F - \rho_L V_F + L_1 - \rho_L V_{L1} + L_2 - \rho_H V_{L2} = 0 \approx O_1$$

$$M_2 - \rho_L V_{M2} + F - \rho_L V_F + L_3 - \rho_L V_{L3} + L_4 - \rho_H V_{L4} = 0 \approx O_2$$

The above can be put in the form where  $M_1 - M_2 = \Delta M$  and

$$\frac{O_1 - O_2}{\Delta M} = -K \left[ \frac{1 + \frac{\rho_L}{\rho_M}}{\rho_L - \rho_H} \right] = \text{constant}$$

The above is true if the density,  $\rho_M$ , of both mass  $M_1$  and  $M_2$  is the same.

For the linearity test three silicon silicon crystal masses were fabricated and placed sequentially and in combination on the float pan as shown below. The float stem diameter was 0.062 in.

LINEARITY TEST				
Sequence	Cathetometer Reading	$\Delta M$	Calculated Constant	Residuals
Zero	0.9898			
$\Delta M_1$	0.7342	0.022954g	11.144	-0.009
Zero	0.9903			
$\Delta M_2$	0.5810	0.036692	11.174	0.021
Zero	0.9917			
$\Delta M_3$	0.4078	0.052390	11.141	-0.012
Zero	0.9913			
$\Delta M_4$	0.1515	0.075344	11.152	-0.001
Zero	0.9921		$\bar{X}$ 11.1528	

Examination of the above residuals does not show a correlation between  $\Delta M$  and float position and that therefore the diameter of the wire is acceptably constant at the present level of precision.

### 5.3 The measurement of "optical-fiber" glass

The density of samples of "optical-fiber" glass were measured and the data are used to demonstrate the

method where all masses are nearly equal (knowledge of  $\rho_L$  is not required). The density is then recalculated using the measured mass and an assigned value for  $\rho_L$  based on the bath temperature[8].

The results given below are based on two independent measurement sequences for each sample where a single crystal silicon and germanium are the standards. The sample masses were about 0.3g and the stem diameter was 0.062 inch

Method #1 (assuming equal masses (0.299000 g) - eq (7))				
Sample	D14	B14(1132)	B15(1072)	B15(1076)
Density	4.5464g/cm <sup>3</sup>	2.4908	2.4125	2.4091

Method #2 (measured mass and assigned $\rho_L$ ) - eq (5)				
Sample	D14	B14(1132)	B15(1072)	B15(1076)
Density	4.5458	2.4915	2.4098	2.4108
Temperature, 21.5 °C				
Assigned $\rho_L = 0.78991 \text{ g/cm}^3$				

Method #1 - Method #2			
	D14	B14(1132)	B15(1072)
Density	-0.0006g/cm <sup>3</sup>	-0.0007	+0.0027
			-0.0017

Sample Masses	Differences in Mass
Si 0.299900 g	Si - Ge = + 15 $\mu\text{g}$
Ge 0.299885	Si - D14 = + 34 $\mu\text{g}$
D14 0.299866	Si - B14(1132) = + 41 $\mu\text{g}$
B14(1132) 0.299859	Si - B15(1072) = - 6 $\mu\text{g}$
B15(1072) 0.299906	Si - B15(1076) = + 58 $\mu\text{g}$
B15(1076) 0.299842	

Differences as large as 1 part in 1000 in density do occur between the two methods, however the actual mass determination is avoided for all objects except the silicon standard in method #1 and likewise the measurement of  $\rho_L$  is avoided. It will be shown later that handbook values for  $\rho_L$  agree well with the measured values and  $\rho_L$  could have been measured here merely as a check standard.

#### 5.4 Nickel Phosphorous Alloy Determination

The Corrosion and Electrodeposition Group of the NBS submitted very small samples of nickel phosphorus alloy for which the density determination was very difficult. The success of these measurements thoroughly demonstrates the usefulness for scientific purposes of the method presented here.

The samples were fabricated by chemical deposition of nickel phosphorous alloy on a copper substrate. The substrate is then etched away leaving a very thin (0.003 in) plate that is extremely brittle and fragile. One aspect of the study was to correlate the alloy density with phosphorous content. The metallurgical significance of this work is reported by Ogburn et al. [9].

Sample preparation required the use of an abrasive machining process (sand blasting), to obtain samples in the approximate shape of a disc and a mass 0.2 g. To facilitate their manipulation in the float chamber a 3 mm hole was machined in each disc. The mass of each sample was then adjusted to the sample of least mass by additional machining. The mass adjustment process was not easily controllable and wide variations were present in the final values.

It was necessary to use the more protracted measurement scheme; i.e. determine all of the masses and measure  $\rho_L$ .<sup>3</sup> A 0.042 in dia. wire was selected for the float stem to increase the measurement sensitivity. Because the nickel phosphorous alloy has a density of  $\approx 8.0 \text{ g/cm}^3$  it was necessary to determine the density of a boule of single crystal silver by hydrostatic weighing [2], thus providing a density standard of 10.492 g/cm<sup>3</sup>. Single crystal germanium (5.327g/cm<sup>3</sup>) was the other standard used. A silicon crystal of 0.268 g provided the large buoyant force required to determine  $\rho_L$ .

The full measuring sequence given previously was then used to assign values to the nickel alloys, no parameters being assumed. The data presented below are three independent determinations but do not include all of the results reported in [9]. The reader may recall there are two values for each unknown determined in the sequence, the mean value is reported here for each measurement.

SAMPLE IDENTIFICATION				
	NI42-7% PH	NI24-9% PH	NI50-10% PH	NI56-10% PH
Meas. 1	8.201 g/cm <sup>3</sup>	8.091g/cm <sup>3</sup>	8.044 g/cm <sup>3</sup>	8.049 g/cm <sup>3</sup>
Meas. 2	Outlyer	8.088	8.052	8.059
Meas. 3	8.207	8.083	8.047	8.061
$\bar{X}$	8.204	8.087	8.048	8.056
Std. Dev.	0.0053	0.0047	0.0047	0.0071

NOTE: Std. Dev. was determined by the range method [10].

The sample masses were:

Si	0.268376 g
Ge	0.199798
Ag	0.197764
NI24	0.200167
NI42	0.199496
NI50	0.196077
NI56	0.200613

The methanol densities, as determined from the above measurements, are as follows:

<sup>3</sup>Suggested by R. S. Davis.

0.7897 g/cm<sup>3</sup> at 22.2°C  
0.7902  
0.7901  
0.7903  
0.7899  
0.7899

$\bar{X} = .7900$  (handbook value 0.7896 g/cm<sup>3</sup>)  
Std. Dev. = 0.0002

One would expect a higher measured value than that given by the table due to absorbed water in the methanol (the table value is for pure methanol). An effort will be made in any future work to perform a Karl Fischer titration for an estimate of the absorbed water.

## 6. Uncertainty of the method

In considering the sources and effects of errors, the discussion will be limited to the method that includes the determination of  $\rho_L$  as well as the unknown sample masses. It is well documented by hydrostatic weighing [1,2,4] and other float techniques [11] that the density of single crystal materials can be determined to better than 10 ppm and the material is homogeneous to that level or better. This means errors in the volumes of the standards used here are almost entirely due to the mass determinations. If the material mass is greater than 100 mg, ordinary mass measurement methods [7] will not cause errors that exceed 10  $\mu$ g (100 ppm), which is well below the precision attained by the float method at this time. As the sample mass decreases the mass determination would have to be improved.

From an analysis one can conclude that the cathetometer-float system may have a basic limitation in the float hydrodynamics. However, a slight improvement may be gained with a more precise cathetometer. Since the uncertainty is due to both imprecision and insignificant systematic error, the uncertainty assigned to the nickel-phosphorous samples is taken to be 1 standard deviation.

## 7. Conclusion

The utilization of the solid object density scale, the ease and reliability of the technique make this method of measuring small sample densities attractive for general laboratory use.

Early in the development of this instrument the float was assembled with a 0.010 in diameter wire and the results indicated the sample size can be decreased to 10 mg and still use the method reported here. However, a greater effort would be required in the mass determinations. Such small diameter stems would be quite useful if

one were only interested in density ratios [12], a technique not investigated here.

Given the clear advantage of hindsight it seems unfortunate that isopropyl alcohol was not tested for use as the less dense liquid. The resulting lower interfacial surface tension may enhance the overall float performance.

Perhaps the overall performance could be improved with the proper choice of an additive to decrease the interfacial surface tension. Personal communication with M. R. Moldover suggest this may be contradictory if the fluids are to remain immiscible [13]. This area certainly requires some attention if the instrument performance is to be improved.

Many years ago Bowman and Schoonover [11] attached a magnet to their cartesian diver and seved it to a null position. Although the effort was successful for density ratios, it did not work to the desired 0.1 ppm. Perhaps using a magnet on the float here would eliminate the lower liquid and yield a precision 1 or 2 orders of magnitude improvement.

---

The author expresses gratitude to F. E. Jones for his assistance in checking the algebra and for the statistical analysis he provided. Thanks to R. S. Davis for checking algebra and for suggesting the methanol density determination; to Charles Reeve for the measurement sequence; and to James Taylor for the preparation of the artwork.

## 8. References

- [1] Henins, I. J. Res. Nat. Bur. Stand. (U.S.). 68A(5): 529-533; 1964 September-October.
- [2] Bowman, H.A.; Schoonover, R.M. Procedure for high precision density determinations by hydrostatic weighing. J. Res. Nat. Bur. Stand. (U.S.). 71C(3): 179-198; 1967 July-August.
- [3] Bowman, H.A.; Gallagher, W., Schoonover, R. The development of a working density standard. Inst. Soc. of Amer., 20th Annual ISA Conference and Exhibit, October 4-7, 1965 Los Angeles, Preprint No. 14.8-4-65.
- [4] Bowman, H.A., Schoonover, R.M., Carroll, L.C. A density scale based on solid objects. J. Res. Nat. Bur. Stand. (U.S.). 78A(1): 13-40; 1974 January-February.
- [5] Foulck, C.W. A new form of precision hydrometer. J. Opt. Soc. of Amer. and Rev. Sci. Instrum. 7(3): 327-334; 1923.
- [6] Franklin, A.D.; Spal, R. A method for the precision comparison of the densities of small specimens. Rev. Sci. Instrum. 42(12): 1827-1833; 1971.
- [7] Schoonover, R.M.; Jones, F.E. Air buoyancy correction in high accuracy weighing on analytical balances. Anal. Chem. June 81.
- [8] International critical table of numerical data, *Physics, Chemistry and Technology*. Volume III, 1928, page 27.
- [9] Ogburn, F.E.; Schoonover, R.M.; Johnson, C.E. Plating and Surface Finishing, 68(42), March 1981.
- [10] Biometrika Tables for Statisticians, Vol. I, edited by E.S. Pearson and O.H. Hartley, The University Press, Cambridge, 1958.

- [11] Bowman, H.A., Schoonover, R.M. Cartesian diver as a density comparator. *J. Res. Nat. Bur. Stand. (U.S.)*. **69C(3)**: 217-223; 1965 July-September.
- [12] Davis, R.S. *J. Res. Nat. Bur. Stand. (U.S.)*. **87(3)**; ; 1982 May-June.
- [13] Moldover, M.R.; Cohn, F. An interface phase transition: Complete to partial weighing, *Science* **V-1 207**: 1073-1075; 1980.

# The Density Determination of Small Solid Objects by a Simple Float Method-II

R. S. Davis\*

National Bureau of Standards, Washington, DC 20234

January 18, 1982

The measurement of density changes in solid samples of less than one gram is often of practical interest. We describe here such relative measurements having a precision of a few parts in  $10^4$  using a newly reported apparatus. Comparisons of results with theory are presented.

Key words: density; density changes; density of solids; small samples.

## 1. Introduction

The preceding paper [1]<sup>1</sup> describes the construction and use of apparatus for determining the absolute density of small solid objects. It is often, however, of interest to find small differences in the relative densities among a set of samples. It is generally true that the density ratios of nearly equal samples can be found with higher accuracy than the density of any one sample can be measured absolutely. An example of the application of the apparatus of Schoonover [1] to this important class of measurement follows. The results make possible a qualitative comparison of the performance of this apparatus with a similar one developed by Franklin and Spal [2].

## 2. The problem

Four samples, A, B, C, and D, of crystalline  $\text{Al}_2\text{O}_3$  (sapphire) were made available to us for evaluation.<sup>2</sup> Sample A was untreated and had a density of  $3.986 \text{ g}\cdot\text{cm}^{-3}$  based on x-ray measurements. Sample B, which was slightly pink in color, had  $\text{Ti}^{+3}$  substituted for  $\text{Al}^{+3}$  in about 0.1% of the aluminum sites of the pure material. To produce sample C, a specimen similar to B had been heated at  $1600 \text{ }^\circ\text{C}$  for 1 day, which oxidized the dopant to the  $\text{Ti}^{+4}$  state causing the color to disappear. Finally, sample D was identical to C except that it was annealed in air for 190 hours at  $1400 \text{ }^\circ\text{C}$ .

This last sample is white, indicating the presence of  $\text{TiO}_2$  (rutile) precipitate.

Of particular interest was the density of sample C because this value was thought at the time of these measurements to depend strongly on the role of the charge concentration defects; i.e. whether aluminum vacancies are present (leading to a calculated density of  $3.987 \text{ g}\cdot\text{cm}^{-3}$ , based on the same lattice parameters as pure  $\text{Al}_2\text{O}_3$ ) or whether interstitial oxygen is formed (raising the calculated density to  $3.998 \text{ g}\cdot\text{cm}^{-3}$ ). Other types of measurements by the group at Case Western Reserve strongly support the interstitial oxygen hypothesis [3].<sup>3</sup>

## 3. Experimental

### 3.1 Choice of Stem Diameter

Since the expected change in the density of sample C relative to A was thought to be  $+30 \times 10^{-4}$ , the experiment was designed to have a relative precision of at least  $3 \times 10^{-4}$  in determining densities. The samples were adjusted by abrasion to have a nominal mass of 250 mg and to be within  $50 \mu\text{g}$  of equality, after which they were weighed to determine their masses exact to  $5 \mu$ .

According to eq (8) of Ref. [1], the coated wire need only be  $8.3 \times 10^{-3} \text{ cm}$  in diameter (0.003 inch) which would give a theoretical precision of relative density of about  $4 \times 10^{-6}$  but would certainly produce an enormous drift rate in the equilibrium position of the float due to temperature changes in the upper liquid. A wire of 0.51 mm diameter (0.020 inch) was therefore chosen as being

\*Center for Absolute Physical Quantities, National Measurement Laboratory

<sup>1</sup>Figures in brackets indicate literature references at the end of this paper.

<sup>2</sup>The author is indebted to Dr. Arthur Heuer of Case Western Reserve University for these samples, which were remnants of research carried out in his department.

<sup>3</sup>This work was published subsequent to the measurements described here.

the largest which would serve the experimental requirements.

### 3.2 Measurements

From equilibrium equations similar to (1) and (2) of Ref. [1], it is easy to show that the volume difference between two samples, e.g. A and B, influences the equilibrium position of the float through the following relation:

$$\Delta V \equiv V_B - V_A = \frac{W(\rho_H - \rho_L)}{\rho_L} (O_B - O_A) + \frac{B - A}{\rho_L} \quad (1)$$

where  $W$  is the cross-sectional area of the coated wire and the other terms have the same sense as in [1].

The ratio of densities is then given by

$$\frac{\rho_B}{\rho_A} = \frac{B}{A(1 + \Delta V \frac{\rho_A}{A})} \quad (2)$$

Our hope was to determine  $\Delta V$  through the relationships in eq (1) by using handbook values for  $\rho_L$  and  $\rho_H$ , and micrometer measurements to determine  $W$ . The experience reported by Franklin and Spal was somewhat discouraging, however. The latter paper describes huge daily variations in the value of  $W(\rho_H - \rho_L)$  inferred from float measurements; i.e., with a measured precision of  $2 \times 10^{-4} \text{ g}\cdot\text{cm}^{-1}$  for a given run, values as large as 2.6 times and as small as 1.3 times greater than the theoretical value of  $6.6 \times 10^{-4} \text{ g}\cdot\text{cm}^{-1}$  were found from experiment to experiment. [To circumvent this difficulty, they used a clever scheme involving the measurement of each unknown sample against six standards of equal density (near that of the unknown) and masses nominally equal but varying over a span of about 1.3 percent.]

In the work reported here samples A, B, C and D were placed on the float at regular intervals in a symmetric series and the equilibrium positions noted by viewing with a cathetometer as described in [1]. During the measurements, the equilibrium position of the float drifted upwards with time.

At the conclusion of the measurements, the equilibrium positions of each sample were plotted against time and the points fit with the least squares line. All four such lines had identical slopes within experimental uncertainty. At the same arbitrary instant near the midpoint of the measurements, the value of the equilibrium position was predicted from the four curves. It is worthwhile noting that the standard deviations of the predicted points were between  $1.8 \times 10^{-3} \text{ cm}$  and  $3.0 \times 10^{-3} \text{ cm}$  whereas the cathetometer itself had a

repeatability of  $0.5 \times 10^{-3} \text{ cm}$ . Thus for these measurements, the cathetometer does not limit the precision.

The pertinent data and results are shown in Table 1. The error bars represent a single standard deviation with no contribution being added for deviations of the buoyant forces from naive theoretical values.

The unexpected result for  $\rho_C/\rho_A$  prompted a check of the simple assumptions. To this end, three additional standards were fabricated—two of germanium and one of silicon. With the same stem described above but now using the three new standards to achieve an absolute determination of density as outlined in [1], the results shown in Table 2 were obtained.

### 4. Discussion

Subsequent to these measurements, data became available which led to an explanation of the unexpected results: The predictions of density for sample C had assumed the lattice parameters of that crystal were the same as those of pure  $\text{Al}_2\text{O}_3$ . An actual measurement, however, revealed a significant lattice relaxation which, it is now believed, obscures the change in density to the extent that the revised predictions are presently within the precision of our measurements [3].

The close agreement between experimental and theoretical values for  $\rho_L$  and  $W(\rho_H - \rho_L)/\rho_L$  shown in table 2 is remarkable. The slight discrepancy in  $\rho_L$  values may reflect contamination of the upper liquid (methanol) with water, although this possibility was not followed up. The value obtained for  $\rho_B/\rho_A$  is consistent in both sets of measurements justifying the simplifying assumptions made in obtaining results from the former set.

In short, none of the behavior which lead Franklin and Spal to suspect a density gradient in the upper liquid of their apparatus is apparent in the device used here. This result may reflect nothing more than a different choice of liquids but it is nevertheless worth noting. Beyond this, it is difficult to compare the performance of the apparatus used here with that reported in [2]. The latter is noteworthy for reporting a precision in ratio measurements equal to our own but on samples having one fifth the volume. It is not yet known whether the apparatus of Ref. [1] could do as well with smaller samples assuming the float volume and wire diameter were scaled down accordingly.

---

It is a pleasure to acknowledge the help, already alluded to, of Dr. Arthur Heuer of Case Western Reserve University in providing the samples used for this work,

TABLE 1. Relative density measurements of Samples A, B, C, and D

	$\rho_L$	=	0.790 g·cm <sup>-3</sup>		
	$\rho_H$	=	1.88 g·cm <sup>-3</sup>		Assumed Values
	$W$	=	2.03 x 10 <sup>-3</sup> cm <sup>2</sup>		

Sample	Mass	Approximate Density	Equilibrium Position
A	0.253715 g	3.986 g·cm <sup>-3</sup>	0.9873 cm
B	0.253665		1.0091
C	0.253690		1.0074
D	0.253669		1.0122

From eq 2

$$\left. \begin{aligned} \frac{\rho_B}{\rho_A} &= 1 - 1.7 \times 10^{-4} \\ \frac{\rho_C}{\rho_A} &= 1 - 4.8 \times 10^{-4} \\ \frac{\rho_D}{\rho_A} &= 1 - 3.7 \times 10^{-4} \end{aligned} \right\} \begin{aligned} &\pm 1.8 \times 10^{-4} \text{ * random error (from } \theta_B, \theta_C, \theta_D) \\ &\pm 1.8 \times 10^{-4} \text{ systematic error (from } \theta_A) \end{aligned}$$

\*errors are estimated at a level of one standard deviation.

in describing their history, and in patiently explaining the theoretical calculations of their density. I also wish to thank Randall Schoonover for advice in using the apparatus which he has developed.

### 5. References

- [1] Schoonover, R.M. The density determination of small solid objects by a simple float method-I, J. Res. Nat. Bur. Stand. (U.S.) 87(3); 1982 May-June.
- [2] Franklin, A. D.; Spal, R. A method for the precision comparison of the densities of small specimens. Rev. Sci. Instrum. 42 (12): 1827-1833; 1971 December.
- [3] Phillips, D.S.; Mitchell, T. E.; Heuer, A. H. Precipitation in star sapphire III Chemical effects accompanying precipitation. Phil. Mag. A 42 (3): 417-432; 1980.

TABLE 2. Absolute density measurements of samples A and C.

Standard	Mass	Density
Ge 1	0.238260 g	5.3270 g·cm <sup>-3</sup>
Ge 2	0.234903	5.3270
Si	0.309219	2.3291
Temp = 22.20 °C		

Results:

	Experimental	Assumed
$\rho_A$	$3.9847 \pm 0.001 \text{ g·cm}^{-3a}$	$3.986 \text{ g·cm}^{-3}$
$\rho_C$	$3.9838 \pm 0.001 \text{ g·cm}^{-3}$	—
$\rho_L$	$0.7897 \pm 0.0001 \text{ g·cm}^{-3}$	$0.7892 \text{ g·cm}^{-3}$
$\frac{W(\rho_H - \rho_L)}{\rho_L}$	$(2.83 \pm 0.02) \times 10^{-3} \text{ cm}^2$	$(2.80 \pm 0.005) \times 10^{-3} \text{ cm}^2$
$\frac{\rho_C}{\rho_A}$	$1 - 2.3 \times 10^{-4} \pm 3.5 \times 10^{-4}$	—

\*errors are estimated at a level of one standard deviation.

# An Absorbed Dose Water Calorimeter: Theory, Design, and Performance\*

Steve R. Domen\*\*

National Bureau of Standards, Washington, D.C. 20234

January 13, 1982

Two calibrated thermistors sandwiched between two insulative polyethylene films were immersed in a 30 cm cube of water having a low thermal diffusivity. The product of the specific heat of water and temperature rise gave the combined effect of the local absorbed dose and any heat defect at a position along a temperature profile produced by cobalt-60 irradiation. The dose rate was near 18 mGy/s and exposure times were 3 min. The standard deviation for a daily set of measurements was about 0.6 percent. Calculations showed that conductive heat transfer produced a negligible effect at the position of measurement along the beam axis. Tests showed the absence of convection.

Temperature drifts before irradiation were quickly controlled by changing the power dissipated in the water between two immersed electrodes. Reproducible measurements were obtained in distilled water supplies that had a wide range of impurities. Measurements, after saturating the water with nitrogen or oxygen, showed no difference. A difference of 0.6 percent would have been easily detectable. Tests with several chemicals added to water showed some unexpected results and changes in the measured absorbed dose rate versus accumulated dose. The measured absorbed dose rate in distilled water under the conditions described was 3.5 percent higher than that determined from measurements with a graphite calorimeter.

Key words: absorbed dose; calorimeter; convection; heat defect; radiation chemistry; thermistor; water.

## Contents

1. Introduction . . . . .	211	9. Calorimeter Performance . . . . .	222
2. Measurement Theory . . . . .	212	10. Thermistor Power Levels . . . . .	224
2.1 Measurement . . . . .	212	11. Tests in the C, J, and C + J Modes . . . . .	226
2.2 Conduction . . . . .	212	12. Tests for Water Convection . . . . .	226
2.3 Convection . . . . .	214	13. Effects of N <sub>2</sub> and O <sub>2</sub> Saturated Water . . . . .	229
3. The Calorimeter . . . . .	215	14. Effects of Water Impurities . . . . .	229
4. The Detector . . . . .	216	15. Results of Collimated Beam . . . . .	232
5. The Wheatstone Bridge . . . . .	218	16. Corrections and Uncertainties . . . . .	233
6. Thermistor Sensitivity Measurements . . . . .	219	17. Discussion . . . . .	233
7. Calorimeter Setup . . . . .	221	18. Recommendations . . . . .	234
8. Temperature Drift Control . . . . .	221	19. Summary . . . . .	234

## 1. Introduction

The purpose of this paper is to describe an improved model of an absorbed dose<sup>1</sup> water calorimeter previously reported [1].<sup>2</sup> Many features of the present improved

\*Some initial work was supported in part by the National Cancer Institute, National Institute of Health, Bethesda, Md.

\*\*Center for Radiation Research, National Measurement Laboratory.

<sup>1</sup>Absorbed dose is the mean energy per unit mass imparted to matter by ionizing radiation. The SI unit of absorbed dose is the gray (symbol Gy). 1 Gy = 1 J/kg.

<sup>2</sup>Figures in brackets indicate literature references at the end of this paper.

model that includes a unique and simple method for quickly bringing temperature drifts under control are described in a U.S. patent [2]. Those features will be described here in further detail along with results of investigations, tests, and experimental measurements. This work was described briefly [3] and in its entirety [4].

The calorimeter is unique in several respects, one being that for the first time measurements of an absorbed dose profile can be derived from measurements of temperature rises at points along a temperature profile in a large continuous water medium. The intention of this

simple method is to circumvent indirect measurements in other materials (with spectral-sensitive detectors such as ionization chambers) and numerous correction factors to convert those measurements to water which is the standard reference material [5]. A direct measurement in water would then also circumvent any required knowledge of the incident spectrum which is too often not well-known but must be estimated and used in time-consuming calculations when indirect measurements are made. The calorimeter also circumvents another problem that appears too complicated to resolve: the effect of vacuum gaps around calorimetric bodies made of solid material. That effect would be extremely difficult to evaluate experimentally or theoretically for the numerous incident radiation and scattering patterns throughout the medium [1,6]. The problem is further complicated because gaps of varying sizes are made by different experimenters. This paper describes an absorbed dose calorimeter that has no gaps.

A workable absorbed dose water calorimeter would be a valuable tool in the medical and radiation chemistry fields, but there appears to have been no investigation, report, attempt, or even serious discussions of the problems of such a calorimeter.

The development of this calorimeter should be viewed as involving two major efforts. The necessary first effort was to overcome the physical problems in making the calorimeter an effective and accurate instrument for measuring a temperature rise at a point in water. In this respect, investigations and experience have shown that there are really no major problems with the calorimeter. It is an efficient instrument. It is relatively easy to construct, can be put into operation quickly, and is much easier to control and to operate than solid-bodied absorbed dose calorimeters requiring vacuum systems. The ease of control was made possible because advantage was taken of the mobility of water to quickly bring the calorimeter to a uniform operating temperature, but more important is that use is made of a unique and simple method that essentially instantly eliminates relatively large temperature drifts by merely changing a potential across immersed electrodes [2]. The second major effort is to determine the existence of and corrections for heat defects (negative and positive) in distilled water. This will be a relatively long investigation, both experimentally and theoretically, using different irradiation beams and dose rates. The present paper describes measurements only for cobalt-60 irradiation.

## 2. Measurement Theory

The measurement theory for the determination of absorbed dose in water is described in this section. Effects of conductive temperature changes at the position of

measurement were determined by application of a simple and well-known graphical method of calculating changes in a temperature profile. The temperature profile will be undisturbed by buoyant forces if they are not sufficiently large to set convection in motion.

### 2.1 Measurement

Advantage was taken of the low thermal diffusivity of water (that retards a temperature change at a point of measurement) and of the imperviousness of polyethylene film (that electrically insulates the sensors and their leads). Two bead thermistors placed close together were sandwiched between polyethylene films and immersed in distilled water. The thermistors formed opposite arms of a Wheatstone bridge circuit to double the sensitivity compared to a one-thermistor bridge.

It can be shown that (for small temperature changes and for negligible heat defects, lead resistances, and negligible electrical power changes in the thermistors) the absorbed dose determined with the two-thermistor bridge is:

$$D = (1/2)(\Delta R/R)(\bar{S}^{-1})(c), \quad (1)$$

where  $D$  is the absorbed dose,  
 $(1/2)$  is the result of using two thermistors to measure a temperature,  
 $\Delta R/R$  is the fractional change in the Wheatstone bridge balancing resistor,  
 $\bar{S}$  is the mean fractional change in resistance of the thermistors per unit temperature rise, and  
 $c$  is the specific heat capacity of water.

If  $c$  is in  $J/(g \cdot K)$ ,  $D$  is in  $kGy$ . The product  $(1/2)(\Delta R/R)(\bar{S}^{-1})$  is the temperature rise. The sensitivity,  $\bar{S}$ , was determined to an accuracy of about 0.1 percent and was stable over long periods of time. A table of accurate values of  $c$  versus temperature is given in Ref. [7]. The values are listed to five figures and vary by only one part in 10,000 per degree Kelvin.

### 2.2 Conduction

Exact theoretical calculations of three dimensional heat flow present a time-consuming and formidable challenge, which may even then be of little or no value in applying calculated temperature corrections to measurements. A theory would be based on an assumption of detailed knowledge of the absorbed dose distribution and that the background drift rates remain zero, are constant, or follow an assumed behavior when in practice they are always subject to unpredictable or difficult-to-

predict changes. These drifts could be caused by external or internal sources, such as the rapidly changing temperature distributions caused by successive runs with collimated beams of low energy electrons. These changes affect the observed temperature rise and the curvatures of the initial and final drifts. However, calculations have value when they indicate the magnitude of a correction, which is useful for the experimenter to determine the approaching limit of accuracy of measurements. For example, theoretical calculations are of value when they indicate an approximate upper bound to the duration of an irradiation run in which the heat conduction corrections can still be considered small or negligible compared to the overall uncertainty of an experiment. As the background instabilities become a significant fraction of the calculated corrections, the corrections would be applied with increasing uncertainty and eventually would become meaningless. It is the drift rates and instabilities that must be kept small and under control in order to extend the same quality of measurements to lower dose rates and longer irradiation times.

Absorbed dose measurements in water were made with cobalt-60 beams shaped with square collimators to produce: (1) a broad beam that irradiated the entire calorimeter; and (2) a smaller beam, that had also been used previously to irradiate an absorbed dose graphite calorimeter [8], the measurements being converted to absorbed dose in water [9]. In the former, heat flow was essentially along the beam axis, whereas in the latter heat flow was predominately radial.

Simple calculations of linear heat flow that produces temperature changes at a point of measurement were made by use of an elegant and well-known graphical method<sup>3</sup> (illustrated below) that can be made to converge to a theoretical solution. The calculations showed that for an instantaneous pulse of a broad and parallel beam of cobalt-60 gamma radiation, the temperature rise at a 5-cm depth in water would decrease by only 0.02 percent of the initial rise in 4 min. This small temperature change results from a slowly changing axial temperature profile that causes essentially the same amount of heat to enter as to leave the point of measurement. Although the collimated beam caused much larger temperature changes as a result of radial heat flow, the calculated changes (assuming zero background drift) were also negligible for irradiations lasting several minutes.

Figure 1 illustrates the numerical method applied to radial heat flow along lines through the beam axis and

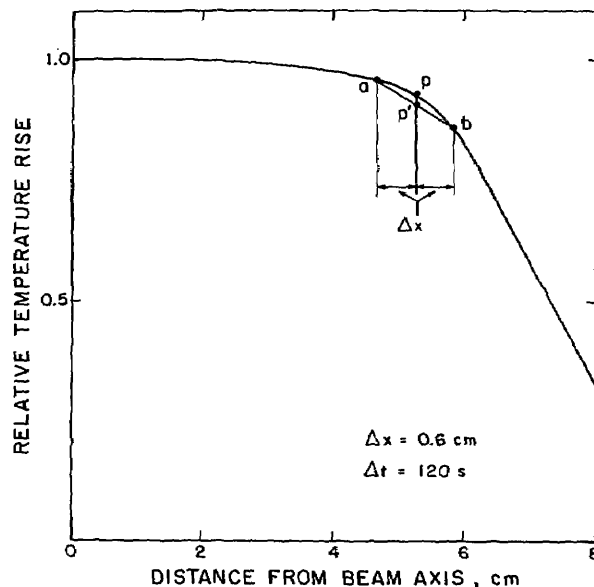


FIGURE 1. Illustration in applying the Schmidt numerical method to calculate an approximate temperature change in water at a point off the beam axis. The cobalt-60 beam passed through a square collimator. Conductive heat transfer was primarily radial.

perpendicular to the four sides of the square<sup>4</sup> of the smaller collimated beam. The curve was determined from densitometer measurements of film exposed under 5 g/cm<sup>2</sup> of polystyrene positioned perpendicular to the beam axis at 1 m from the source. Densitometer measurements through *p* and perpendicular to the above described heat flow (parallel to the side of the square beam) showed comparatively little variation in the region of *p*. Therefore, the component of heat flow along that direction could be neglected.

Assume that a beam pulse produced the relative temperature profile shown. It is desired to know the approximate percent decrease in temperature rise from *p* to *p'* after 120 s,  $\Delta t$ . The increments are related by the equation:

$$(\Delta x)^2 / (2\alpha \Delta t) = 1, \quad (2)$$

where  $\alpha$  is the thermal diffusivity (0.00144 cm<sup>2</sup>/s) of water (the thermal conductivity divided by the product of density and specific heat capacity). Solving the equation gives  $\Delta x = 0.6$  cm. The point of intersection of line *ab* with the vertical line through *p* gives the desired point *p'* which is 2 percent lower than point *p* (calculations

<sup>3</sup>The Schmidt method [10] is the best known, although a precursor of this method is described by Binder [11]. The method is further described in numerous publications and books on heat conduction, such as Refs. [12-16]. Reference [14] includes the procedures in applying the method to cylindrical and spherical heat flow.

<sup>4</sup>The heat flow pattern away from the irradiated region was much more complicated than the simple linear directional flow described here. Nevertheless, the described direction of heat flow is a good approximation considering the relatively large beam size, and this greatly simplifies the calculations that will be accurate enough for their intended purpose in determining an approximate heat loss correction for a run of given duration.

can be carried out to any degree of accuracy by testing results with decreasing values of  $\Delta x$ ). The calculations can be performed simply and rapidly with a programmed calculator. This was done to determine the change in the profile. The results showed that it would require 23 min, after applying the single-pulsed square-shaped beam, for the temperature rise of the thermistor on the axis to drop by 1 percent, and it would drop only 0.04 percent and 0.24 percent at the end of 3 and 10 min, respectively.

Another illustrative example is shown in figure 2 for the case of a broad beam pulse of 11 MeV electrons on water. At the end of 1 min the temperature rise  $Q$  would drop to  $Q'$ , a decrease of 0.8 percent. Temperature

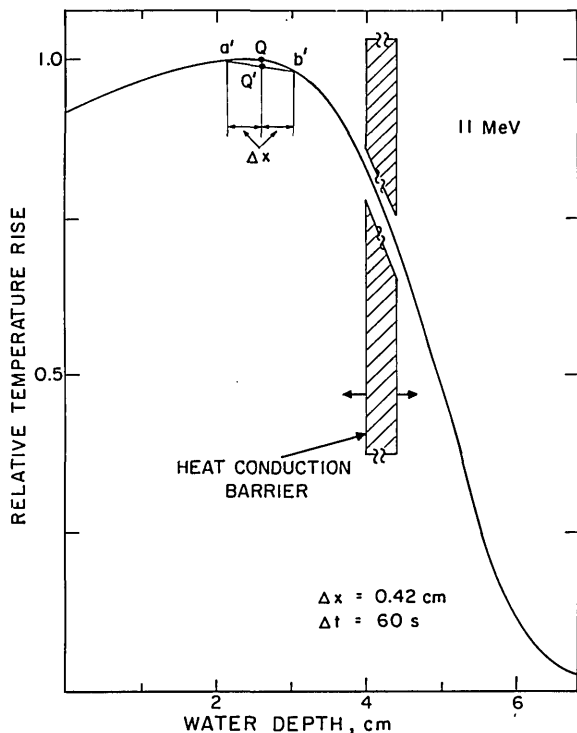


FIGURE 2. Illustrative sample in calculating the magnitude of a change in temperature at a point on the axis in water irradiated with a broad beam pulse of low energy electrons. Conductive heat transfer is primarily axial and can be decreased by a heat conduction barrier.

changes in long runs would be significantly affected by the steep drop in temperature beyond the peak. (A suitable heat conduction barrier, suitably positioned, in that region would decrease the effect; also, an irradiated non-water material can act as an excess heat source—explained later.)

The low thermal diffusivity of water results in small *theoretically calculated* temperature corrections even at positions of large changes in the temperature gradients. Essentially negligible corrections would then result from

measurements made immediately after a beam pulse or short runs of constant irradiation.

As will be seen, the calorimeter to be described was sensitive and stable. These features, combined with the large absorbed dose rates which can be delivered with medical therapy beams, are such that only about a minute or two of irradiation time would be needed. They would make the heat loss corrections small or negligible. Even these would tend to be corrected by extrapolating the final temperature drifts.

### 2.3 Convection

Perhaps a faulty belief of the omnipresence of convection in water containing buoyant forces was one of several reasons why the idea of the water calorimeter, if previously conceived by others, was dismissed as infeasible. This concern led to the construction of a calorimeter for measuring absorbed dose in a gelatin medium [17]. Although the present investigator was also initially concerned about convection, the calorimeter was still thought to be feasible if a series of closely spaced convection barriers was used above and below the plane defining the measurement point [1]. An initial design unnecessarily incorporated such a complicated construction. However, it was then learned that it had been well-known that buoyant forces can exist but the liquid will remain motionless until the Rayleigh number of about 1000 is exceeded [18] (reference [19] is an excellent article on convection). It would be instructive to give a brief description of the theory, followed by an example.

Consider the region before the peak of a temperature profile produced by an irradiation beam directed vertically downward. The temperature of the water in this region will increase with depth. This will cause a buoyant force that would be opposed by the viscous force of the fluid. The Rayleigh number is the product of the Grashof number ( $G_r$ ) that is a measure of the relative importance of the buoyant and viscous forces and the Prandtl number ( $P_r$ ) that is a measure of the ratio of the molecular diffusivity of momentum to the molecular diffusivity of energy:

$$G_r = g \Phi \rho^2 \Delta T d^3 / \eta^2,$$

$$\text{and } P_r = \eta C_p / k,$$

where  $g$  is the gravitational force per unit mass,  
 $\Phi$  is the volumetric expansion coefficient,  
 $\rho$  is the density,  
 $\Delta T$  is the temperature difference between two horizontal planes,  
 $d$  is the distance separating the planes,  
 $\eta$  is the viscosity,

$C_p$  is the specific heat at constant pressure, and  $k$  is the thermal conductivity.

Assume that two horizontal convection barriers (consisting of films) are immersed in water and that the lower barrier is 1 mK higher in temperature, which is roughly an upper limit that would be encountered in medical therapy beams. A calculation shows that the Rayleigh number is 1000 when the separation ( $d$ ) is 4 cm. Therefore, convection barriers (if needed) would consist only of a few and would be widely separated.

Measurements (described later) indicated no evidence of convection even in the absence of the barriers. Initial concerns about convection restricted the design of the calorimeter to vertically downward directed beams, but these calculations, in conjunction with experimental measurements described below, appear to also allow measurements in horizontally directed beams.

### 3. The Calorimeter

Figure 3 is a drawing that shows some features of the calorimeter. Two 0.25-mm diameter bead thermistors

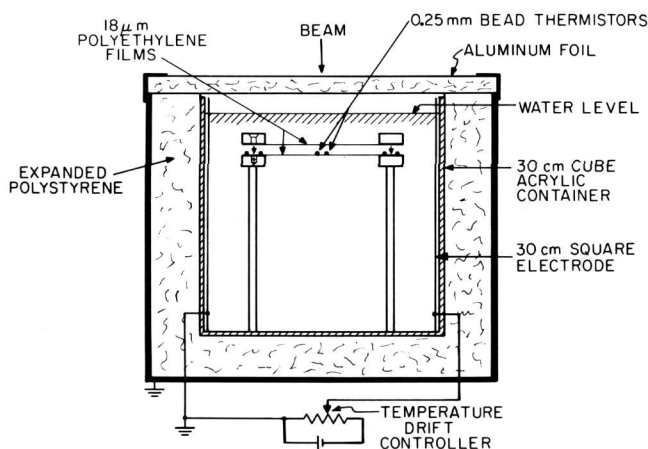


FIGURE 3. Essential features of the absorbed dose water calorimeter.

(separated by 2.5 mm) were sandwiched between two 18  $\mu$ m thick polyethylene films immersed at a 5 cm depth in water. The films were tightly stretched and clamped between two polystyrene rings (152 mm i.d., 214 mm o.d., and 23 mm total thickness). The rings were fastened with screws to three acrylic rods (polymethylmethacrylate) secured to the bottom of a 30-cm cube water container constructed of the same acrylic material. Two drift control electrodes, 30 cm square and 0.6 mm thick stainless steel, were secured against two opposite vertical walls inside the container. One electrode was connected to ground in order to ground the partially conductive once-distilled water. The drift control potential supply

consisted of several 67½ V dry-cell batteries placed in parallel, and these were connected across a 10-turn 50 k $\Omega$  helipot connected to the electrodes. A digital voltmeter and ammeter displayed the potential and current through the water. These values were recorded and used to calculate the power dissipation in the water, its resistance, and its electrical resistivity throughout a series of measurements. The depth of the water in the container was 26 cm. The calculated electrical capacitance between the electrodes of the filled container was about 200 pF.

An electrically grounded magnetic shield, consisting of 1.3 mm thick plates (not shown), surrounded the outer walls and the bottom of the water container. The container also was surrounded by a thermal shield of expanded polystyrene which, in turn, was surrounded by an electrically grounded shield of aluminum. An easily removable lid was snap-secured to the exterior duraluminum container. The lid thickness was 4 mg/cm<sup>2</sup> of aluminum and 75 mg/cm<sup>2</sup> of expanded polystyrene. The external dimensions of the outer container were 45 x 45 x 40 cm high, and the mass (without water) was 31 kg.

Figure 4 is a top view photograph that shows additional interior details. The signal leads from the thermistors passed through Teflon spaghetti and a connector shown on the top of the rings. Silicone rubber and a rubber sleeve waterproofed the connector. (Additional details that describe the emergence of the leads are given in a previous report [1]). The connector and the three

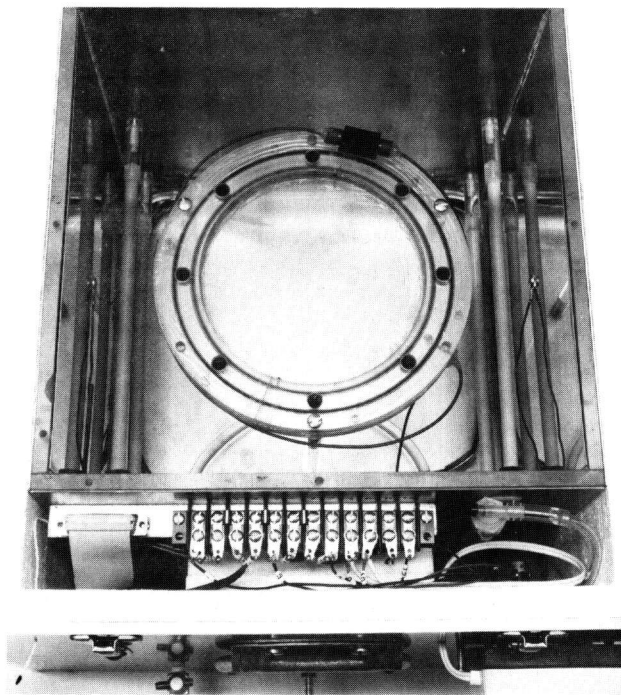


FIGURE 4. Top view photograph showing calorimeter internal details.

securing screws permitted easy placement or removal of the detector assembly. The left and right sides show the stainless steel drift control electrodes, each showing reflections of two horizontally mounted immersion heaters (400 W total power for the four heaters) enclosed in quartz sheaths. Not visible between two of the heaters was a horizontally positioned commercial temperature sensor in a stainless steel sheath. A perforated plastic tube was positioned along the bottom horizontal interior edges of the tank for the purpose of agitating the water with air, oxygen, or nitrogen at a flow rate near 1.5 L/min. The gas was made to flow directly upward near the four vertical corners of the tank to effectively prevent gas bubbles from migrating to the bottom surface of the lower film. The lower part of the photograph shows the connecting points for wires between the two enclosures of the calorimeter. The wires, immersion heaters, perforated tube, and the temperature sensor all entered the water tank through seals below the water surface for easy removal of the lid. The lower left-hand corner of the photograph shows another temperature sensor for measuring the temperature outside the exterior box. Both probes were connected to an instrument that displayed temperature with a resolution of 0.01 K.

Figure 5 shows the external features. The lid is shown snap-secured to complete the thermal and main electrostatic shielding. An aquarium pump, shown mounted

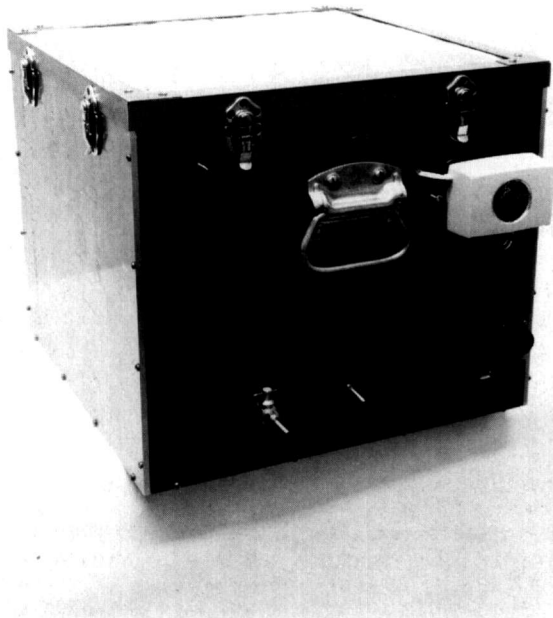


FIGURE 5. Photograph showing calorimeter external details.

adjacent to the handle, was occasionally used to agitate the water. Agitation with oxygen or high-purity nitrogen was accomplished by connecting those supplies with the pump outlet connecting tube. A valve (shown at the lower left) was connected to the water tank with a plastic tube at a position near the bottom of the tank. A tube connection from the valve outlet to an external column of water would permit micrometer measurements down to the water surface which would provide a convenient way of accurately measuring changes in the depth of the immersed thermistors, after water is added to or removed from the column.

A tube fitting (to the right of the valve) was connected to the same nitrogen or oxygen supply used to agitate the water, and after agitation a small amount of the gas continued to flow between the two containers to prevent air from diffusing back onto the water surface. Signal lead and control cables (16 m long) were attached to the connectors shown at the lower right.

If necessary, the temperature around the calorimeter could be accurately controlled by means of a structure placed over the calorimeter. This four-sided acrylic structure contained a temperature sensor, heater, and fan mounted on an inside wall. The lid of this structure was expanded polystyrene with a polyethylene film covering the beam entrance window.

#### 4. The Detector

The amount of non-water materials near the thermistors must be kept at a minimum. Those materials act as generators of excess heat that must be sufficiently dissipated to cause negligible effects, or the effects must be calculated so that corrections can be made. The 25  $\mu\text{m}$  diameter thermistor leads (90 percent platinum—10 percent iridium, and nearly 1 cm long) were soldered to 80  $\mu\text{m}$  diameter copper wires. The excess length of each soldered junction was cut away with a surgical blade. Each junction was then attached to the lower film with a minimal amount of silicone rubber. Each pair of junction points was separated about 15 mm, and the copper wires were separated by at least that amount. This separation permitted more rapid dissipation of excess heat from the wires compared to wires placed close together. The length of the copper wires was made to be about 14 cm before being allowed to exit from the inside diameter of the rings. Just prior to securing the rings together, several scattered spots of silicone rubber were placed on the lower film, at least 2 cm away from the thermistors and wires. The spots were compressed immediately after securing the rings, adding further assurance of closer film contact. Close examination at the thermistors revealed bulging on both sides of the films which were presumably in good thermal contact

with the thermistors. There were observed non-uniform contacts of the films with the wires. Contact between the remainder of the films looked good. All thermal contacts were undoubtedly improved by water pressure on both sides of the films.<sup>5</sup>

The assembled detector was examined under a microscope to view the films for tiny weak spots which were sealed by application of tiny amounts of silicone rubber (care was taken that obvious weak spots were not in the immediate vicinity of the thermistors).

The thermal effects of the films, beads, and bare Pt-Ir leads were calculated from theoretical solutions [20]. The effects of the films on the thermistors were calculated by using a slightly modified form of the theoretical solution (eq (10), p. 76 in [20]). Figure 6 shows the calculated excess thermistor temperature rise caused by the films, in percent, as a function of time after a 3-min irradiation run. The correction is small and it decreases as the duration of the run increases. The correction at the instant of beam turn off after a one-, two-, or three-minute run is 0.31, 0.22, and 0.18 percent respectively. The small variable corrections can readily be applied to the observed calorimeter signals, after

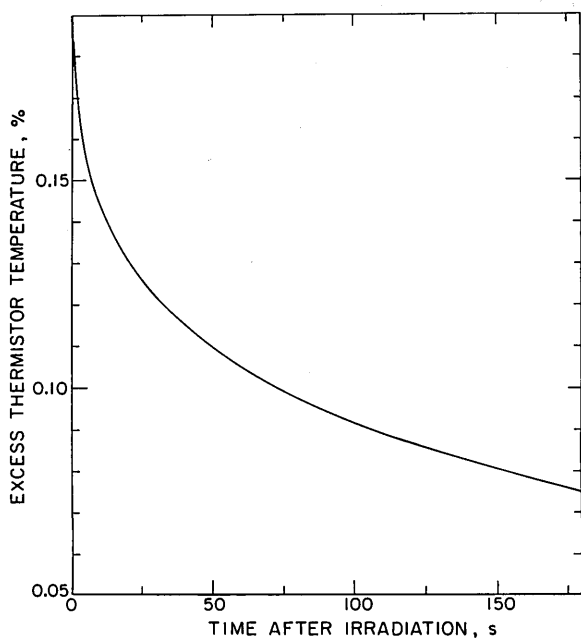


FIGURE 6. Excess thermistor temperature rise caused by the two immersed 18  $\mu\text{m}$  polyethylene films irradiated for three minutes.

<sup>5</sup>Calculations showed that even if the plane between the films (at a 5-cm depth of water) acted as an impervious conductive barrier to heat flow after a pulse from a broad parallel beam of cobalt-60 radiation, but the thermistors represented the average temperature at the water boundaries, then such a barrier would cause an error in measurement of only 0.03 percent at the end of 3 minutes.

beam turn off. The corrections are taken to be accurate considering the well defined geometry and known thickness of the films. The effects of the beads and wires were calculated by considering them as isolated but continuous point and line sources of heat in water, the theoretical solutions being formulas (2) and (5), respectively, on p. 261 in reference [20]. Their effects were negligible even though the geometry assumed here was not realistic in practice. Results of the calculations showed that their separate excess temperature effects would essentially disappear, within 0.01 percent, a few seconds after beam turn off. The fast disappearance of excess heat from the beads and wires is a result of spherical and cylindrical flow of heat, respectively, away from them; whereas it is slower from the films because of the linear flow of heat.

Polyethylene appears to be a good choice for the sandwiching films. In regard to generated excess heat, this material produces a smaller effect for a given thickness than, for example, Mylar (polyethylene terephthalate) by approximately a factor of 1.7—the ratio of their specific heat capacities, which is the dominant factor causing that effect. In regard to the water absorption characteristics of these two materials, polyethylene is lower by at least a factor of 20 (according to data listed in reference [21]). Early tests showed that polyethylene films provided high electrical insulation from water. In one test two 30  $\mu\text{m}$  films sandwiched two 15 cm diameter aluminized plastic foils, each 6  $\mu\text{m}$  thick. The aluminized layers (electrically connected) were against the 30  $\mu\text{m}$  sandwiching films. This unit was kept immersed in water for two weeks while daily electrical resistance measurements were made between the aluminum and water. The geometry, therefore, was such that leakage resistance anywhere through the films would be included in the measurements. On the first day, the resistance was  $5 \times 10^{12} \Omega$ . On the other days, the measurements varied from  $1.3$  to  $4.0 \times 10^{11} \Omega$  which were still sufficiently high resistance values.<sup>6</sup> (The electrical resistance between two points in the water was negligible in comparison with the resistance through the films). The sandwiching films were not previously inspected under a microscope for weak points (only visual observations were made). Polyethylene films have a desirable property in that they can be slightly stretched

<sup>6</sup>Perhaps the best test for intolerable leakage resistances can be judged by observation of the recorded bridge output signal, using an amplifier gain normally used for measurements. Small variations in leakage resistance would likely be present, and this could result in large and erratic noise particularly when measuring small output signals. This was never observed with the detector described in this paper (the detector was immersed only during the course of daily measurements). If internal difficulties from this source occur, the detector can easily be removed for repair or replaced. This simple procedure is in striking contrast to painstakingly rebuilding a calorimeter constructed of sealed nested bodies made of solid material.

without apparent damage. This eliminates wrinkles when the films are stretched around the rings with elastic tape during detector fabrication and assembly.

The detector polystyrene mounting rings had a specific heat capacity nearly one-third that of water. The absorbed dose rate in the two materials is approximately the same. Therefore, a pulse of broad beam irradiation will cause an instantaneous rise in temperature about three times higher in the rings than in the surrounding water. Heat produced in them, during typical 3-min irradiation runs, caused a negligible effect on the centrally located thermistors. An upper limit to the effect was calculated by using theoretical results listed in table J.1 of reference [12]. The table would apply to the rings being infinite in extent in the vertical direction and the cylinder receiving a sudden change in temperature which remains constant with time. The result showed that 20 min would be required for thermal conduction from that cylinder (152 mm i.d.) to raise the temperature of the thermistors by 0.1 percent of its initial temperature rise. In reality, the total thickness of the rings was small, the temperature of the rings decreased rapidly from loss of heat (because of the small specific heat capacity), and the heat conducted from the inside lateral ring surface was diffuse in direction. Consequently, many irradiation runs had to be made before the thermistors significantly sensed the heat conduction, and whenever they did the effect helped to control and speed the measurements, as will be explained later.

### 5. The Wheatstone Bridge

Figure 7 is a drawing of the simplified Wheatstone bridge circuit that was used for determining both the fractional resistance change ( $\Delta R/R$ ) in the balancing resistor ( $R$ ) and the fractional change in thermistor resistance per degree temperature rise ( $S$ ) of each thermistor,  $C$  and  $J$ . A selector switch (not shown) could replace each thermistor with an external resistor of equal value (the power through the replaced thermistor remaining constant by means of an auxiliary variable power supply). Also provided were means for independently varying the power through each thermistor.<sup>7</sup>

Each thermistor had a nominal resistance value of 3 k $\Omega$  at the water bath operating temperature of about 23  $^{\circ}\text{C}$ . The bridge power supply was two 1.35 V mercury cells that could be switched in series or in parallel. These were in series with a variable resistor,  $R_1$ , that consisted

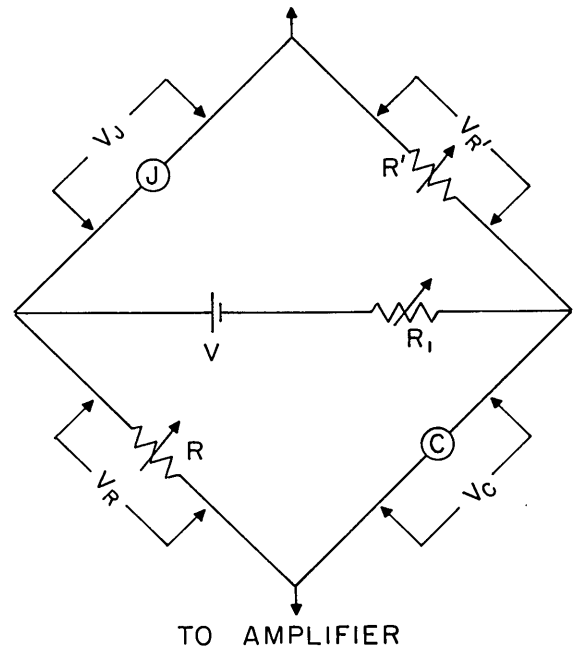


FIGURE 7. Wheatstone bridge circuit used for determining the absorbed dose and the absolute sensitivity of the thermistors.

of a 10-turn helipot and a selector switch that placed additional resistors in series. These arrangements permitted a large range of power dissipations in the thermistors to study their effects on the measurements of absorbed dose, thermistor sensitivities, and possible water convection in the immediate vicinity of the thermistors.

A selector switch permitted measurements of the potentials  $V_C$ ,  $V_J$ ,  $V_R$ , and  $V_{R'}$ , between pairs of points along each bridge arm. Prior to a series of measurements, the resistor  $R'$  was adjusted until  $V_J$  was essentially equal to  $V_{R'}$ . Then resistor  $R$  was adjusted to bridge balance. This made the  $J$  thermistor resistance value,  $r_J$ , essentially equal to the resistance value of  $R'$ , and the  $C$  thermistor resistance value,  $r_C$ , essentially equal to the balancing resistance value of  $R$  (external lead resistances had a small effect). This bridge condition resulted in minimal changes in thermistor powers during the course of the runs. The four measured potentials were also used to determine the sensitivity ( $S$ ) of the thermistors.

The dc output of the bridge was fed into a 16 m double-shielded signal cable connected to a nanovolt null detector that consisted of a chopper, ac amplifier, and demodulator system followed by a dc amplifier. The signal cable consisted of nine pairs of 640  $\mu\text{m}$  diameter copper wires, each pair separately shielded. A change in room temperature will change the resistance of the signal leads and that will cause a change in the bridge output. This effect was minimized in the following manner: the two wires within a pair would presumably be closer to

<sup>7</sup>The circuit features were the same as for the absorbed dose graphite calorimeter described in reference [8]. These permitted a rapid means for making important tests to determine the consistency of the measurements in the  $C$ ,  $J$ , and  $C + J$  modes that are described later.

the same temperature than two wires from separate pairs. Therefore, leads from a pair were positioned in adjacent arms of the bridge that would essentially remain in balance for equal resistance (temperature) changes in the leads. In a similar manner, to further decrease the effect, separate leads from two other pairs were placed in parallel to the first pair to decrease the conductive path arm resistance to 0.3  $\Omega$ .

Optimum measurement conditions required that the resistance values of the components in the variable resistance arms, R and R', depended on whether the bridge was to be used for measuring the sensitivities of the thermistors (when the water bath temperature was made to vary from 9-34 °C) or absorbed dose (when the water bath temperature was essentially constant). For the former, R and R' were decade resistors which provided dial resistance values of 10(0.1+1+10+100+1000)  $\Omega$  and 10(1+10+100+1000+10,000)  $\Omega$ , respectively. Each had a resistance accuracy of 0.05 percent. Their terminals were shielded by grounded metal enclosures surrounded by thermal insulation. For absorbed dose measurements (when very small signals at a high amplifier gain had to be measured), R was shunted with a 1.5 k $\Omega$  resistor and the combination was in series with a 1.55 k $\Omega$  resistance combination, while R' was shunted with a 2.5 k $\Omega$  resistor and this combination was in series with a 0.8 k $\Omega$  resistance combination. These resistance arrangements attenuated possible effects of contact resistance changes in the dials and also permitted desirably small recorder-pen deflections with changes in the smallest dial steps.

Effects of thermal electromotive forces (emfs) were decreased mainly by providing thermal insulation around the bridge circuit enclosure. The above-mentioned resistors were wire-wound (non-inductively), and it was necessary to enclose them within that insulation. All components were soldered with an ordinary solder alloy of 60 percent tin, 40 percent lead. An emf stability test was made by connecting a thermally insulated mini-box (at the calorimeter end of the signal cable) containing two fixed wire-wound resistors that replaced the thermistors. A prolonged test indicated entirely satisfactory stability; and although changes in temperature drift were observed at times, they were too slow and predictable to impair the precision of measurements. This setup provides an additional test in determining if problems (if they do occur) are caused within or exterior to the calorimeter outer container.

## 6. Thermistor Sensitivity Measurements

The thermistor resistance value ( $r$ ) at a given absolute temperature ( $T$ ) is given by the well-known empirical expression:

$$r = r_0 e^{\beta(1/T - 1/T_0)}, \quad (3)$$

where  $r_0$  is the resistance at temperature  $T_0$  and  $\beta$  is the "material constant."<sup>8</sup>

The sensitivity of a thermistor ( $S$ ) is defined as  $(1/r)(dr/dT)$ , which gives

$$S = -\beta/T^2. \quad (4)$$

The sensitivity is nominally 4 percent per degree and varies by seven parts per thousand per degree at room temperature. Equation (3) can be reduced to linear form:

$$y = \beta x + \theta, \quad (5)$$

where  $y = \ln r$ ,  $x = 1/T$ , and  $\theta = \ln r_0 - \beta/T_0$ , a constant.

The values  $\beta_C$  and  $\beta_J$  for each thermistor were derived from resistance measurements ( $r_C$  and  $r_J$ ) determined *within* the beads as a function of temperature *within* the beads. Least-squares fits of the data were applied to eq (5).

Figure 8 shows smooth plots of the C and J thermistor resistances as a function of their temperatures from 9-34°C. Table 1 lists the results of the analysis. Column 1 shows the different months in which the measurements were made. Column 2 shows the chosen temperature ranges, and column 3 shows the number of data points in those ranges. Columns 4 and 5 list the calculated values of  $\beta_C$  and  $\beta_J$  for the C and J thermistors, respectively. In all cases, the least-squares fits resulted in variations in the coefficient of correlation that differed from unity by less than one part in 10,000. A value of unity would represent a perfect fit for the data.

An examination of the data indicates that sufficiently accurate and repeatable results would be obtained from about ten data points over a temperature span of approximately 6 degrees above and 6 degrees below the calorimeter operating temperature. The values of  $\beta_C$  and  $\beta_J$  differed by 0.4 percent. A mean value  $\beta$ , of 3202 K  $\pm$  0.1 percent was used for the final result. Careful measurements showed that there was no detectable evidence of variation in  $\beta_C$  or  $\beta_J$  at eight different values of thermistor power dissipation from 6-200  $\mu$ W.

The water bath temperature,  $T_w$ , was measured with a separate sensor probe connected to a circuit that displayed temperature with a resolution of 1 mK. The probe

<sup>8</sup>Although  $\beta$  increases slightly with increasing temperature [22,23], it may be considered constant over temperature spans of approximately 40 K, depending on the thermistor material and the absolute temperature of the center of the span [24]. Furthermore, slight effects of variations in  $\beta$  will be decreased by analyzing data within equal temperature spans around the calorimeter operating temperature, near 23 °C.

was a calibrated commercial quartz thermometer. Tests showed that movement of the probe to different positions in the water (after agitation) indicated no significant differences in observed temperature. Another test showed that the power dissipation in the probe raised its temperature by 4 mK, which was subtracted from the displayed values. The Wheatstone bridge electrical power

dissipations in the thermistors,  $P_C$  and  $P_J$ , caused them to rise,  $\Delta T_C$  and  $\Delta T_J$ , above the water temperature,  $T_w$ . The mean values of the differential temperatures,  $\Delta T$ , were determined experimentally (shown below) and were later added ( $\sim 24$  mK for most of the measurements) to the values of  $T_w$  displayed on a meter. A calculation showed that a systematic error as large as 100 mK throughout the temperature range would have resulted in an error in  $\beta_C$  or  $\beta_J$  of only 0.07 percent.

When the Wheatstone bridge was balanced, the values  $R$ ,  $R'$ ,  $V_C$ ,  $V_J$ ,  $V_R$ , and  $V_{R'}$  were recorded and stored in the registers of a programmed calculator. Included in the computer program were the effects of all lead resistances external to the beads, including the effects of the exact locations of the four potential measurements. The computer printouts gave values of  $r_C$  and  $r_J$  (the electrical resistances *within* the beads), and  $P_C$  and  $P_J$  (the electrical powers dissipated *within* the beads). These results permitted determinations of small temperature corrections,  $\Delta T$ . Then  $T = T_w + \Delta T$ , for use in eq (5).

Figure 9 shows normalized plots of the equilibrium thermistor resistances,  $r_C$  and  $r_J$ , as a function of thermistor electrical power dissipations,  $P$ , in microwatts. The measured values for  $r_J$  are not shown. The resistances,  $r_J$ , were about 5 percent higher than  $r_C$ , but was normalized to  $r_C$  (at  $P = 0$ ) to better show the difference in slopes of the linear fits of the form  $r = mP + n$ . The small difference in slopes was presumably caused by differences in thermal coupling between the thermistor beads and connecting wires with the surrounding

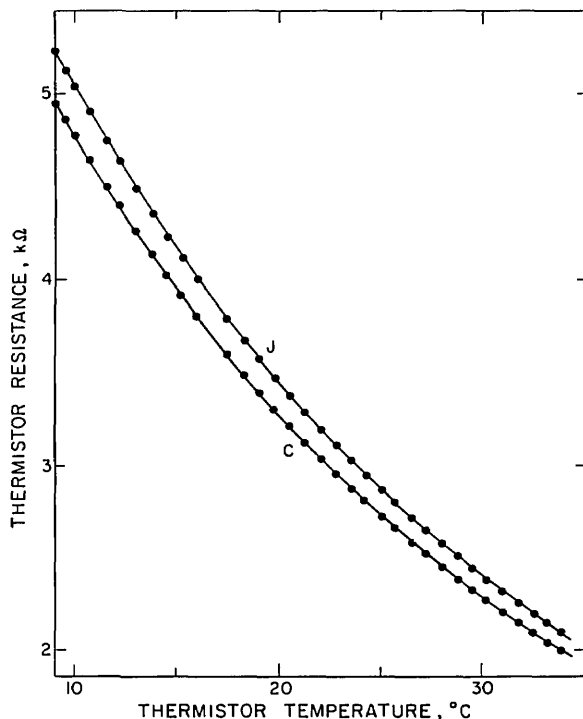


FIGURE 8. Plots of measured thermistor resistances versus temperature.

TABLE 1. Measured values of  $\beta$ .

Date (1980)	Temperature range (°C)	Date points	$\beta_C$ (K)	$\beta_J$ (K)
March	13-34	28	3193.3	3207.3
"	16-31	20	3195.0	3209.1
"	19-28	13	3194.4	3205.2
"	20-26	9	3196.1	3204.7
			<u>3194.7</u>	<u>3206.6</u>
Sept.	14-33	21	3189.5	3208.5
"	16-29	14	3183.4	3210.4
"	19-26	8	3195.8	3206.7
"	20-25	6	3202.2	3201.3
			<u>3199.7</u>	<u>3202.2</u>
Nov.	12-33	8	3192.9	3204.2
"	16-30	6	3198.7	3212.1
"	19-27	4	3207.1	3221.7
			<u>3201.5</u>	<u>3212.7</u>

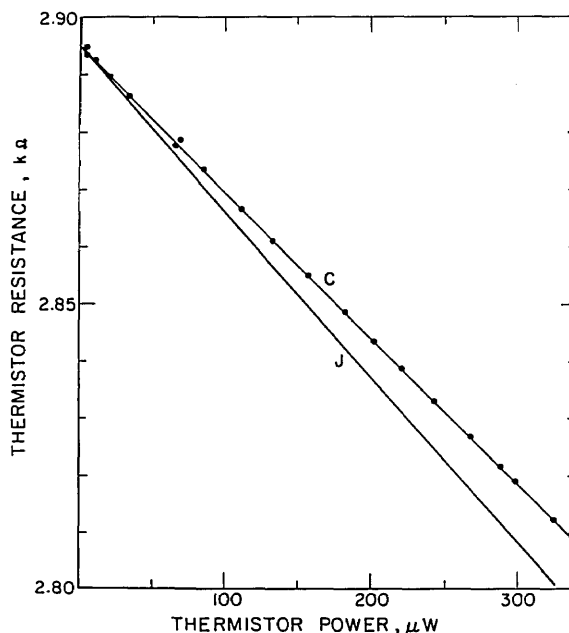


FIGURE 9. Normalized plots of equilibrium thermistor resistances versus electrical power dissipations. Data points are plotted for C curve only.

films and water. The plots were converted to temperature scales by the equation:

$$\Delta T_{C,J} = \frac{m_{C,J} P_{C,J}}{n_{C,J} (\beta'_{C,J} / T_w^2)} = \phi P_{C,J}, \quad (6)$$

where  $\beta'_{C,J}$  were first approximations of  $\beta_C$  and  $\beta_J$  determined from measurements of resistances versus  $T_w$  ( $P_C$  and  $P_J$  were about  $5 \mu\text{W}$  so the values of  $\Delta T_C$  and  $\Delta T_J$  were negligible for these determinations). Plots like figure 9 were made at eight operating bath temperatures from 10-33 °C. The mean value of  $\phi$  for the two thermistors was  $2.6 \text{ mK}/\mu\text{W} \pm 1$  percent mean error, and was essentially constant over this temperature range.

Equation (1) can now be put in a more usable form:

$$D = (1/2)(\Delta R/R)(\bar{\beta}^{-1})(T_w + \bar{\Delta T})^2(c) \quad (7)$$

where  $\bar{\Delta T} = 2.6 \bar{P} \text{ mK}$ , (8)  
and  $\bar{P}$  was the average power, in  $\mu\text{W}$ , of the two thermistors.

## 7. Calorimeter Setup

The following procedure was followed each morning in preparation for irradiation runs. The calorimeter (fig. 3) was empty of water, the lid was removed, and zero potential was across the drift control electrodes. A horizontal line-of-sight of a telescope (mounted on a distant vertical scale) was used to indicate a 1 m distance from the cobalt-60 source. The thermistors were to be placed along this line. A bar was placed across the top of two opposite edges of the 30-cm cube container. A depth micrometer was placed on the bar and a measurement (A mm) down to the film was made to a accuracy of about  $\pm 0.025$  mm. The line-of-sight of the scope was then raised by A mm. The height of a sturdy motorized platform (on which the calorimeter rested) was adjusted until the line-of-sight coincided with the plane between the micrometer base and bar (this was later checked when the tank was full of water). This placed the thermistors at the reference distance of 1 m, the same place at which previous measurements were made with the NBS absorbed dose graphite calorimeter.

The next step was to place the plane of the thermistors at a 50 mm depth in water, with a micrometer reading of (A-50) mm to the water surface. Water was then allowed to flow into the container, and as it rose air was trapped within the boundaries of the film and lower ring. The trapped air was completely removed with a suction syringe. When electrical contact between the micrometer and water was made, the water flow was stopped. A measurement to the water surface usually differed

slightly from the required (A-50) mm value. This difference was eliminated by adding or withdrawing the required volume of water with a graduated hypodermic syringe. The lid was then snap-secured, and temperature control was ready to begin.

## 8. Temperature Drift Control

When the calorimeter was being constructed, two seals were installed at the bottom of the water tank for the use of cooling coils to aid in the temperature control, if necessary. These were never put into use because the method of controlling temperature drifts described below was found to be adequate.

Initial temperature measurements made with the sensor probes indicated that the water bath was always about 1°C cooler than the immediate surroundings. The reason is that on the previous day the storage bottles containing the water were placed at floor level where the temperature was cooler than at the elevated calorimeter. This condition helped to bring the calorimeter under control.

The initially cool water started to cool the container walls and polystyrene rings (the thermal diffusivity and thermal conductivity of the polystyrene were lower than that of water by approximately factors of two and five, respectively). The calorimeter is most stable when the water bath temperature is raised to the environmental temperature. Water agitation was started and the immersion heaters were turned on and then turned off after approximately 4 min to allow the temperature difference between the water and the ambient (near 23 °C) to settle within 0.2 °C (daily room temperature variations were near 0.2 °C). At this point, the average temperature of the rings (the principal structure nearest the sensors) lagged too far behind the water bath temperature, but the agitation continued for about 20-30 min (a small gas flow within the outer container continued throughout the day). At this point, the lag in ring temperature was desirably small. The agitation was stopped and a period of approximately 10 min was allowed for the water turbulence to subside. The gain of the amplifier was increased and the drift of the bridge output as indicated by the recorder was observed. The recorder at first always indicated a characteristic upward drift (temperature increase) that gradually peaked and then turned into a small (and desirable) cooling drift. The reason for this behavior is that at first the Wheatstone bridge electrical power produced sharp temperature gradients around the thermistors, which gradually approached a steady state, but which were then overcome by conduction of heat to the cool rings. A potential was then applied across the drift control electrodes, and adjusted until the drift was greatly reduced. In this way, a temperature drift was

quickly brought under control<sup>9</sup> by increasing or decreasing the electrical heating of the distilled water which was slightly electrically conductive.

After continued agitation (~30-40 min), the cooling drifts at times were small enough to allow runs with zero potential across the electrodes.<sup>10</sup> In theory, prolonged agitation followed by a long wait should result in an initial zero drift, but in practice external effects could be significant.

On two days (out of approximately 40), there were long and steady initial heating drifts when the potential across the plates was zero, a seemingly uncontrollable situation. However, control was easily restored. The water bath was agitated and raised in temperature about 0.1 °C. This made the rings again lag behind the water temperature, again causing a slight cooling of the thermistors, and thus permitting drift control. This procedure is better than attempting to control the situation by initially starting with too high a power between the electrodes (zero power was used although a small initial power would be satisfactory), and then decreasing the high power to control small heating drifts. In a room well regulated in temperature, drift control is relatively easily achieved when the initial temperature of the water is not greater than room temperature. Excessive initial temperature of the water may result in undesirably large cooling drifts.

Helpful to the understanding of the drifts is the degree to which the rings lag behind the water in temperature. Consider, for example, that the rings and water are initially at a uniform temperature and then the water is suddenly raised in temperature by one degree and water agitation is started. The changes in temperature at the geometric center of the ring cross section (with the rings considered as one piece with dimensions of 23 x 65 mm) were calculated from existing tabulated results derived from theoretical calculations. At 10, 20, 30, and 40 mins, the temperature differences from water would be about 500, 180, 60, and 20 millidegrees, respectively.

The effectiveness in controlling drifts depends on the axial and radial absorbed dose profiles. Successive

<sup>9</sup>This is a vital feature that calorimeters must have; otherwise, these instruments are too unwieldy, which discourages their construction and use. In the NBS absorbed dose graphite calorimeter [8] drifts were also quickly brought under control in its four nested bodies. Described in the cited reference is the method of momentary observation of the drift in each body followed by selective temperature adjustments to bring the bodies to a state of temporary equilibrium for a long enough period to complete at least several irradiation runs.

<sup>10</sup>Experience has shown that these conditions were relatively easy to attain—particularly as the drifts would become more negligible in comparison with higher dose rates available with medical therapy beams. If the drifts are negligible throughout the container and no control is needed, then, as pointed out in references [1] and [2], sensors could be placed in a pattern between the films, and any number of these arrays can be placed at desired depths in a water (or other liquid) phantom. A fast read-out system, in a single irradiation run, could then measure simultaneously the response of each sensor as a function of time to give a dose profile.

cobalt-60 runs with a collimated beam, such as the one having the radial profile shown in figure 1, will cause the irradiated portion of the water to rise increasingly higher in temperature<sup>11</sup> compared to the water at larger radial distances. This caused an increased cooling drift which was largely counteracted by increasing the potential across the immersed electrodes. To further decrease the effect of radial heat flow, and to speed the measurements, most investigative studies were made mainly with a broad beam.

## 9. Calorimeter Performance

Figure 10 shows a small portion of a bench test made immediately after completion of the present third model of the calorimeter. The thermistors were at a 2-cm depth in water, and the values of  $P_C$  and  $P_J$  were 164 and 156  $\mu\text{W}$ , respectively. Time increases from right to left. The initial drift shows a rapid cooling rate that was quickly decreased by changing the potential across the electrodes from 0 to 45 V (the downward spike was caused by the manual adjustment of the potential). Opening a door to the test room caused the shown upward increase in signal that remained constant. Closing the door eliminated the signal that represented about a 12  $\mu\text{K}$  equivalent temperature rise of the thermistors. (That the effect might have been caused by electromagnetic signals entering the room was ruled out by tests.) The signal was always repeatable and became less noticeable as the thermistor powers decreased. Two large air ventilators were blowing in the room. A pressure gauge showed that opening the door caused about a 13 Pa (0.1 mm Hg) decrease in air pressure. This may have microscopically increased the spacing between portions of the thermistors and their leads to the films. This would decrease the rate of heat transfer that would cause the thermistors to rise to new equilibrium temperatures.

After closing the door, the cooling drift was again rapidly decreased by increasing the potential to 50 V, and still further by applying 53 V eleven minutes later. The test was continued for approximately 75 min. Subsequent drifts (not shown) were further decreased by increasing or decreasing the potential as required. The bench test was continued for several days with the recorder running continuously. The recorder showed no sudden changes in drift that would impair the precision of measurements during irradiation. This condition also prevailed in the experimental room during most days of operation; but when large changes in air circulation were felt, noticeable changes in drift were observed.

<sup>11</sup>If necessary, this temperature pattern (that results in an increased cooling drift) can be quickly erased by momentarily agitating the water. Every advantage should be taken of the mobility of a liquid and drift control electrodes to bring the calorimeter into operation and to speed the measurements.

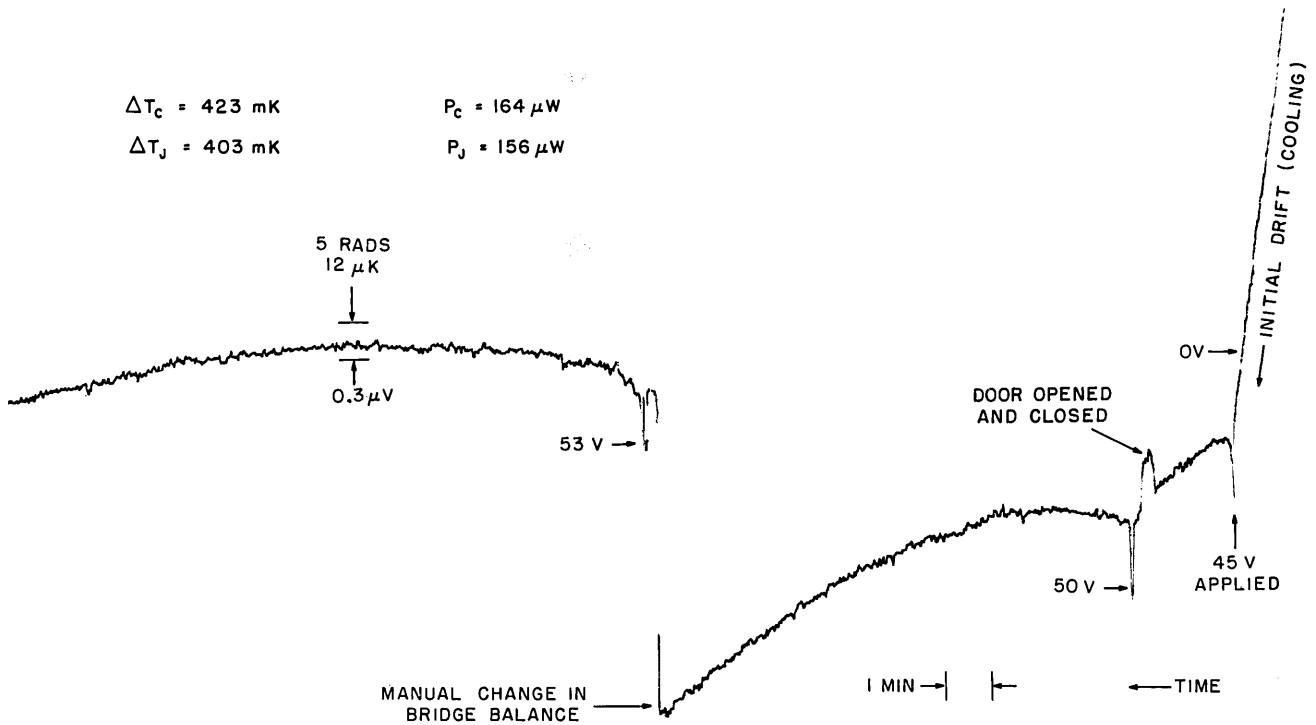


FIGURE 10. Early bench test illustrating the calorimetric sensitivity, stability, and rapid control of large temperature drifts.

The rapid initial cooling drift shown in figure 10 is somewhat severe (although controllable, but, as mentioned, the test was made immediately after completion of the calorimeter and before experience with the behavior was gained. Moreover, the procedure followed in subsequent tests, as discussed in the previous section, was different. In this first test, the bath was raised in temperature by 1 degree and agitated for only 3 min (not the 20-30 min as recommended). About a half hour later the recording began as shown. The rapid initial cooling was apparently caused by too much heat conduction to the polystyrene rings that lagged too far behind in temperature. Although the applied potentials greatly counteracted this effect, heat conduction to the rings continued and caused the curvatures shown. Even this curvature can be considered small if a typical medical therapy dose rate of 2 Gy/min were applied for 1 min. The recorder pen would deflect 40 times greater than the distance indicated by the 5 rads shown. Furthermore, the initial and final drifts would need to be extrapolated only 0.5 min to the mid-run. When lower dose rates are to be measured over longer periods of time, the quality of measurement would require traces with smaller curvature so that drifts could be extrapolated to the mid-run with precision and accuracy.

Figure 11 shows typical broad beam cobalt-60 irradiation runs. The dose rate was 1.1 Gy/min (18 mGy/s) ap-

plied for 3 minutes. The thermistors were at a 5-cm depth in water, and the values of  $P_c$  and  $P_j$  were 9.6 and 9.1  $\mu\text{W}$ , respectively. The recording was made with an amplifier gain setting which was three times greater than that used to record the test run shown in figure 10. When the initial drift (shown on the right in figure 11) was considered small and predictable, the beam was turned on and  $R$  was adjusted around the null (mid-scale) until the beam was turned off after three minutes. The abrupt spikes shown are the result of this manual change in  $R$  (the sum total of the pen deflection was 44 times greater than the indicated distance for 7.5 rads). The initial and final drifts were extrapolated toward the mid-position (1.5 min after start of the run for this case). The distance between the two points of intersection of the extrapolated drifts was converted to an equivalent change in  $R$  from a chart calibration. These combined with the values of  $R$  during the initial and final drifts were used to calculate  $\Delta R/R$  for use in eq (7).

The final heating drift in the first run shows that the drift increased slightly compared to the initial drift. Although it can also be considered small, it was decreased before starting the next run. The resistor  $R$  was adjusted to move the pen to the mid-position of the recorder chart. The potential across the electrodes was then decreased from 30.5 to 29 V that decreased the electrical heating power in the 25 L of water from 157 to

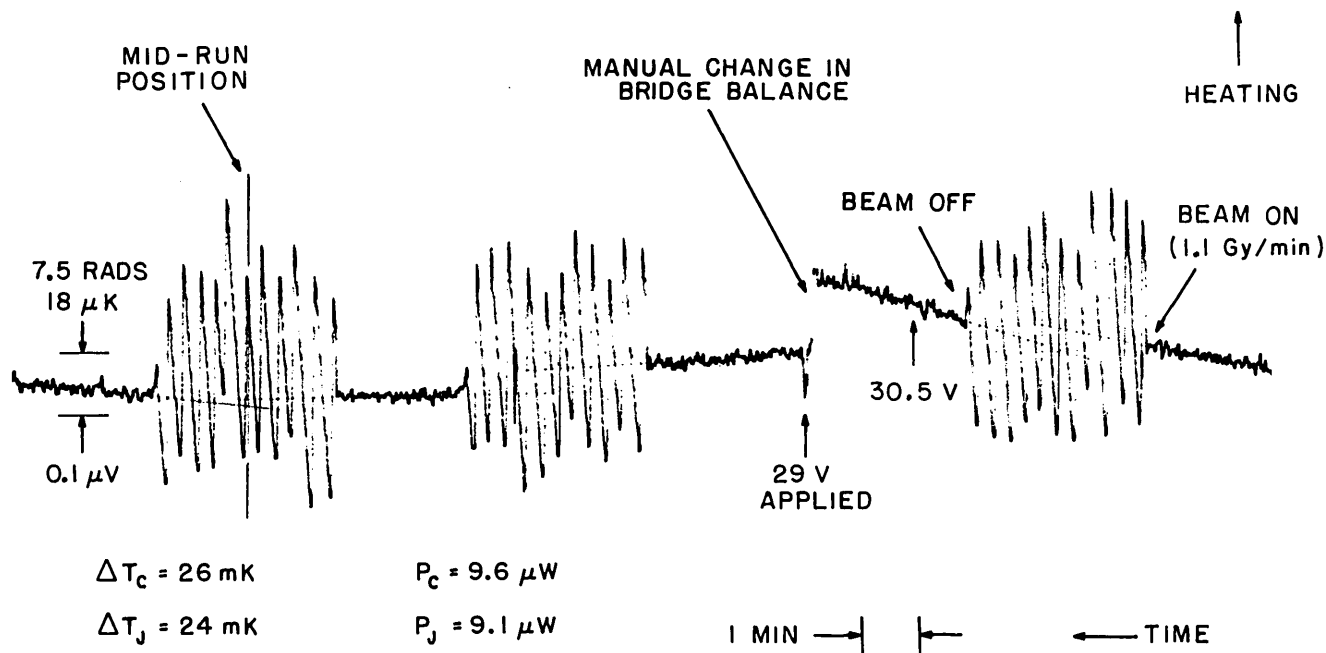


FIGURE 11. Recorder tracings illustrating small and quickly controlled drifts, large signal to noise ratio, and the rapidity of broad beam cobalt-60 measurements.

146 mW. Several more runs were made without further adjustments in potential.

Observation of all the drifts showed that there was an overall tendency for the drifts to turn slightly upward (heating). This was presumably caused by the broad beam heating of the polystyrene rings that rose three times higher in temperature than the water (as explained previously). Significant heat conduction from the rings (caused from previous runs) was sensed by the thermistors only after a long time had elapsed. This was a desirable behavior because drift control potentials gradually decreased throughout the day. This procedure nearly always permitted runs to be made continuously without loss of calorimeter control which would require reheating and agitation to regain control, with consequent delay. Up to 45 runs were made in a 7 hour period, including the time required to get the calorimeter into operation. Runs were made on approximately 40 days. The standard deviation for a daily set of measurements varied from 0.3-1.1 percent, with a mean value of 0.6 percent.

## 10. Thermistor Power Levels

The stability of the traces shown in figures 10 and 11 is remarkable when considering the small temperature increments represented by the noise levels shown, compared to that caused by the power levels  $P_C$  and  $P_J$ . Studies with different power levels proved valuable in

correcting for the effects of small changes in power during irradiation and in improving the operation of the calorimeter.

In figure 12, the bottom horizontal line (a) represents the equilibrium temperature of the thermistors and water when  $P = 0$ . The horizontal line (b) represents a 24 mK average temperature rise in each thermistor

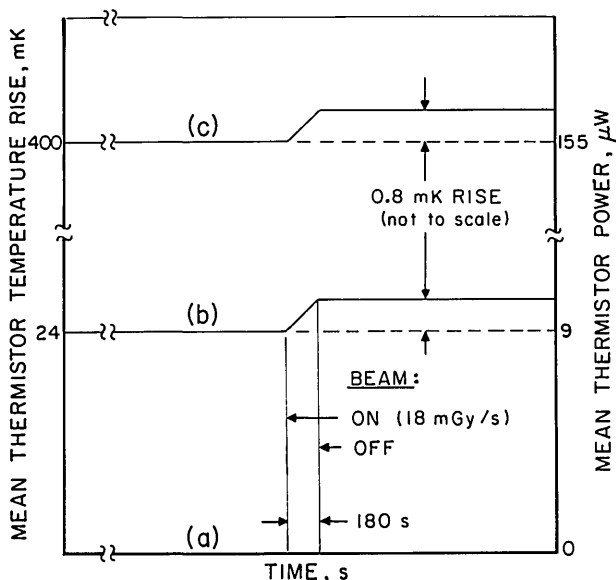


FIGURE 12. Rise of thermistor temperature levels as a result of electrical power dissipations and beam irradiation.

when  $P = 9 \mu\text{W}$  in each ( $P_C$  and  $P_J$  actually differed by 1-7 percent, depending on initial balancing conditions). The figure shows a further temperature rise of 0.8 mK (3.3 percent) as a result of an absorbed dose rate of 1.1 Gy/min for three minutes (the predominant irradiation condition used in this investigation). The horizontal line (c) represents a 400 mK temperature rise when  $P = 155 \mu\text{W}$ , and irradiation further increased the temperature rise by 0.8 mK (0.2 percent).

The thermistor temperature rises caused by irradiation were, therefore, very small compared to those caused by electrical power dissipation. This raises an important question as to the power level that would result in optimum performance. Initial investigations were performed at the 155  $\mu\text{W}$  level, and then at the 9  $\mu\text{W}$  level, which permitted a factor of three increase in amplifier gain. The precision of measurements remained unchanged, about 0.6 percent standard deviation for a daily set of measurements. Measurements over periods of months indicated that operation at the lower power level produced the most stable ratio of output to spurious signal.

During irradiation the thermistor resistances decreased while the bridge balancing resistor ( $R$  in figure 7) was manually decreased in value to maintain the output signal near the zero null position. Calculations were made to determine the changes in  $P_C$  and  $P_J$  and the resultant temperature changes by use of eq (8). Although these changes produced negligible fractional changes in the (b) and (c) levels (of figure 12), the temperature changes represented much larger fractional changes when they were compared to the 0.8 mK temperature rise caused by the irradiation. The effects are shown in table 2. Column 1 lists the nominal power levels in microwatts. Columns 2 and 3 list the changes in  $P_C$  and  $P_J$  in picowatts. The changes in average powers are shown in column 4. The negative sign indicates that the (b) level decreased, reducing the measured fractional resistance change that required a correction of 0.04 percent increase at the 9  $\mu\text{W}$  level and a 1.5 percent decrease at the 155  $\mu\text{W}$  level. These corrections were calculated from a detailed analysis of the currents and resistances in the Wheatstone bridge circuit before and after the irradiation. They are a good indication of how

TABLE 2: Thermistor electrical power changes and corrections caused from an absorption of 3.3 Gy.

Nominal thermistor power ( $\mu\text{W}$ )	Change in $P_C$ (pw)	Change in $P_J$ (pW)	Change in average power (pW)	Correction (%)
9	120	-360	-120	0.04
155	8100	50	4100	-1.5

closely the simplified formula (1) describes the real situation, where the power levels change.

Even after applying the above corrections, it was found that the absorbed dose measurements were affected by the power level. This is shown in figure 13. The reason for this behavior is not understood, although recommendations for its possible reduction or elimination will be discussed later. It is speculated that the effect may have been caused by increased thermal coupling between the thermistors and wires with their surroundings during irradiation. This presumably would cause the higher (c) level to drop more than the lower (b) level, and they may not have fully recovered to their initial positions after irradiation to enable an accurate measurement to be made.

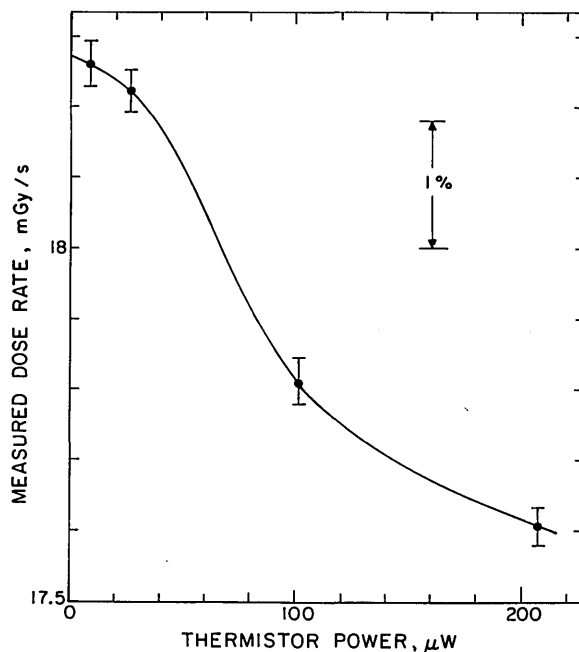


FIGURE 13. Variation of the measured absorbed dose rate versus thermistor electrical power dissipation.

An example of the rate of equilibrium temperature buildup around the thermistors is shown in figure 14. This is the recorder-pen response when the thermistors were subject to a sudden change in power, by suddenly changing  $R_1$ . The response was primarily a temperature effect when compared to a much faster response when only the balancing resistance ( $R$ ) was changed. About 90 percent of the temperature change occurred in 2 s, but thereafter the rate of temperature change rapidly diminished. If something similar to this were happening after beam turn-off, it was assumed that this effect (or any other) would disappear for  $P = 0$ . Corrections to this condition were made for all measurements reported in this paper.

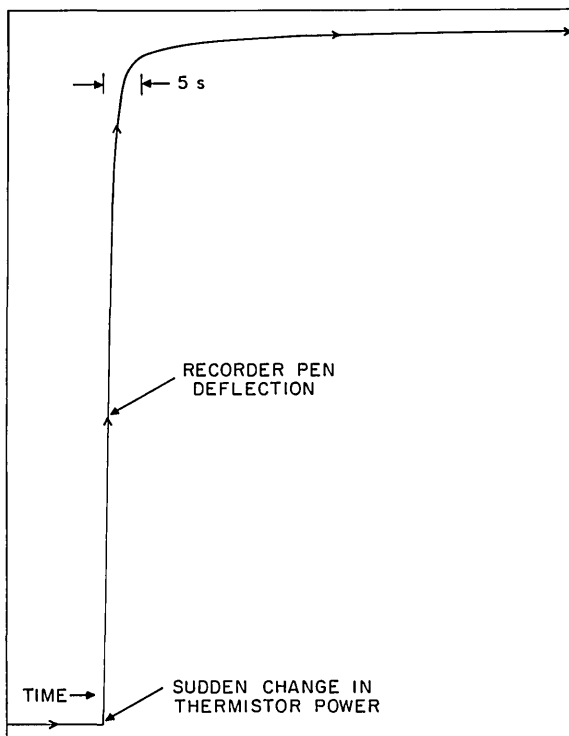


FIGURE 14. Recorder-pen response showing the rate of relative change in temperature of the thermistors when subject to a sudden change in electrical power dissipation.

## 11. Tests in the C, J, and C + J Modes

The results listed in table 3 show the consistency of the absorbed dose measurements with either thermistor or with both in the bridge circuit. The measurement tests were made in distilled water on three separate days; the water was discarded at the end of each day. The source-to-detector distance was 82 cm, the detector depth was 5 cm, and the cobalt-60 beam was broad. On the first day the thermistor powers were  $9 \mu\text{W}$ . The first entry in the first row indicates the C + J mode (the two-thermistor bridge), while the second and third entries in that row indicate the electrical power dissipations in the thermistors. The second row indicates the one-thermistor J mode. Although the C thermistor was switched out of the bridge, an auxiliary power supply maintained its  $9 \mu\text{W}$  dissipation. The third row still indicates the J mode, but with  $P_C = 0$ . On the second day, measurements were made at  $158 \mu\text{W}$  power levels. On the third day, the power level ( $P_J$ ) of the measuring thermistor was  $9 \mu\text{W}$ .  $P_C$  was zero or  $160 \mu\text{W}$ , the latter causing the C thermistor temperature rise to increase by an additional 26 percent. The fourth column lists the absorbed dose rate measurements that include 0.07 and 3.4 percent correction factors (i.e., corrected to  $P = 0$  conditions, using the curve shown in figure 13) when the power levels in the

measuring thermistors were 9 and  $160 \mu\text{W}$ , respectively. Inspection of the results in the fourth and fifth columns indicates the consistency and repeatability in any measurement mode on each of the three days. Therefore, large changes in temperature gradients around the thermistors did not affect the results. These tests also indicated the sharpness of the equilibrium temperature gradients around the thermistors separated by 2.5 mm. A change of temperature rise in either thermistor caused a temperature rise change in the other of only 1.5 percent, as determined by the re-balance of the Wheatstone bridge circuit.

Column 6 shows the number of 2-min irradiation runs. Column 7 shows the total time to complete those runs under the conditions of the nominally applied potential and current ranges shown in columns 8 and 9, respectively. The data in columns 4 and 9 indicate that the measurements were not affected by electrical current through the water.

## 12. Tests for Water Convection

Results of three observations indicated no evidence of water convection during measurements in the calorimeter described.

In the case of cobalt-60 irradiation (directed vertically downward), the temperature decreases with depth, except from the surface to about 0.5 cm. Consequently, for this radiation source there are, in principle, essentially no buoyant forces trying to cause convection at depths larger than 0.5 cm. However, even in the absence of any irradiation-produced temperature gradients, there is a natural concern as to whether non-uniformity of water temperature in the large 30 cm cube of water can be such as to set convection in motion. Furthermore, the largest temperature gradients were those caused by electrical power dissipation in the critical regions around the thermistors. Therefore, the possible existence of variations in convective forces at different distances from the thermistors had to be investigated.

The sandwiching polyethylene films themselves form a convective barrier that will delay the onset of convection, or slow it down, compared to isolated point detectors without the films. Such a point detector was also used in the first test for convection.

Figure 15 shows a square (152 mm inside) polystyrene frame (5 mm thick) supporting two  $254 \mu\text{m}$  diameter copper wires separated by 25 mm. The wires had about  $40 \mu\text{m}$  thick uniform coatings of commercially applied varnish that provided high electrical resistance ( $>10^{13} \Omega$ ) from water over long periods of time. Figure 16 shows a close-up view of the wires and thermistors near the frame center. The construction was relatively difficult and fragile, and not as effectively insulated over long

TABLE 3. Absorbed dose measurement test results in the C, J, and C + J modes.

Mode of operation	Thermistor power		Dose rate (mGy/s)	Mean error of the mean (%)	Number of runs	Total time (min)	Potential range (V)	Current range (mA)
	C ( $\mu$ W)	J ( $\mu$ W)						
C + J	9	9	24.93	0.1	9	40	0-0	0-0
J	9	9	24.83	.1	6	25	0-0	0-0
J	0	9	25.02	.4	6	25	0-0	0-0
			24.93					
			$\pm 0.2\%$					
Water agitated for 8 min, temperature raised								
C + J	9	9	24.97	0.2	10	55	10-35	0.5-2
C	9	9	24.87	.3	6	35	30-20	1.5-1
C	9	0	25.08	.4	7	35	10-5	0.5-0.2
C + J	9	9	24.98	.2	7	30	0-0	0-0
			24.95					
			$\pm 0.3\%$					
C + J	158	158	24.95	0.7	10	85	35-15	2-1
J	158	158	24.90	.7	7	30	0-0	0-0
J	0	158	24.97	.4	6	32	0-0	0-0
			24.93					
			$\pm 0.6\%$					
J	160	9	24.80	0.2	10	55	25-50	1.5-3
J	0	9	24.90	.2	10	55	50-35	2.5-2
J	160	9	24.98	.2	10	40	0-0	0-0
			24.90					
			$\pm 0.2\%$					

periods of time as with use of the films; nevertheless, the detector was sufficiently good for its intended purpose. Care had to be used in passing this detector through the water surface so that the surface tension would not damage the delicate structure.

The large wires are shown twisted together after having been cut. On each side of the two twisted junctions, small varnish sections (separated by about 2.5 mm) were scraped away with a surgical blade to permit attachments of the Pt-Ir wires fused to the two 0.25 mm diameter bead thermistors. Soldering the wires caused melting of the varnish, but the electrical resistance across each twisted junction remained high (about  $5 \times 10^{13} \Omega$ ). High electrical resistance was needed because the thermistors were to be positioned in opposite arms of the Wheatstone bridge circuit.

The bare 25  $\mu$ m diameter Pt-Ir wires and the seemingly porous thermistor beads were covered with several coatings of silicone rubber to electrically insulate them from water. The final variable coating thicknesses were about 0.05-0.13 mm on the bare wires, and about 0.13

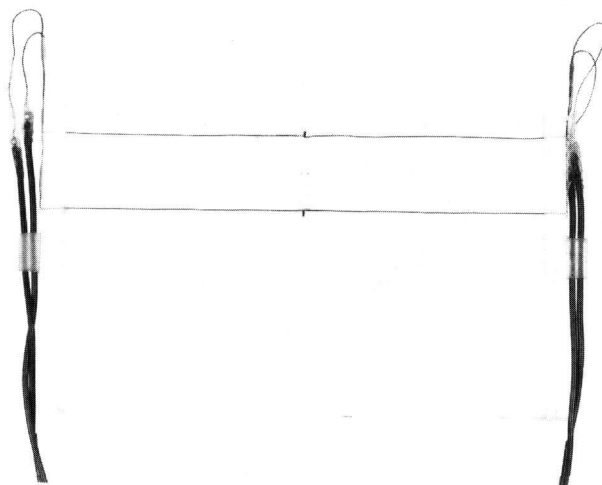


FIGURE 15. Photograph showing mounting of two thermistors with insulative leads.

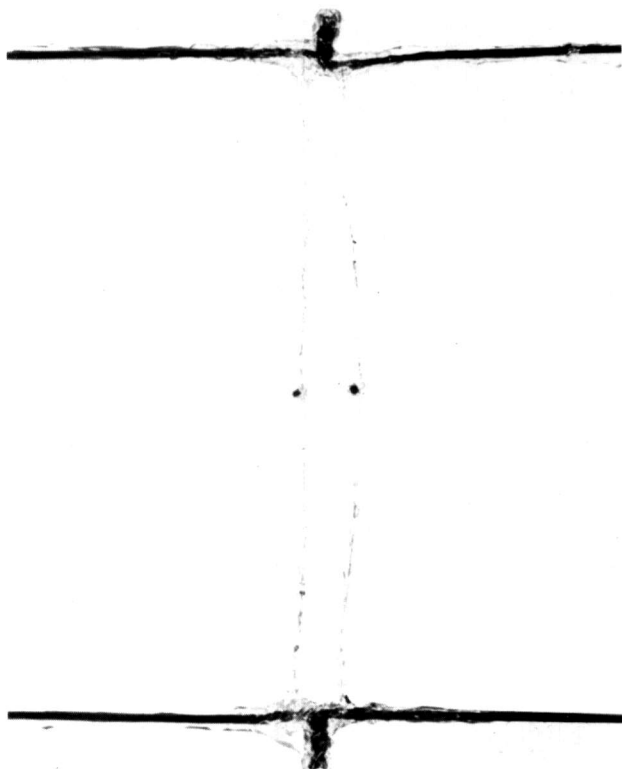


FIGURE 16. Close-up photograph of the two insulated 0.25 mm diameter bead thermistors and leads.

mm around the beads. Compared to the uniformly thin polyethylene film insulators (which were much better), large uneven coating thicknesses could produce larger excess generated heat during irradiation that would be difficult to account for by calculation.

These thermistors ( $C'$  and  $J'$ ) were horizontally positioned at a depth of 6 cm in distilled water and were separated by 1.5 mm at the time of the measurements. Measurements were made in this condition and also by placing a stretched  $2\ \mu\text{m}$  plastic film above the thermistors at a distance of 2.5 mm and then at 8.7 mm. The film was mounted on a polystyrene frame similar to that shown in figure 15. This convective barrier would presumably have had an effect on any convection that existed.

There were two modes of operation. In the  $C' + J'$  mode, the two thermistors were located in opposite arms of a bridge circuit. Plots were made of the measured resistances,  $r_{C'}$  and  $r_{J'}$ , as a function of their electrical power dissipations,  $P_{C'}$  and  $P_{J'}$ .  $P_{C'}$  varied from 8-530  $\mu\text{W}$ , while  $P_{J'}$  varied from 12-720  $\mu\text{W}$ , which produced maximum thermistor temperature rises of 0.8 and 1.5 K, respectively. Measurements were also made in the  $C'$ -mode where  $P_{J'}$  was zero, while  $P_{C'}$  was again varied from 8-530  $\mu\text{W}$ .

If a large onset of convective motion had occurred, then it could be expected that an abrupt change in the resistance versus power curves (such as in fig. 9) would have been observed. An onset of convection would have had a sudden cooling effect on the thermistors that would have caused the curves to have an abrupt upward curvature. No significant change in slope was observed.

However, there may have been minute convective currents confined to the immediate vicinity of the thermistors where there were sharp temperature gradients. In principle, such highly confined convection has essentially little or no effect on the measurements of resistance or absorbed dose.

The second test was mainly to detect if there was any existing motion of the water that affected the measurements. The structure used is shown in figure 17. The detector was the one first described, the two thermistors sandwiched between films.  $P_C$  and  $P_J$  were 9  $\mu\text{W}$ , which produced temperature rises of only 24 mK. The front and rear distances of the barriers from the plane of the thermistors (at a 5 cm depth) were 17 and 22 mm, respectively. Each barrier consisted of a  $2\ \mu\text{m}$  thick plastic film stretched on a polystyrene ring, 15 cm inside diameter. Three plastic rods spaced each barrier parallel to the detector plane. The rods permitted flow of water between the planes during agitation. They also permitted the drift control electrical current to pass freely between those planes. Measurements of absorbed dose rates (on the same day) were made with and without the convection barriers in position. The results are shown in table 4.

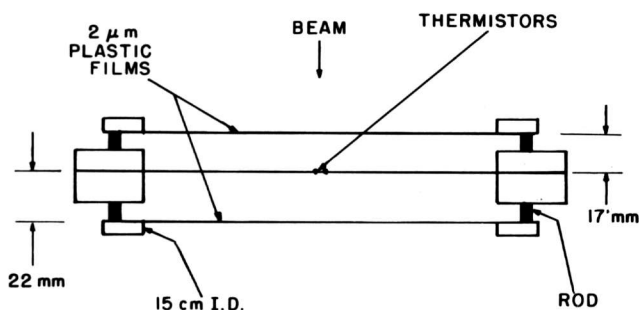


FIGURE 17. Configuration of the detector and  $2\ \mu\text{m}$  plastic film convection barriers.

TABLE 4. Results of second water convection test.

Convection barriers	Dose rate (mGy/s)	Difference (%)	Mean error (%)	Number of runs
In	18.39	0.20	0.18	12
Out	18.43		0.16	12

Placement of the barriers in position would have decreased any existing water convection at those positions. Because there was no significant difference in the dose rate measurements, it was concluded from this test that convection in the vicinity of those barriers was insignificant or non-existent.

The third and most sensitive and convincing test, which at least indicates the absence of moderate water convection, is the recorder-pen tracings shown in figures 10 and 11. The indicated average temperature rises of the thermistors above that of the water are 413 and 25 mK, respectively. Compared to the noise levels of only several microdegrees, these gave differential temperature ratios of roughly 100,000 to one and 10,000 to one in figures 10 and 11, respectively. These large ratios and the existence of the sharp temperature gradients around the thermistors would seem to have created a sensitive condition for detecting turbulent motion. Large changes would have disturbed the temperature gradients which would have caused large disturbances in the recorder output. Instead, long and stable drifts were observed. From these observations, it was concluded that the sharp temperature gradients around the thermistors produced insignificant or non-existent local turbulence and that these conditions extended to much larger distances.

It is worth repeating that on a few occasions the tracings did show sudden changes which were believed to have been caused by sudden changes in air circulation which produced air pressure changes in the measurement room. However, it was only on one out of 40 measurement days that the stability was considered impaired enough (only during the large thermistor power dissipation of  $155 \mu\text{W}$ ) so that the measurements made on that day were ignored. Possible ways to eliminate the air pressure effect will be suggested later in this paper.

### 13. Effects of $\text{N}_2$ and $\text{O}_2$ Saturated Water

It is well-known theoretically that irradiation of water saturated with oxygen induces production of hydrogen peroxide [25,26]. If oxygen were the only gas *initially* present in the water, then it would aid in producing a positive heat defect which means that it would contribute to a decrease in calorimeter response. It is also theoretically expected that the heat defect would be less significant for the case of water *initially* saturated with nitrogen, replacing the oxygen. An experimental test was made to determine whether a significant difference in the measured absorbed dose rate could be detected. The results are shown in table 5.

A set of measurements was made on three different days. Each morning the calorimeter was refilled with newly drawn once-distilled water. Column 1 indicates

the gas used to agitate the water. The gas flow rate near the four vertical edges in the water in the tank was about 1.5 L/min. Column 2 indicates the duration of agitation. Column 3 shows the measured absorbed dose rates (corrected for cobalt-60 decay), and column 4 shows the differences in measured results. The percent mean errors of the mean and the number of runs are shown in columns 5 and 6, respectively. Column 7 indicates the continued rate of gas flow (after agitation) in the space between the two calorimeter enclosures to prevent air from diffusing back onto the water surface during measurements. The duration of each run was three minutes.

The results show that (for the conditions described) there was no significant difference in measurements of absorbed dose rate as a result of the water pre-agitated with oxygen or nitrogen. However, it is not concluded that an effect caused by hydrogen peroxide production did not exist. It was subsequently pointed out [27] that if the water still contained *initial* concentrations about  $10^{-6}$  mol/L (or larger) of dissolved *hydrogen* and *oxygen*, then a 3.0 percent reproducible exothermic reaction (increase in heat) would have been included in the measurements. The nitrogen used to pre-agitate the water was classified: "High purity, oxygen-free, < 5 ppm."

More experimentation is necessary. New apparatus would have to be constructed for use of triply distilled water saturated separately with oxygen, nitrogen, or hydrogen. Water saturated with hydrogen is believed to have a virtually zero heat defect [28].

### 14. Effects of Water Impurities

Important critical questions concerning the effects of water impurities and calorimetric materials must be investigated. Once-distilled water was used for beam calibration measurements. It was inexpensive and readily available in large quantities, which were important practical considerations. However, was the water from the still pure enough so that radiation induced chemical effects were negligible? Also, what are the effects of dissolved organics from the immersed calorimetric materials? The calorimeter was used to answer these complex questions as much as possible.

Figure 18 and table 6 show results of investigations with liquids of widely different impurities. Column 1 identifies the liquid and column 2 identifies the curves shown in the figure. Column 3 indicates the gas used to agitate the water prior to the start of measurements. Figure 18 shows curves of the "apparent" absorbed dose rate (absorbed dose plus chemically induced effects) as a function of the accumulated calorimetric response up to 150 Gy. In reality, all absorbed dose measurements reported in this paper were determined from

TABLE 5. Results with  $N_2$  and  $O_2$  saturated water.

Gas	Duration of agitation (min)	Dose rate (mGy/s)	Difference (%)	Mean error (%)	No. of runs	Gas over-flow rate (cm <sup>3</sup> /min)
$N_2$	17	18.40	-0.3	0.18	8	30
$O_2$	22	18.34				
$N_2$	33	18.39	-0.05	0.11	12	70
$O_2$	33	18.38				
$N_2$	67	18.31	0.2	0.09	16	120
$O_2$	67	18.34				

TABLE 6. Liquid parameters and results.

Liquid	Curve	Agitation gas	Electrical resistivity	
			(k $\Omega$ -cm)	Approx. max. daily change (%)
Distilled water	1	$O_2$ - $N_2$	100-800	-100
Tap water	2	$N_2$	4	30
$10^{-2}$ M/L iso-propyl alcohol	3	Air - $N_2$	200-600	-100
$10^{-5}$ M/L cadmium sulfate	4	Air	100	-80
" " "	1	$N_2$	100	-70
$10^{-3}$ M/L sodium formate	5 - 5'	$N_2$ - $O_2$	200	-40
" " "	6 - 6'	$O_2$ - $N_2$	300	-60

measurements of heat rise that resulted from all irradiation effects. For all results shown in figure 18, the source-to-detector distance was 1 m, the detector depth in water was 5.0 cm, the cobalt-60 beam was broad, and the irradiation times were 3 min, resulting in an absorbed dose of 3.3 Gy in distilled water (the points are not shown for the sake of clarity). Also, in all cases the liquid was discarded at the end of a day of measurements. Then (except after using distilled water) the drift control immersion plates were removed, thoroughly cleaned, and the tank was refilled twice—agitated, and drained during agitation.

Curve (1) in figure 18 indicates that for distilled water there was no detectable change in measurements.<sup>12</sup> Column 4 of table 6 indicates a large variation in the water

electrical resistivity ( $\rho$ ), 100-800 k $\Omega$ -cm. Column 5 indicates that the value of  $\rho$  decreased by approximately 100 percent during measurements throughout the day. That irradiation is not the cause is evident from figure 19 where measurements of  $\rho$  were made as a function of time in the absence of and then with irradiation on a new supply of distilled water. With 23 V across the electrodes, the initial and final current and power ranges were 4.0-4.7 mA and 90-110 mW, respectively.

Curve (2) in figure 18 shows results of repeatable measurements with tap water on two separate days. The initial calorimeter response was 35 percent higher than with distilled water, but rapidly decreased to within 1 percent of distilled water between 60 and 150 Gy. The water was noticeably discolored (muddy in appearance as a result of pipe supply maintenance). The formation of many bubbles on the immersed surfaces indicated that the tap water was very gassy (bubble formation was not evident with distilled water). The initial value of  $\rho$  was 4 k $\Omega$ -cm, lower than the average for distilled water by ap-

<sup>12</sup>Examination of all data, however, roughly suggests that there may have been a small increase below 10 Gy. Several attempts were made to further explore this region by decreasing the duration of the runs from three minutes to one minute, to get better resolution of measurements. The results were inconclusive.

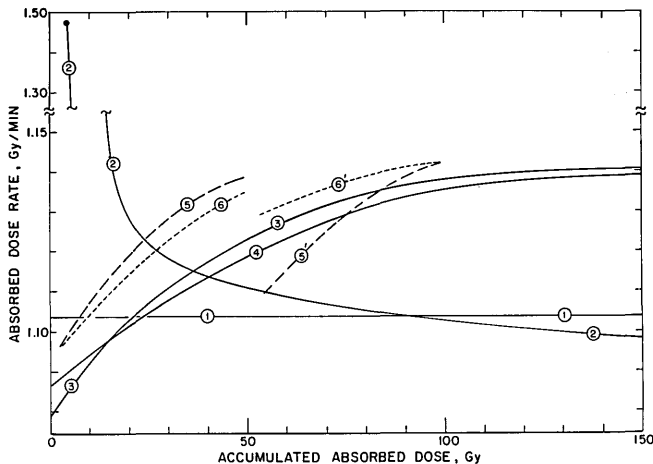


FIGURE 18. Measured dose-rate as a function of accumulated dose, for: (1): distilled water, or cadmium sulfate solution  $N_2$  saturated; (2): tap water; (3): iso-propyl alcohol solution  $N_2$  or air saturated; (4): cadmium sulfate solution air saturated; (5)-(5)': sodium formate solution  $N_2$ - $O_2$  saturated; (6)-(6)': sodium formate solution  $O_2$ - $N_2$  saturated.

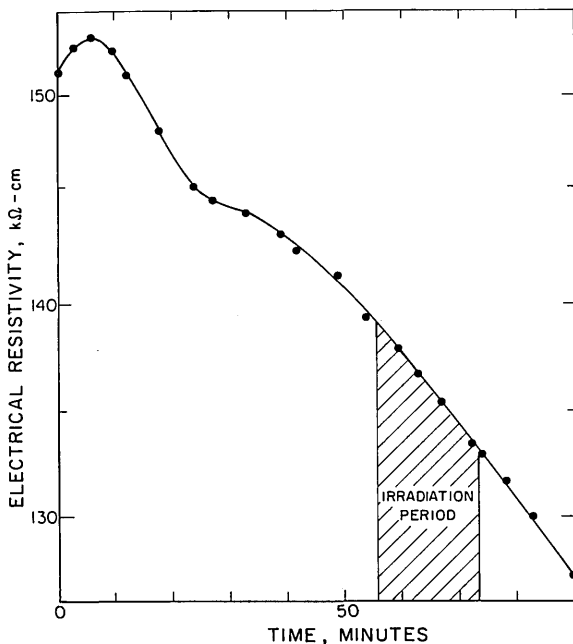


FIGURE 19. Change in water electrical resistivity in the absence of and during irradiation.

proximately a factor of 100. The value of  $\rho$  increased by approximately 30 percent during the measurements. To efficiently control the drifts in water with such a low resistivity, the electrical components in the temperature drift controller (figure 3) had to be replaced.

Curve (3) of figure 18 shows results of complicated reactions [25,26] due to irradiation of a solution of  $10^{-2}$  mol/L of iso-propyl alcohol. On one day air was used to agitate the liquid, and on another day the high purity

nitrogen was used. The results showed no significant difference between the measurements. Initially, a heat deficiency (relative to the distilled water) was observed, but it diminished and then a heat excess gradually increased to 3.4 percent at 150 Gy.

Curve (4) shows similar results of one day of measurements using a radical scavenger [25] solution of  $10^{-5}$  mol/L of cadmium sulfate added to the distilled water preagitated with air. However, when nitrogen was used on another day, the results were the same as with distilled water, table 6.

Curves (5) and (5') show results with a  $10^{-3}$  mol/L sodium formate solution preagitated with nitrogen and oxygen, respectively. The reaction of the solution with irradiation results in the formation of hydrogen peroxide. Initially, a small positive heat defect was observed, but it disappeared near 10 Gy where a negative heat defect grew to an extrapolated value near 4 percent at 150 Gy. Curves (6) and (6') show results on another day when the agitation was with oxygen and nitrogen, respectively.

Further studies were carried out to determine the effect of storing distilled water in various containers. The water supply was drawn from a 100 L stainless-steel reservoir. During the course of the measurement, it was noticed that the bottom of the reservoir was covered with a hard layer of residue. The reservoir was removed, thoroughly scrubbed with steel and nylon brushes, and rinsed numerous times with distilled water. Although the value of  $\rho$  increased by a factor of eight, no noticeable difference was observed in the measured absorbed dose rate. Occasionally, the water in the reservoir was agitated while it was being completely drained and then refilled.

The water drawn from this reservoir was stored in three types of containers prior to use in the calorimeter. Container #1 was a new 25 L polyethylene jug. The water used from this jug was always replaced in that jug. Measurements in this water extended over a period of seven months—a period long enough for organic materials from the polyethylene to dissolve into the water. Container #2 was a 25 L used glass jug. Numerous rinses with solvents and solutions of sodium hydroxide, sodium dichromate and sulfuric acid, followed by numerous rinses with distilled water, failed to remove noticeable internal deposits of unknown composition. Nevertheless, use of this jug was considered of value in view of the objective of the investigation. Water stored in this jug was also replaced in that jug after use in the calorimeter tank. Container #3 was a new 25 L glass jug that was washed with hot solutions of detergent soap and rinsed numerous times with hot tap water and then numerous times with distilled water. Water stored in this container was always discarded after it was used in the calorimeter tank. Only the results of measurements in

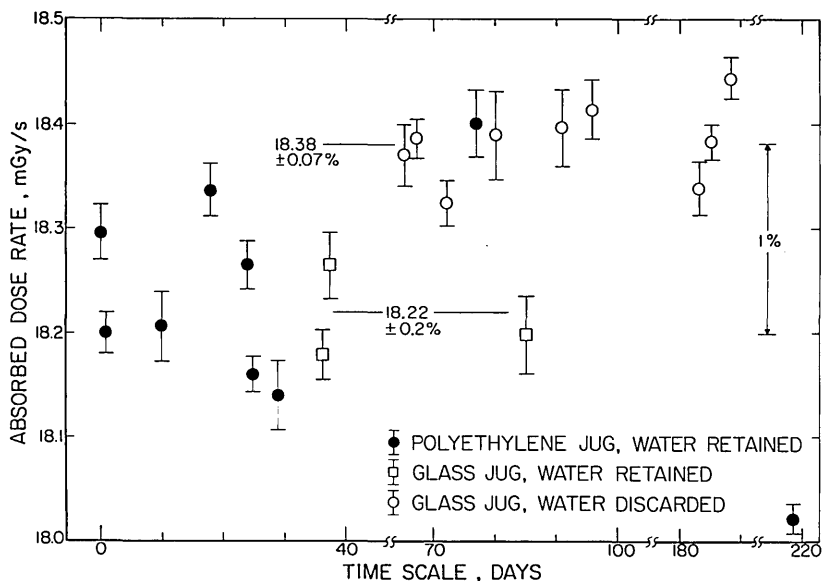


FIGURE 20. Comparison of broad-beam absorbed dose measurements in water stored for different durations in three different containers.

water from this container (#3) were used for the final reported beam calibrations.

The results for broad beam irradiation are shown in figure 20, where the absorbed dose rate (corrected for cobalt-60 decay) is plotted as a function of time. The uncertainties are mean errors of the mean. The data shown by the closed circles were from measurements in water from container #1. The water was pre-agitated with air prior to the measurement results shown by the data points from 0-29 days, whereas nitrogen was used prior to the measurement results made on the 77th and 219th day. The mean value of those nine data groups was 18.23 mGy/s, with a mean error of 0.2 percent. Measurement results in water from container #2 (shown by the squares) were made on the 36th and 37th day (water pre-agitated with air), and also on the 85th day (water pre-agitated with nitrogen). The mean value of the three data groups was 18.21 mGy/s, with a mean error of 0.2 percent. The results show no significant difference between the two sets of data that have a mean value of  $18.22 \pm 0.2$  percent for the 12 data groups. The nine data groups shown by the open circles extending from the 65th to 186th day (water pre-agitated with nitrogen) are from measurements in water from container #3. The range of the data points in this group is 0.7 percent, which indicates good reproducibility of results over a period of 121 days. The mean value of those nine data groups was 18.38 mGy/s, with a mean error of 0.07 percent. The results indicate that the measurements were not critically dependent on the cleanliness or material of the storage containers. The

constancy of successive runs throughout a day indicated a negligible effect of dissolved organics from the sand-wiching films into the immediate surrounding water.

## 15. Results for Collimated Beam

The mean value of nine sets of determinations on nine different days was 17.21 mGy/s, with a standard error of the mean of 0.07 percent. The final result was 17.21 mGy/s  $\pm 0.4$  percent combined uncertainty. The conditions of the measurements (corrected for cobalt-60 decay) were for the once distilled water pre-agitated with high purity nitrogen (oxygen free, < 5 ppm), detector depth at 5 g/cm<sup>2</sup>, source-to-detector distance of 1 m, and for the collimator size that produced the beam profile shown in figure 1. These were the same conditions that were used to calibrate the same beam with the graphite calorimeter [8]. Conversion of those results to water [9] gave an absorbed dose rate of 16.63 mGy/s  $\pm 0.6$  percent combined uncertainty. The result with the water calorimeter is 3.5 percent higher than this value.

The higher apparent absorbed dose rate in once distilled water appears to be in approximate agreement with a recent result. Measurements in double distilled and in de-ionized water (in a copy of the calorimeter described in this paper) were 3.8 percent higher when the measurements were compared with those determined with an ionization chamber [29]. This same general conclusion also appears to be the case for comparison for measurements in a small cell alternately containing double distilled water and a Fricke solution [30].

## 16. Corrections and Uncertainties

A negligible uncertainty was assigned to the specific heat of water that has listed values (versus temperature) to five figures in reference [7]. Corrections and uncertainties in measurement of source-detector distance and the 5 cm *linear* depth in water were negligible because of the accuracy of the optical sighting and micrometer measurements. However, a 0.05 percent correction was required to correct all absorbed dose measurements to a mass depth of 5 g/cm<sup>2</sup>. Uncertainties in the calibrated temperature probe (1 mK temperature resolution display) needed to measure the sensitivities of the thermistors were considered to be negligible.

Table 7 lists larger uncertainties from sources shown in column 1. The second column lists statistical uncertainties  $s_i$  in terms of standard deviations of random measurements, and the numbers in parentheses are the corresponding numbers of degrees of freedom. The largest statistical uncertainty is 0.2 percent for the reproductibility of measurements in new supplies of distilled water. The uncertainty in determining the sensitivity of either the *C* or the *J* thermistor is listed as 0.1 percent. Ionization measurements in a water phantom showed that the expanded polystyrene and aluminum foil of the calorimeter lid decreased the absorbed dose measurements by 0.34 percent. This correction was made and a 0.05 percent uncertainty was assigned.

TABLE 7. *Uncertainties in the absorbed dose rate measurements.*

Source	Estimated uncertainty (%)	
	Statistical (degrees of freedom) $s_i (\nu_i)$	Other $u_j$
Reproducibility of water	0.2 (8)	
Sensitivity of C-thermistor	0.1 (3)	0.1
Sensitivity of J-thermistor	0.1 (3)	0.1
Effect of lead resistances		0.05
Beam attenuation of calorimeter lid	0.05 (5)	
Beam exposure timing		0.05
Extrapolation to zero thermistor power		0.3
Polyethylene films		0.05

$$\text{Combined uncertainty} = \sqrt{\sum s_i^2 + \sum u_j^2} = 0.4\%$$

Column 3 lists the uncertainties  $\mu_j$ , which are believed to be reasonable estimates of other non-statistical uncertainties, to be treated as if random in character. A 0.1 percent uncertainty was assigned for this type of uncertainty in determining the sensitivity of either the *C* or the *J* thermistor. The *Pt-Ir* leads fused to each thermistor bead had a calculated resistance of 9.5 ohms, and the additional copper signal leads raised the resistance to 10.7 ohms external to the nominal 3 k $\Omega$  resistance within the beads. These external resistances decreased the fractional change in resistance of each thermistor arm which caused a decrease in the fractional measured change in the bridge-balancing resistor arm. An analysis showed that the results of the measurements had to be increased by 0.36 percent, and a 0.05 percent uncertainty was assigned. A 0.05 percent uncertainty was also assigned to the beam exposure time and to the thermal effects of the polyethylene films. A 0.3 percent uncertainty was assigned for extrapolation to zero thermistor power (from fig. 13).

These initial measurements gave no conclusive evidence for assigning corrections or uncertainties for heat defects for the experimental conditions described.

The *combined uncertainty* was calculated by using a recently recommended procedure [31]. That uncertainty was obtained by combining in quadrature the uncertainties shown in table 7. The combined uncertainty was calculated to be 0.4 percent, excluding effects of the radiation chemistry of water. Treating the combined uncertainty as if it were a mean error, it can be multiplied by a factor of 2 to obtain an *overall uncertainty* of 0.8 percent. For the present, this overall uncertainty is rounded upward, and an uncertainty of about 1 percent is assigned to absorbed dose determinations with the water calorimeter in the NBS cobalt-60 gamma-ray beam, excluding uncertainty arising from radiation chemistry of water.

## 17. Discussion

An interesting result is that the absorbed dose rate measured in water was 3.5 percent higher than the results converted from measurements with a graphite calorimeter. The sources of this significant difference cannot at present be explained with assurance. The theoretical 3.0 percent exothermic effect, that could have been produced by production of hydrogen peroxide, offers the best lead to explain most of the difference. This will be explored experimentally and theoretically. Also, there still remains an unresolved problem in calorimetry concerning the effects of vacuum gaps in calorimeters made of solid materials. Recent experimental data for 12-30 MeV electrons indicate that the gap effects, in a copy of the NBS graphite calorimeter, vary in the range

of  $\pm 0.7$  percent, depending on the beam energy [32]. Speculative reasoning would seem to indicate that the gaps surrounding the core would result in a smaller response than the water calorimeter that has no such gaps. This would provide a partial explanation of the difference. Further experimental data, that will include results under different irradiation conditions, will be available from use of replicas of calorimeters that are now in operation or are being constructed at other institutions. Also in progress by others are theoretical calculations concerning effects in water under different irradiation conditions.

## 18. Recommendations

Previous speculation (in reference to fig. 13) pointed out that the dependence of the measured absorbed dose rate on the thermistor electrical power dissipation may have been caused by increased thermal coupling (during irradiation) between the thermistors, leads and connecting wires with their surroundings. The *c*-level (fig. 12) would then have dropped more than the *b*-level, and they may not have fully recovered in time after irradiation when extrapolations were made. The magnitude of this effect may be inherent in the exact thermal coupling in a particular detector. Regardless as to whether this was the cause, it would seem good constructional practice to have those temperature levels as low as possible for given thermistor power dissipations. The detector could be fabricated to increase the thermal coupling which may greatly attenuate the effect shown in figures 12 and 13. A portion of the leads and connecting wires was surrounded by air which has a lower thermal conductivity by a factor up to 20 compared to some adhesive materials. However, extreme caution must be used in applying such materials (preferably flexible). Those non-water materials must be extremely thin. The calculated effect of the two 18  $\mu\text{m}$  films (fig. 6) should serve as a guide for the caution that must be used.<sup>13</sup> It was also pointed out (Section 4) that theoretical calculations showed negligible effects caused by the beads and wires. Therefore, minute amounts of adhesive judiciously placed can still result in tolerably small excess heat generation. The material should also be of a slow-drying

<sup>13</sup>Being unaware of this need for caution was the reason for applying excessive silicone rubber to those elements in the first reported model of the water calorimeter [1] which was quickly assembled and beam tested within a month after conception of the idea of the instrument (the calculations were made a considerable time later). It was speculated in that report that the cooling effect after beam turn off (in figure 2 of that report) may have been caused by water convection. However, in the light of subsequent experimental work reported in this paper, that effect is believed to have been caused by heat conduction—excess heat conducted away that was caused by the excessive non-water adhesive material.

nature. Using a thin wire (or other suitable applicator), very small droplets of the adhesive could be applied in the regions of the greatest heat concentrations, on the top of the beads and along the Pt-Ir leads (and possibly on the lower film in their immediate vicinity). Per unit length, the ratio of thermal conductivities of the copper and Pt-Ir wires used was 120/1. After fastening the rings, air at constant pressure (or other mechanical means) should be applied to both sides of the films for a sufficient time to give good adherence and a minimal adhesive thickness between the beads, wires, and films. It would then be reasonable to expect that such a construction would also aid in making such a detector less sensitive to effects of changes in room barometric pressure as previously described and shown in figure 10. It is worth repeating that the magnitude of that pressure effect became less noticeable as electrical power dissipations decreased. It was not noticeable at the 9  $\mu\text{W}$  level at which all the beam calibration measurements were made.

The cobalt-60 measurements reported in this paper were within a 150-Gy accumulated absorbed dose at the point of measurement. Further investigations should be made at extended ranges including pre-irradiation of water beyond the kGy region. Similar investigations should be carried out with other irradiation beams and a wide range of absorbed dose rates.

Although the data indicate that organic materials dissolved into the water from the plastic container do not seem to be a problem, it would still be good practice to minimize the amount of immersed plastic materials. Consideration should be given to constructing a container with its bottom and two opposite sides consisting of glass plates, and the other two sides consisting of stainless steel plates. The metal plates would serve a dual role as being the drift control electrodes containing drilled holes, beneath the water surface, through which the immersion heaters and signal feedthroughs would be mounted. The immersed tube, through which air is forced to agitate the water, should be glass.

## 19. Summary

Experience with the water calorimeter has proven that it can be placed into operation quickly. In this respect, it represents a considerable improvement over solid calorimeters requiring vacuum systems. The predominant goal of the NBS work in absorbed dose calorimetry was to develop means to quickly control or eliminate one of the most troublesome features of calorimeters that prevented their wider adoption as a practical laboratory instrument: the troublesome large and changing background drifts. Means to accomplish this were built into both the NBS graphite and water calorimeters. The

drifts are quickly reduced to tolerable levels in the water calorimeter because of the drift control method of changing the power between two immersed electrodes. The water calorimeter also has additional desirable features of being relatively simple to construct and to operate. Furthermore, all its internal components are relatively rugged and easily accessible for possible repair or replacement. This is in striking contrast to painstakingly rebuilding delicate nested bodied structures of solid calorimeters once internal troubles occur. The operation of the water calorimeter was virtually trouble-free on every day of operation. In these respects, the first of two phases of investigation was essentially completed: that of overcoming the physical problems in making the calorimeter an effective and accurate instrument for measuring a temperature rise at a point along a temperature profile in water.

Finally, it should be noted that the instrument measured a temperature rise with more assurance than it measured absorbed dose, thus the second phase of the investigation is only in the initial stage: the investigation of irradiation effects produced by different beams, absorbed dose rates, and accumulated absorbed dose that may cause significant positive or negative heat defects at the point of measurement.

The primary conditions of the initial investigations reported here are for three-minute irradiations with cobalt-60 gamma rays, a dose rate near 18 mGy/s, and an accumulated dose of 150 Gy. The mean of the standard deviations of daily sets of measurements was 0.6 percent. Satisfactorily reproducible results were obtained by using water with a wide range of impurities and with distilled water agitated with nitrogen or oxygen. The measured absorbed dose rate to distilled water was 3.5 percent higher than previous measurements with a graphite calorimeter that were converted to absorbed dose to water. Tests showed that there was no evidence of water convection.

## 20. References

- [1] Domen, S. R. Absorbed dose water calorimeter, *Med. Phys.* 7 (2): 157-159; 1980 March-April.
- [2] Domen, S. R. Absorbed dose water calorimeter, U.S. Patent Number 4,312,224; 1982 January.
- [3] Domen, S. R. An improved absorbed dose water calorimeter, AAPM Meeting, *Med. Phys.* 8 (4): 552; 1981 July-August.
- [4] Domen, S. R. Theory, performance, and measured results with an improved absorbed dose water calorimeter, Electron Dosimetry and Arc Therapy Symposium, Univ. of Wisconsin, 1981 September.
- [5] ICRU Rep. No. 14, Appendix B. Washington, D.C.: ICRU Publications; 1969.
- [6] Domen, S. R.; Lamperti, P. J. Comparisons of calorimetric and ionometric measurements in graphite irradiated with electrons from 15 to 50 MeV, *Med. Phys.* 3(5): 294-301; 1976 September-October.
- [7] *Handbook of chemistry and physics*, Cleveland: Chemical Rubber Publishing Co.
- [8] Domen, S. R.; Lamperti, P. J. A heat-loss-compensated calorimeter: theory, design, and performance, *J. Res. Nat. Bur. Stand. (U.S.) (Phys. and Chem.)*, 78A(5): 595-610; 1974 September-October.
- [9] Pruitt, J. S.; Domen, S. R.; Loevinger, R. The graphite calorimeter as a standard of absorbed dose for cobalt-60 gamma radiation, *J. Res. Nat. Bur. Stand. (U.S.)* 86(5): 495-502; 1981 September-October.
- [10] Schmidt, E., *On the application of the calculus of finite differences to heating and cooling problems in engineering*, *Frappels Festschrift*, Springer, Berlin, p. 179 (1924).
- [11] Binder, L., *On the thermal conduction to the environment and the temperature increases of electrical machines*, Wilhelm Knapp, Halle, Germany, p. 20 (1911).
- [12] Ingersoll, L. R., Zobel, O. J., and Ingersoll, A. C., *Heat conduction*, Madison, WI, The University of Wisconsin Press, 209-213 (1954).
- [13] Fishenden, M., and Saunders, O. A., *An introduction to heat transfer*. The Clarendon Press, Oxford, pp. 54-60 (1950).
- [14] Patton, T. C., Graphical methods for temperature distribution with unsteady heat flow, *Ind. Eng. Chem.*, 36(11): 990-996; 1944 November.
- [15] Benedict, R. P., Transient heat flow, *Electro-Technology, Sci. and Eng. series*, 94-112; 1961 December.
- [16] Schmidt, E., *Thermodynamics*, The Clarendon Press, Oxford, 428-433 (1949).
- [17] Filimonov, A., Absorbed dose measurements in gelatin, Ph.D. Thesis (1973), Univ. of NC.
- [18] McLaughlin, E., Thermal conductivity of liquids and dense gases, *Chem. Rev.* 64, 389-428 (1964).
- [19] Velarde, M. G., and Normand, C., Convection, *Sci. Am.* 243(1): 93-; 1980 July.
- [20] Carslaw, H. S., and Jaeger, J. C., *Conduction of heat in solids*, 2nd ed., Oxford, The Clarendon Press; 1959. 510 p.
- [21] Clark, F. M., *Insulating materials for design and engineering practice*, New York, John Wiley and Sons, Inc., pp. 421 and 530 (1962).
- [22] Becker, J. A., Green, C. B., and Pearson, G. L., Properties and uses of thermistors—thermally sensitive resistors, *Electrical Engineering*, 1946 November.
- [23] Clark, L. E., Report on the exactness of fit of thermistors to the equation  $\log R = A + B/(T + \Theta)$  and  $\log R = A + B/(T + \Theta) + CT$ , USASRD Tech. Rep. No. 2168, U.S. Army Signal Res. and Dev. Lab., Fort Monmouth, NJ, (Jan. 1961).
- [24] Theory and application of self-heated thermistors, V1210-revised, Victory Engineering Corporation, Springfield, NJ.
- [25] Draganic, I.G., and Draganic, Z. D., *The radiation chemistry of water*. New York and London: Academic Press; 1971. 242 p.
- [26] Spinks, J. W. T., Woods, R. J. *Radiation chemistry*. New York: J. Wiley & Sons; 1976. 504 p.
- [27] Boyd, A.W., private communication (1981).
- [28] Hart, E. J., and Fielden, E. M., Submicromolar analysis of hydrated electron scavengers, *Advan. Chem. Ser.* 50, 253-262 (1965).
- [29] Marles, A. Ph.D. Thesis (1981), Univ. of Texas (Houston).
- [30] Busulini, L. et al. Dosimetry of Co-60  $\gamma$ -rays by a simple calorimetric method, *Int. J. Appl. Radiat. Isotop.* 19(8): 657-662; 1968 August.
- [31] Kaarles, R., Report of the BIPM Working Group on the statement of uncertainties (1980).
- [32] Cottens, E. Geabsorbeerde dosis calorimetric bij hoge energie elektronenbundels en onderzoek van de ziersulfaat dosimeter, Ph.D. Thesis, Univ. of Gent, Belgium, (1979-1980).

# Torsional Splittings and Assignments of the Doppler-Limited Spectrum of Ethane in the C-H Stretching Region\*

A. S. Pine\*\* and W. J. Lafferty\*\*

National Bureau of Standards, Washington, DC 20234

November 18, 1981

The Doppler-limited absorption spectrum of the C-H stretching region of ethane has been recorded at  $T \approx 119$  K with a tunable difference-frequency laser spectrometer. The strong torsional hot band structure at room temperature is eliminated at 119 K, and the enhanced resolution from the Doppler width reduction allows us to observe small torsional splittings. The two fundamentals in the region,  $\nu_7$ , a perpendicular band and,  $\nu_5$ , a parallel band have been essentially completely assigned as have a large number of transitions in the parallel component of the  $\nu_8 + \nu_{11}$  combination band. A number of perturbations of both global and local nature have been observed. The complete spectrum and a listing of transition wavenumbers, intensities and assignments are presented here to facilitate identification and quantitative analysis of ethane in a variety of monitoring applications. Precise ground state rotational constants have been determined from combination differences.

**Key words:** C-H stretching region; difference-frequency laser; Doppler-limited resolution; ethane; ground state constants; infrared spectrum; low temperature spectrum; torsional splittings.

## 1. Introduction

Although ethane is the simplest hydrocarbon containing a saturated carbon-carbon bond and has very high symmetry ( $D_{3d}$ ), the extremely dense and complex rotational fine structure of its infrared bands has defied complete resolution until recent advances in Doppler-limited tunable laser and Fourier transform instrumentation. Previously, high-quality grating spectra of the C-H stretching region at  $0.025 \text{ cm}^{-1}$  resolution permitted Cole, Lafferty and Thibault [1]<sup>1</sup> to partially assign the rotational transitions of the  $\nu_7$  perpendicular band. More recently Cole, Cross, Cugley and Heise [2] deconvolved similar grating data to  $\sim 0.015 \text{ cm}^{-1}$  to observe somewhat more structure in this same band. We present here the Doppler-limited absorption spectrum of the infrared active C-H stretches of ethane recorded at  $T \approx 119$  K (Doppler FWHM =  $0.0043 \text{ cm}^{-1}$ ) with a tunable difference-frequency laser spectrometer. Both fundamentals,  $\nu_7$  centered at  $2985.39 \text{ cm}^{-1}$  and the parallel band  $\nu_5$  at  $2895.67 \text{ cm}^{-1}$ , have been fully resolved

and assigned, and much of the  $\nu_8 + \nu_{11}$  combination band has been identified.

The principal complications in the infrared spectrum of  $\text{C}_2\text{H}_6$  arise from the relative torsional motion of the two methyl groups about the saturated C-C bond [3]. The moderate potential barrier (of  $\sim 1024 \text{ cm}^{-1}$ ) to free internal rotation leads to a low frequency torsional mode  $\nu_4$  at  $\sim 290 \text{ cm}^{-1}$  as determined by a number of calorimetric [4,5] and spectroscopic [6,7] techniques. This mode is highly excited at room temperature giving rise to "hot bands" associated with each normal band originating in the ground vibrational state. These hot bands are effectively suppressed in the present study by maintaining the ethane sample at the lowest possible temperature above the vapor condensation point. Overtones and combination states of this low frequency torsional mode are also in Fermi or Coriolis resonance with virtually all the higher vibrations of the molecule, causing severe perturbations whose complexity increases dramatically with the wavenumber of the other bands because of the increasing number of possible combinations.

Tunneling through the torsional potential barrier creates a further doubling of the energy levels of the molecules which may be manifest as small splittings in the rovibrational transitions as discussed by Susskind [8]. However, for nontorsional modes, such as those studied here, the barrier and, hence, the torsional split-

\*The experimental portion of this work was performed while the author was with Lincoln Laboratory of the Massachusetts Institute of Technology under NSF Contract #NSF/ASRA/DAR 78-24562. A preliminary account of this work appears in the NSF Final Report entitled "Tunable Laser Survey of Molecular Air Pollutants: Doppler-Limited Spectra of the C-H Stretching Bands of Formaldehyde, Ethylene, Ethane and Allene," January 1980.

\*\*Molecular Spectroscopy Division, National Measurement Laboratory.

<sup>1</sup>Figures in brackets indicate literature references at the end of this paper.

tings are not expected to vary significantly from the ground state. Thus the splittings for nontorsional infrared transitions, which arise from the *difference* in the splittings of the upper and lower vibrational levels [8], are expected to be unresolvable, even at the Doppler limit. Nevertheless the resonant interactions with torsional overtones and combinations, mentioned above, induce variations in the barrier giving rise to observable torsional splittings in the present work. Some of these are illustrated in figure 1 for the region around  $RQ_5$  of the  $\nu_7$  band, as brought out by the resolution enhancement and spectrum simplification resulting from lowering the ethane temperature. The torsional doublets of the  $RR_2(7)$  and  $RR_3(4)$  lines and the interleaved  $RQ_5$  subbranch are unambiguously characterized by their nuclear spin statistical weight intensity ratios calculated by Wilson [9].

The first observation of torsional splitting in ethane was made in diode laser spectra of the  $\nu_9$  band by Patterson, Flicker, McDowell and Nereson [10]. These splittings also arise from perturbations, induced by a resonance with  $3\nu_4$ ; but since that is the only possible

resonance with  $\nu_9$ , that band is more amenable to analysis than the complex C-H stretching bands. Two detailed studies of the  $\nu_9$  band are now in progress [11,12]; both are based on Doppler-limited diode laser spectra of the Q branches and comprehensive, precision Fourier transform interferometer data. In the present study of the C-H stretches, the torsional splittings exhibit many interesting patterns indicative of a variety of interactions and perturbing states.

The complex low temperature Doppler-limited spectrum of ethane between 3051 and 2862  $\text{cm}^{-1}$  is given in this report along with a listing of transition wavenumbers, intensities and assignments. We also discuss the assignment procedure and the more interesting spectral features associated with the perturbations, torsional splittings and combination bands. A precise set of ground state rotational constants obtained from combination differences is given since microwave data do not exist for this nonpolar molecule. These definitive spectra are truly characteristic of the molecule without instrumental distortion since the laser linewidth ( $\sim 0.0003 \text{ cm}^{-1}$ ) is much narrower than the Doppler width. Hence, the spectral patterns should be useful for the identification and quantitative analysis of ethane for a number of practical applications. For example, ethane is a principal constituent of natural gas (0 to 20% with  $\sim 7\%$  average) and can be used for labelling sources, detecting leaks and monitoring pipeline transmission and LNG carriers [13]; it is one of the major hydrocarbon emissions in automobile exhausts and can interfere with the measurement of more toxic components [14]; and it has been observed in the atmosphere of several outer planets [15] with significance to extraterrestrial organic chemistry.

## 2. Experimental Considerations

The high resolution ethane spectra reported here were recorded with a tunable difference-frequency laser spectrometer developed at MIT Lincoln Laboratory for obtaining precise and comprehensive Doppler-limited vapor-phase spectra in the 2.2 to 4.2  $\mu\text{m}$  region. The instrument is based on the nonlinear optical down-conversion of CW visible single-mode argon ion and tunable dye lasers in a  $\text{LiNbO}_3$  mixing crystal. The basic operating characteristics of the system [16] along with techniques of drift compensation [17], stabilization and automated data processing [18] and linear scan control [19] have been detailed elsewhere, so we will discuss here only those features pertinent to the present investigation.

Since the C-H stretching bands of ethane are quite extensive (covering  $\sim 200 \text{ cm}^{-1}$ ), the difference-frequency system was operated in a broad survey, rapid scan mode. The absorption spectra were recorded in continuously

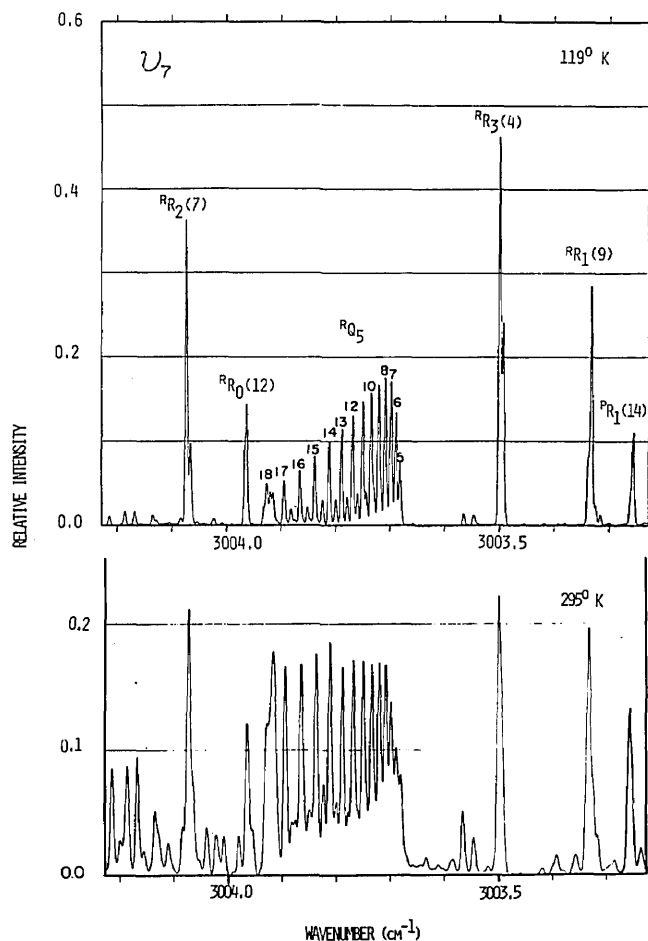


FIGURE 1. Comparison of the ethane spectrum in the region of the  $RQ_5$  subbranch of the  $\nu_7$  band for temperatures of 119 K and 295 K.

scanned  $3.75 \text{ cm}^{-1}$  segments overlapped at intervals of  $3 \text{ cm}^{-1}$ . The scan rate was  $0.0125 \text{ cm}^{-1}/\text{s}$  or  $375 \text{ MHz}/\text{s}$  so each segment was scanned in 5 minutes. The post-detection time constant was 40 ms (corresponding to  $5 \times 10^{-4}$  or 15 MHz) which was short enough to allow full response to the sharp Doppler-broadened lines (FWHM = 128 MHz for  $\text{C}_2\text{H}_6$  at  $T \approx 119 \text{ K}$ ) but long enough for good signal-to-noise ratio of  $\sim 500$ . The transmission traces were digitized at a 20 Hz rate (6000 points per segment,  $6.25 \times 10^{-4} \text{ cm}^{-1}$  per point) for data storage and subsequent numerical processing. The instrumental width, due primarily to the dye laser free-running jitter, was about 10 MHz FWHM. Thus the effect of instrumental broadening is negligible since convolution of the Gaussian profiles of the Doppler and laser distributions results in the widths adding in quadrature.

The ethane spectra were recorded over a period of 2 days. Each day's run was calibrated against  $\text{CH}_4$  reference lines from the Fourier transform interferometer data of Tarrago *et al.* [20]. The first day's run was interpolated between the R(3) and P(7) manifolds of the  $\nu_3$  band of  $\text{CH}_4$  while that of the second day between P(7) and P(15) using a 5 cm confocal Fabry-Perot interferometer with a free spectral range of  $0.050027(1) \text{ cm}^{-1}$ . The interorder spacing of this scan calibration interferometer can be measured to a precision of  $\pm 2 \times 10^{-7} \text{ cm}^{-1}$  over a  $100 \text{ cm}^{-1}$  interval, but it exhibits a small frequency dispersion and overnight thermal shifts which must be checked during extended runs. The determination of the spectral line wavenumbers for these rapid survey scans was made to a relative precision of  $\sim \pm 4 \times 10^{-4}$  which was slightly better than the least reading for the digitizing grid. The absolute accuracy of the wavenumbers may be slightly worse due to uncertainties in the reference line standards.

In order to obtain linestrength information from the transmission traces, one must account for Beer's law,  $\alpha(\omega) = (\rho L)^{-1} \ln(B(\omega)/S(\omega))$ . Here  $\alpha(\omega)$  is the absorption coefficient in units of  $(\rho L)^{-1}$  where  $\rho$  is the sample density and  $L$  is the cell length;  $S(\omega)$  is the transmission and  $B(\omega)$  is the empty cell baseline. In this case the baseline was entered manually on a coarse grid ( $0.125 \text{ cm}^{-1}$ ) since it was not practical to evacuate the cold cell and refill for each trace. Also our automatic baseline interpolation routine, which keys on the background between lines, did not work reliably for ethane since the spectrum was so dense. The manual baseline estimation is only adequate to  $\sim \pm 1$  percent because of strong channeling of the spectra from the cold cell windows. The baseline uncertainties dominate the relative line strength errors since the actual transmission spectra are reproducible to  $\approx \pm 0.2$  percent. In addition, absolute intensities depend on measurement accuracy of the cell length ( $29.4 \pm 0.1 \text{ cm}$ ), the fill pressure ( $225 \pm 4 \text{ m Torr}$  at  $T = 295 \pm 1$

K), the sample temperature (held at  $T = 119 \pm 3 \text{ K}$ ) and, to a lesser extent, on sample purity. Here we used natural isotopic ethane of research grade from Matheson with a quoted purity of 99.96 percent; it exhibited no trace of methane or other simple hydrocarbons in the spectrum. In the atlas, corrections are made for the isotopic abundance of  $^{12}\text{C}_2\text{H}_6$ .

The sample cold cell was a copper tube with thinned end sections for stress-free epoxy mounting of ZnSe windows required because of differential thermal contraction. Copper cooling coils were soldered to the tube and an evacuable stainless steel jacket with  $\text{CaF}_2$  windows provided thermal isolation. The cell was cooled by manually controlling the flow of He gas through a liquid  $\text{N}_2$  heat exchanger and then through the cell coils. The temperature was measured with a single platinum resistance thermometer imbedded in the copper cell wall. The uniformity of the temperature is expected to be better than the manually controlled temperature setting which dominates the absolute intensity errors ( $\sim \pm 3\%$  for low  $J$  and  $K$ ).

### 3. Spectral Features

The fundamentals,  $\nu_5$  and  $\nu_7$ , are examples of parallel and perpendicular bands whose assignment, as is customary, is based on selection rules, "missing lines" and consistent ground state combination differences. Where observed, the torsional doublets provide a definitive confirmation of the  $K$  and some  $J$  assignments because of their distinctive intensity ratios for particular rotational quantum numbers. The nuclear spin statistical weights for these doublets derived by Wilson [9] yield the intensity ratios of 4:1 for  $K$  not a multiple of 3; 2:1 for  $K$  a multiple of 3 but not 0; and for  $K = 0$  a ratio of 3:1 for  $J$  even and 5:3 for  $J$  odd. These ratios are illustrated in figure 1 for  $K = 2, 3$  and 5 levels of  $\nu_7$  and in figure 2 for the  $K = 0, 2$  and 4 cases in the P(6) and P(7) manifolds of  $\nu_5$ . Each torsional component is labelled in the atlas according to the ground state symmetry species of the permutation-inversion group  $G_{36}^+$  for ethane-like molecules exhibiting internal rotation as discussed by Hougen [21].

Though the assignments for the fundamentals are firm and rather complete, a number of severe perturbations are observed due to accidental resonant crossings of energy levels. However, for both  $\nu_5$  and  $\nu_7$  the initial  $K$  subband lines at  $J = K$  appear regular and undisturbed. This implies that both bands are affected by X-Y Coriolis interactions since the matrix elements governing such a resonance are proportional to  $[J(J+1) - K(K+1)]^{1/2}$ . In most cases the effect of such a perturbation is to change the effective B values of individual subbands but to leave the  $K$  structure unaffected. However, for the

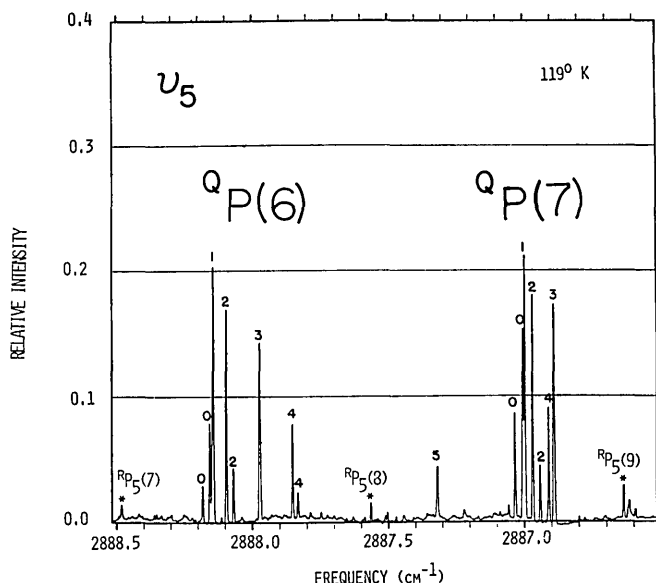


FIGURE 2. Spectrum of  $C_2H_6$  near the P(6) and P(7) manifolds of the  $\nu_5$  band at  $T = 119$  K. Perturbation-induced lines are labelled with an \*.

very close resonances observed in some of the subbands here, the perturbations are severe enough that they cannot be fit using a standard power series expansion. In  $\nu_7$  such a resonance is dramatically exhibited by the  $RQ_5$  subbranch shown in figure 1. This subbranch is much more spread out than lower  $RQ_K$  subbranches and is degraded in opposite direction to the higher  $RQ_K$  subbranches; it also shows an abrupt head and gap above  $J = 18$ . In addition, there are numerous smaller local perturbations, one of which, shown in figure 3, occurs in the

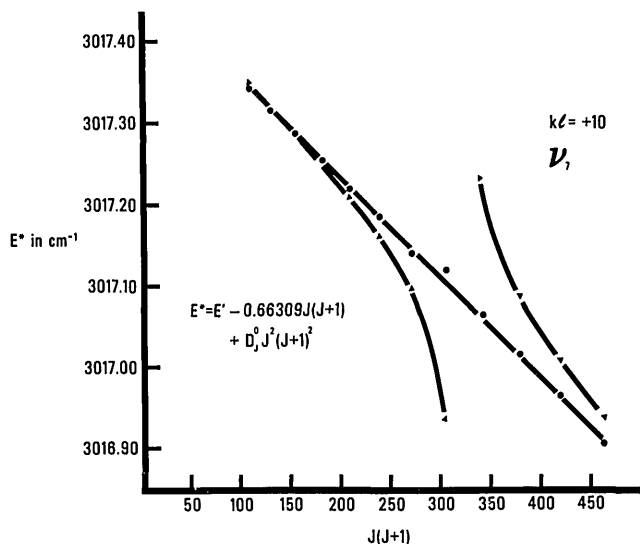


FIGURE 3. Torsional splittings in the  $K' = 10$ ,  $\Delta K = +1$  subband of  $\nu_7$ . The dots represent the stronger  $A_{1s} - A_{2s}$  symmetry components and the triangles represent the weaker  $E_{3s} - E_{4s}$  symmetry components.

$K = 10$ ,  $\Delta K = +1$  subband, manifest in a rapid increase in the torsional splitting as a function of  $J$  to a value  $\sim 0.1$   $cm^{-1}$  at  $J' = 17$ , above which it suddenly reverses sign and decreases again to higher  $J'$ . In some subbands of  $\nu_7$  the torsional splitting is constant or a monotonic function of  $J(J + 1)$  and in others it appears to be irregular.

On the other hand, perturbations in  $\nu_5$  appear to be dominated by a strong resonance near the  $K = 5$  energy level stack. The effect of this resonance is to degrade the  $K = 5$  subband to lower frequency while the others are degraded to higher frequency as shown in figure 4. Despite the degradation, the subband "origins" at  $J = K$  fall on a relatively unperturbed straight line, as seen in figure 4, implicating the X-Y Coriolis interaction. From

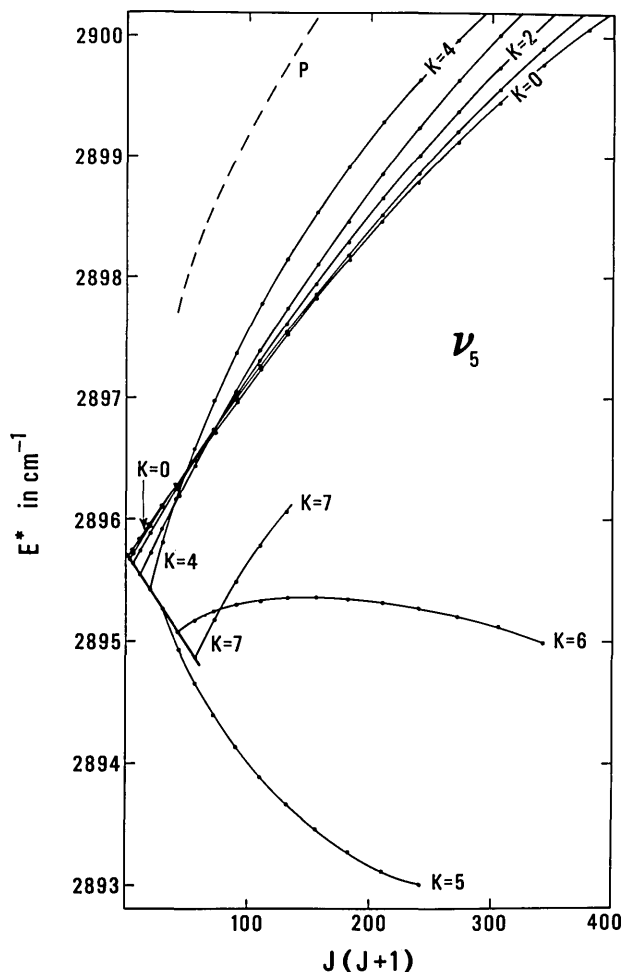


FIGURE 4. Reduced energy for the stronger torsional components of the  $K$  subbands of  $\nu_5$ . The dashed line represents the  $K = 6$  subband of an  $E_u$  vibration perturbing  $K = 5$  of  $\nu_5$  and observed by resonant mixing. Here  $E^* = \nu_5(J'K, J''K'') + B_5 J''(j'' + 1) - B_5^* J'(J' + 1)$  where  $\nu_5(J'K', J''K'')$  are the transition wavenumbers for the band and  $B_5^* = 0.6624$   $cm^{-1}$  is chosen to adjust the scale of the plot.

the  $a_{2u}$  symmetry of  $\nu_5$  and the  $E_g$  species for the vibrational operator of the X-Y Coriolis coupling, we can conclude that the perturbing vibration has  $E_u$  symmetry. The resonance mixing is strong enough near the crossover that the perturbing levels accompanying the  $K = 4$  and 5 subbands borrow sufficient intensity to be observed in the spectrum. The levels perturbing  $K = 5$  are positioned along the dashed curve, labelled P in figure 4, and a few of the corresponding perturbation-induced transitions are shown in figure 2, labelled with an asterisk. We believe that these perturbing levels belong to the  $K = 6$  subband of the resonant state because of the  $\Delta K = \pm 1$  requirement for the X-Y Coriolis interaction and the fact that the  $J = K = 5$  level of  $\nu_5$  is unperturbed. The  $K$  assignments for the perturbing subbands must be regarded as tentative since we have so few series, but they are consistent with the intensity ratios of their torsional doublets which have splittings comparable to those in  $\nu_5$ .

The perturbation-induced torsional splittings take the interesting form shown in figure 5. For the odd  $K$  subbands the  $J = K$  transitions are not observably split, but at higher  $J$  the splitting increases regularly, to as much as  $\sim 0.1 \text{ cm}^{-1}$  in some cases. Even for the most perturbed subband,  $K = 5$ , the doublet of the  $J = 5$  transition is not resolved while  $J = 6$  is. In the even  $K$  subbands however, the  $J = K$  transitions are all split by  $\sim 0.02 \text{ cm}^{-1}$  and, except for  $K = 6$ , the splittings increase slowly with  $J$ . For  $K = 6$  the splittings decrease with  $J$ , become unresolved at about  $J = 14$  and are resolved again at higher  $J$  with the splittings reversed. We currently have no consistent model for this striking behavior of the torsional splittings in  $\nu_5$ . It is clear however, that recognizing the presence of torsional doubling was the key to assigning  $\nu_5$  which was missing in prior studies [1,2].

The combination bands present a somewhat more difficult situation to analyze. First there are ambiguities in

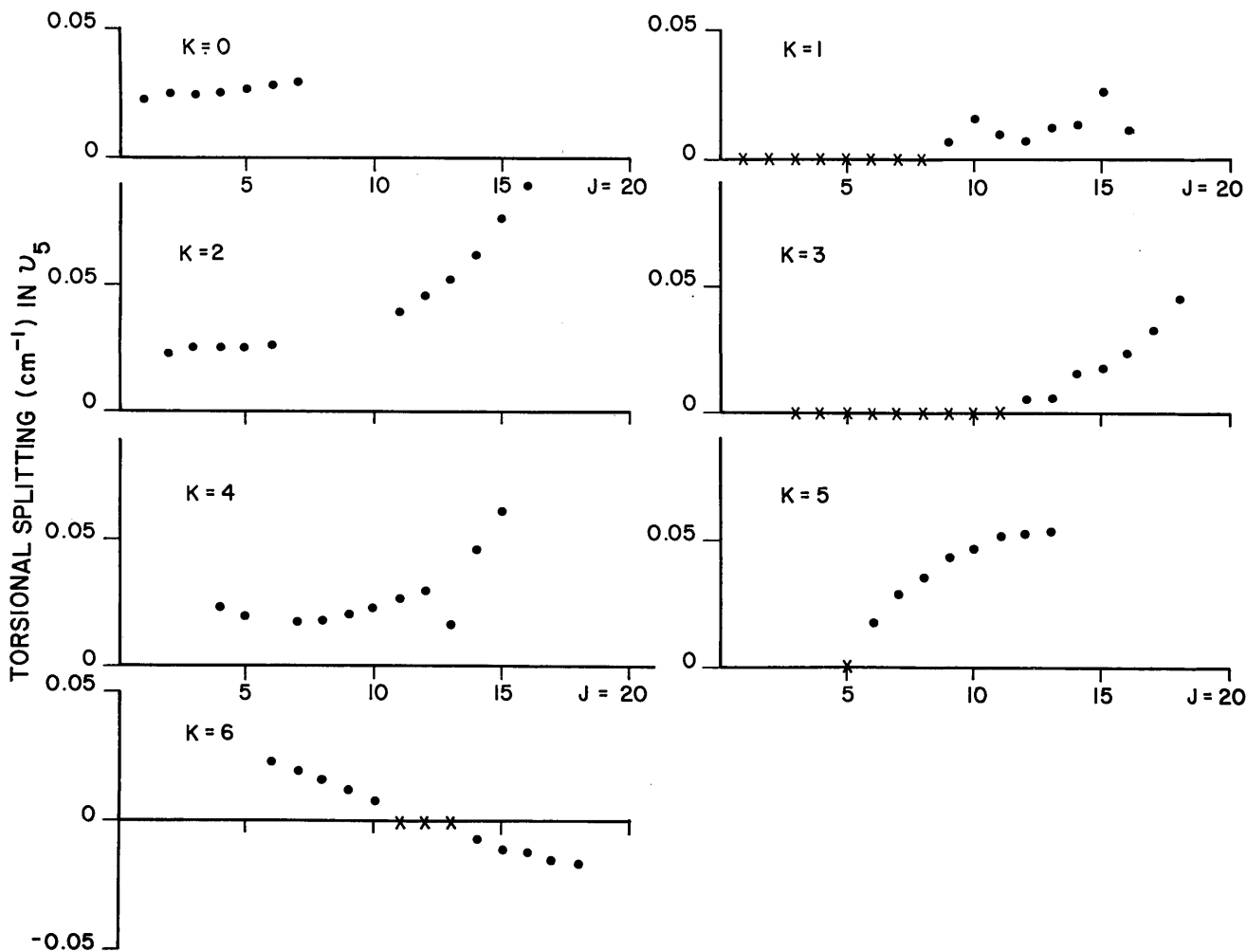


FIGURE 5. Torsional splittings in the  $\nu_5$  band of  $\text{C}_2\text{H}_6$  for  $0 \leq K \leq 6$ . Here X represents unresolved doublets.

the vibrational sublevel symmetries for the  $\nu_8 + \nu_{11}$  combination band since there are several components possible ( $e_u \times e_g = A_{1u} + A_{2u} + E_u$ ). The  $E_u$  component of  $\nu_8 + \nu_{11}$  should result in a perpendicular band with an effective  $\xi_+ = -(\xi_8 + \xi_{11}) \simeq +0.71$  from the data of Nakagawa and Shimanouchi [22], leading to  $P, R, Q_K$  subbranches spaced by  $\sim 7.8 \text{ cm}^{-1}$ . We see no direct evidence for such a band in our spectrum. On the other hand, we see at least two moderately strong parallel bands belonging to the  $A_u$  components. To first order only the  $A_{2u}$  mode should be infrared active, but the normally inactive  $A_{1u}$  mode may borrow intensity from  $A_{2u}$  via a Z-type Coriolis interaction proportional to  $H_{12} = -AK\xi_-$ , where  $\xi_- = |\xi_8 - \xi_{11}|$ , as discussed by Hougen [23]. The appearance of the  $A_1 - A_2$  band also depends on the separation,  $\Delta E$ , between these two states. In the uncoupled limit where either  $\Delta E$  is large or  $H_{12}$  is small, the mixing is negligible and only transitions to the ordinary  $A_{2u}$  parallel band would be observed. If  $\Delta E = 0$  the mixing will be complete and the resulting infrared band will have the appearance of a perpendicular band (with parallel band intensity patterns [24]) with a Coriolis constant  $\xi_-$ . Intermediate cases require a more detailed calculation. The two modes can be distinguished by the presence of a  $K = 0$  subband allowed for  $A_{2u}$  and forbidden for  $A_{1u}$  since the Coriolis coupling is proportional to  $K$ .

A number of parallel-type subbands were assigned in this region by first identifying strong series in the R branch with estimated  $J$  and  $K$  and calculating the Q and P lines using the precise ground state combination differences obtained from the fundamental bands. If the series matches observed lines to within  $\sim 0.0005 \text{ cm}^{-1}$  and the intensities are consistent, then one can be quite confident of the  $J$  assignment. The  $K$  assignment is less certain because the combination differences are not strongly  $K$  dependent. However again, where torsional splittings are observed ( $K = 0$  and 3 in this instance) the  $K$  assignments are verified by the doublet intensity ratios. The other subbands were assigned  $K$  values according to the missing lines resulting from  $J \geq K$ . In the P and R branches, the lower  $J$  transitions are weak and often obscured and overlapped by stronger series. For the Q branch of a parallel band, the lowest  $J$  line is strongest, so the Q branches were most useful in establishing the  $K$  numbering of the series. One subband has a very small value of  $B' - B''$  and its Q subbranch, falling at  $2958.0863 \text{ cm}^{-1}$ , is not resolved. This subband is tentatively believed to involve  $K = 2$  transitions with an uncertainty of  $\pm 1$  in  $K$ . The prominent feature in the spectrum at about  $2953.8 \text{ cm}^{-1}$  consists of Q subbranches ranging from  $K = 2$  to 6. The lower  $K$  subbands have origins both above and below this feature; namely  $K = 0$  at  $2955.6699(2) \text{ cm}^{-1}$ ,  $K = 1$  at

$2956.1196(4) \text{ cm}^{-1}$  and  $2951.9962(2) \text{ cm}^{-1}$  and  $K = 2$  at  $2958.0866(8) \text{ cm}^{-1}$ .

Although the majority of lines occurring in the combination band region have been assigned, their subbands are badly perturbed and many strong series remain unidentified. The  $\nu_8$  and  $\nu_{11}$  band is expected to have both Fermi and Coriolis interactions with the fundamentals and with other higher order overtones and combinations. Also Hougen [25] has pointed out the possibility of an interaction between the  $A_{1u}$  component and the totally symmetric  $a_{1g}$  C-H stretching mode,  $\nu_1$ , in ethane-like molecules with an intermediate barrier. This interaction, strictly forbidden for rigid  $D_{3d}$  molecules, is permitted during the torsional tunneling motion. It is of course expected to be weak in ethane but the near degeneracy with the Raman-active  $\nu_1$  mode at  $2953.7 \text{ cm}^{-1}$  as determined by Lepard, Shaw and Welsh [26] may account for some of the observed anomalies in this band.

#### 4. Ground State Constants

Since ethane is nonpolar, no microwave data are available for the ground state rotational constants. Thus we have calculated the rotational constants from the large number of ground state combination differences (CDs) collected during the course of the assignment of the C-H stretching bands. We have restricted the CDs used in obtaining the constants to those obtained from the two fundamentals,  $\nu_5$  and  $\nu_7$ , since the lines from these bands are stronger, more precisely measured than those in the combination band, and the assignment is firm in these bands. In calculating CDs from transitions which were split into torsional components, the lines were assigned the ground state symmetry of Hougen [21] according to the observed intensity ratios, and differences were taken between components of the same symmetry. A number of lines were unsplit and, if these lines were sharp, CDs between them were also included in the fit. Lines for which the torsional splitting was only poorly resolved were not included in the fit.

The ground state constants of a prolate symmetric top molecule are defined by the usual term value equation:

$$F(J,K) = (A_0 - B_0)K^2 + B_0 J(J+1) - D_J^J J^2(J+1)^2 - D_J^K K^2(J+1) - D_K^K K^4.$$

No "forbidden" transitions with  $|\Delta K| > 1$  were observed in the spectrum so only the coefficients of the  $J$ -dependent terms can be determined. A total of 766 CDs were obtained from the fundamental bands of which two thirds were from torsionally split lines. Originally CDs of each symmetry species were fit separately to determine if there were any dependence of the rotational constants on

symmetry or the corresponding nuclear spin. No statistically significant differences were found so all CDs were then fit simultaneously, resulting in the ground state constants given in table 1.

TABLE 1: Ground State Constants of  $^{12}\text{C}_2\text{H}_6$  in  $\text{cm}^{-1}$

$A_0$	$= 2.671^{(a)}$
$B_0$	$= 0.6630271(14)^{(b)}$
$D_0^K$	$= 1.09 \times 10^{-5} \text{ (c)}$
$D_0^{JK}$	$= 2.660(29) \times 10^{-6} \text{ (b)}$
$D_0^J$	$= 1.0312(26) \times 10^{-6} \text{ (b)}$

<sup>a</sup>Raman value for Ref. [26].

<sup>b</sup>Present work with uncertainties in parentheses representing one standard deviation.

<sup>c</sup>Calculated value from Ref. [22].

Not only does the combination difference fitting provide an excellent set of rotational constants, but it also reflects the measurement precision obtained in this experiment. The standard deviation of the fit is  $0.00055 \text{ cm}^{-1}$  or  $16.5 \text{ MHz}$ . Since the ground state fitting is performed on differences, the measurement uncertainty of an individual line is reduced by a factor of  $1/\sqrt{2}$  to  $\sim 12 \text{ MHz}$ . These ground state constants, given with near microwave precision, are certainly an improvement over prior lower resolution grating spectra determinations, and they are compatible with ultra precise Fourier transform interferometer data on  $\nu_9$  currently being analyzed [11].

## 5. Spectrum and Listing

We present in figure 6<sup>2</sup> the complete Doppler-limited absorption spectrum of ethane from  $3051 \text{ cm}^{-1}$  to  $2870$

$\text{cm}^{-1}$  recorded at  $T \approx 119 \text{ K}$ . Prominent Q branches are labelled for  $\nu_7$ , and the  $K = 0$  subband lines for the P(J) and R(J) manifolds are labelled for  $\nu_5$ . A listing of the measured transitions is given in table 2 consisting of the line center wavenumber, the peak intensity, the upper and lower state rotational quantum numbers when assigned, the ground state vibration-rotational-torsion symmetry in the  $G_{36}^\dagger$  group [21] when resolved (the subscript  $s$  is suppressed), the vibrational band code and the lower state energy. The vibrational band code is  $A$  for  $\nu_7$ ,  $B$  for  $\nu_8 + \nu_{11}$ ,  $C$  for  $\nu_5$ , and  $D$  for perturbation-induced lines. The lower state energy in wavenumbers is calculated from eq (1) using the precise rotational constants of table 1 and the more approximate values for  $A_0$  and  $D_0^K$  obtained from Raman spectra [26]. These ground state functions [3], are needed to compute the temperature dependence of the line intensities.

The intensity scale for figure 6 is given in  $(\text{Torr} - \text{m})^{-1}$  taken from the “raw” experimental fill pressure at room temperature and the cell length. However, the experiment was conducted at constant density since the cell was sealed when the temperature was lowered. Thus for the listing of table 2 we convert the peak intensity units to  $(\text{Amagat-cm})^{-1}$  by multiplying  $(\text{Torr} - \text{m})^{-1}$  by the factor  $(760/100) \times (295/273)/a = 8.397$  where  $a = 0.978$  is the isotopic abundance of  $^{12}\text{C}_2\text{H}_6$ .

The authors are grateful to A. Mooradian and P. M. Moulton of MIT Lincoln Laboratory for the loan of the cold cell. They are also indebted to J. T. Hougen for numerous helpful discussions on the torsional symmetry and interactions in ethane.

<sup>2</sup>Figure 6 and table 2 are displayed on pages 244-256. References are on page 256.

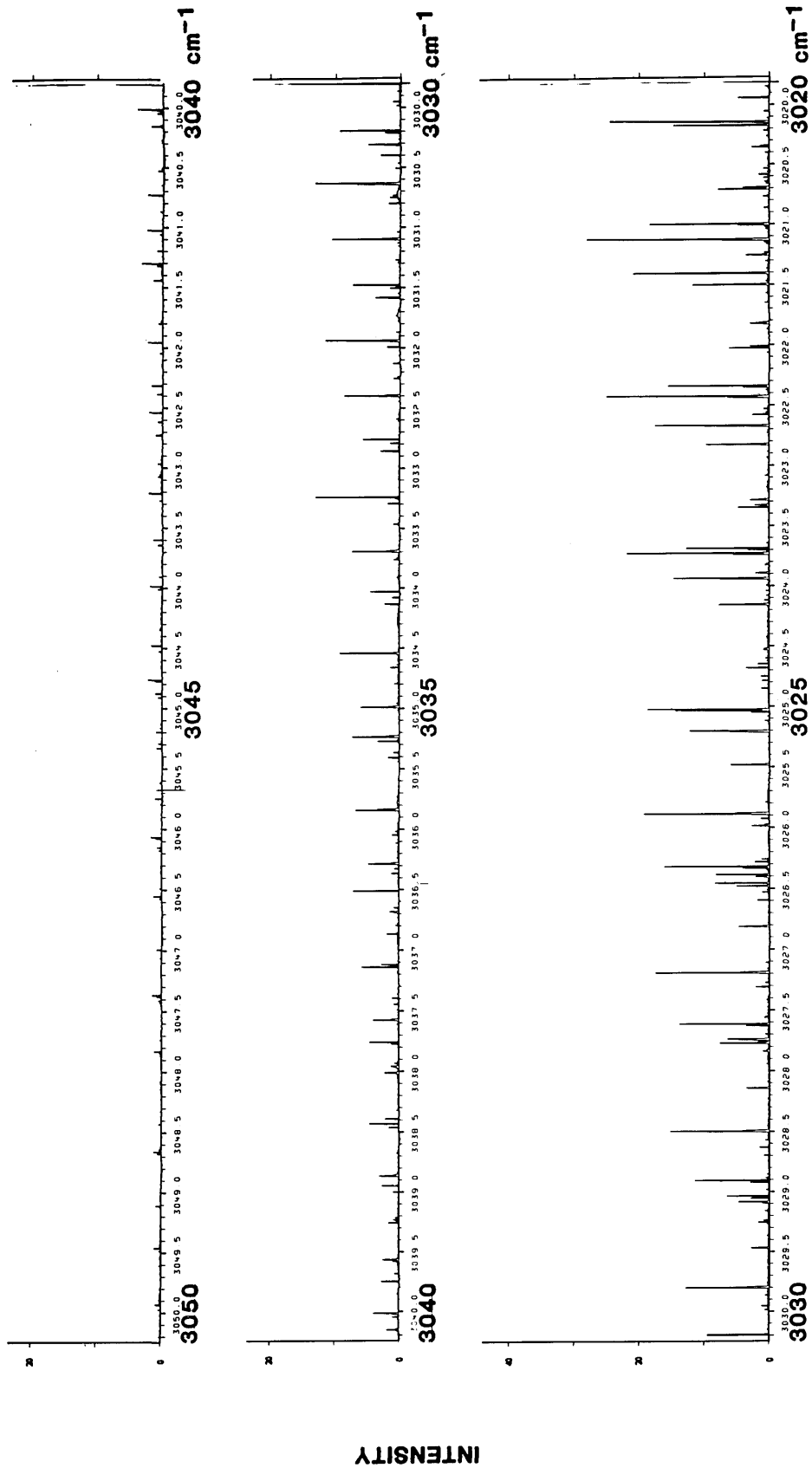


FIGURE 6. Doppler-limited spectrum of ethane at  $T = 119$  K. The intensity scale is in  $(\text{Torr}\cdot\text{m})^{-1}$  uncorrected for temperature or isotopes (see text).

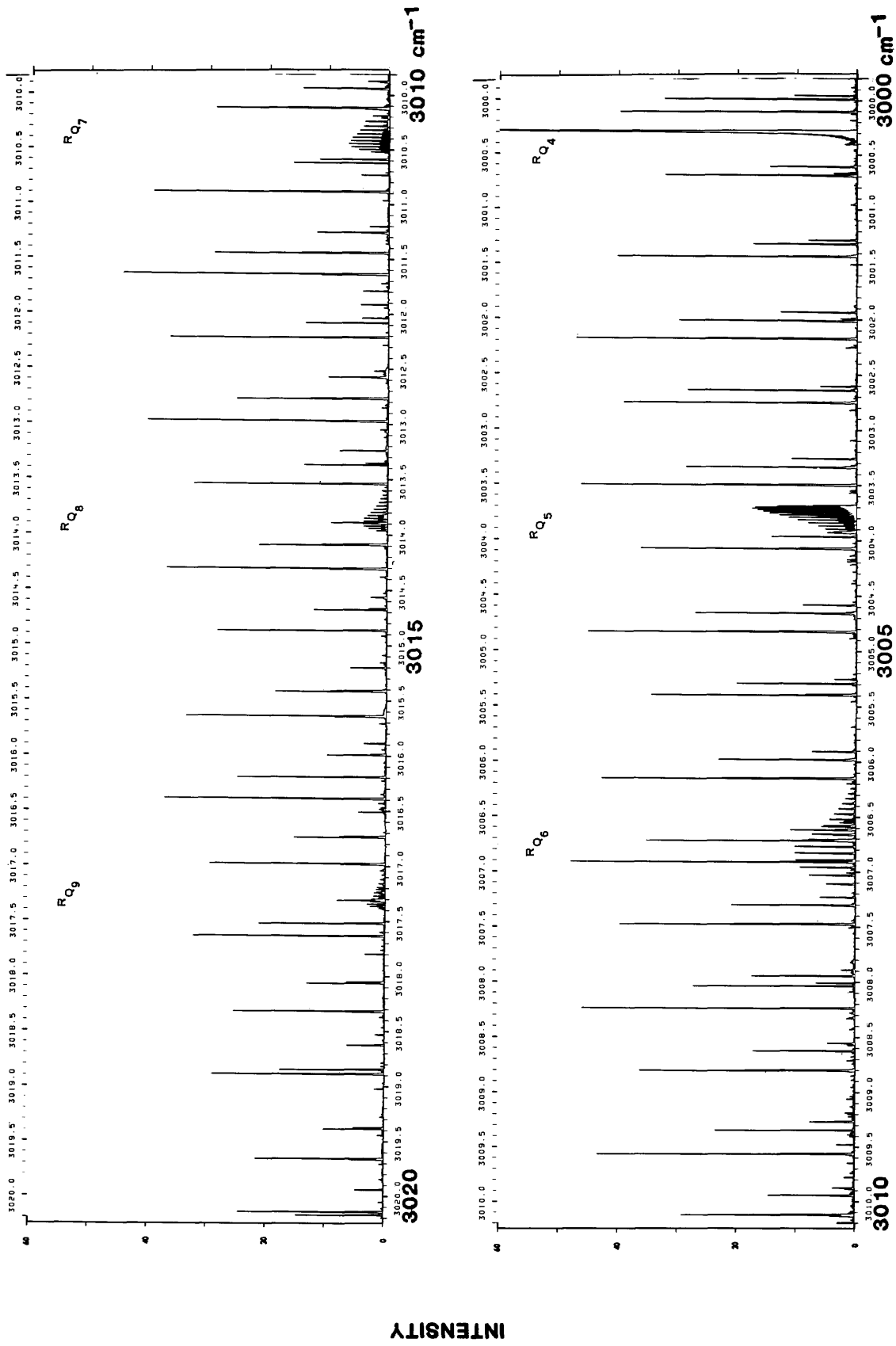


FIGURE 6. Continued

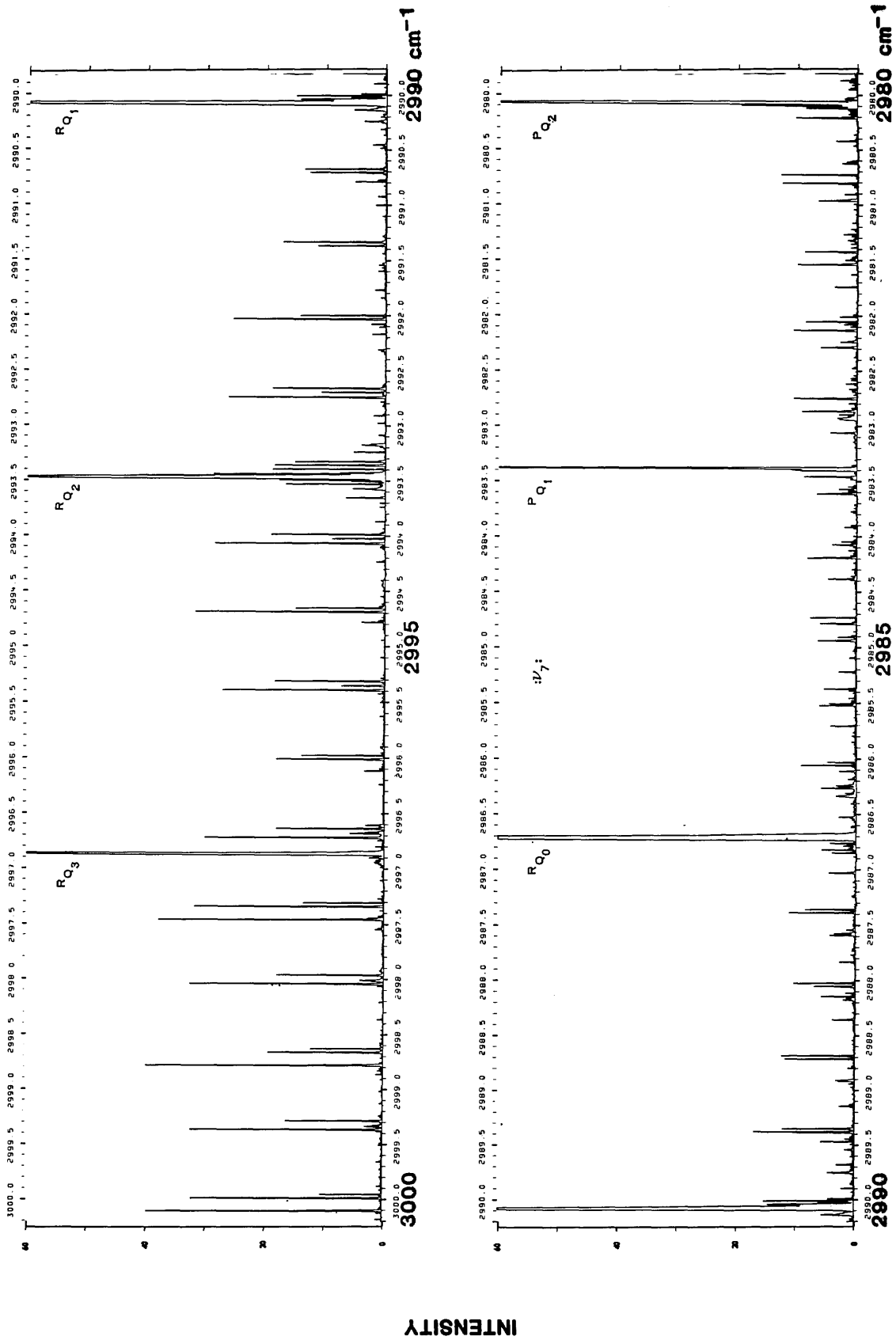


FIGURE 6. Continued

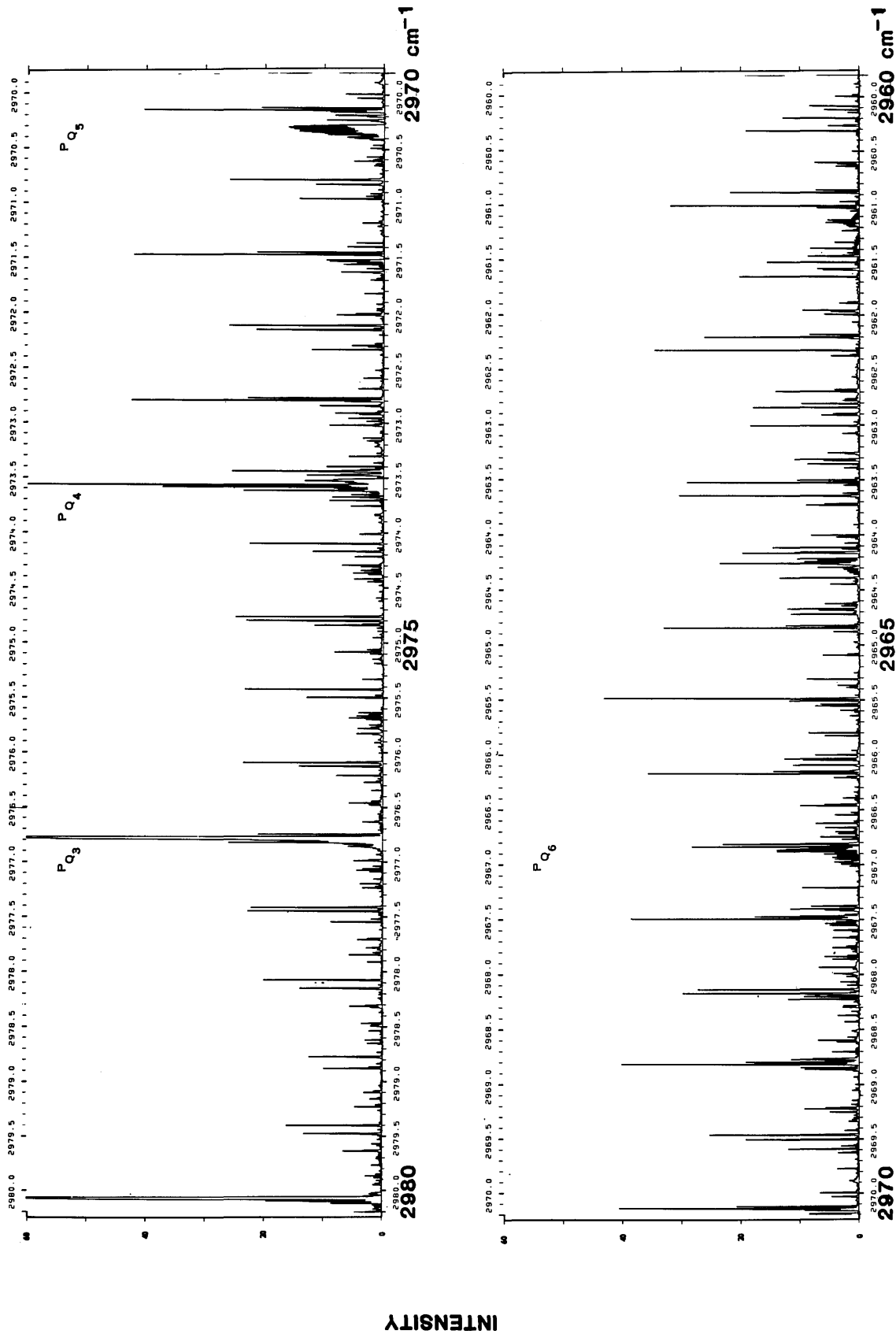


FIGURE 6. Continued

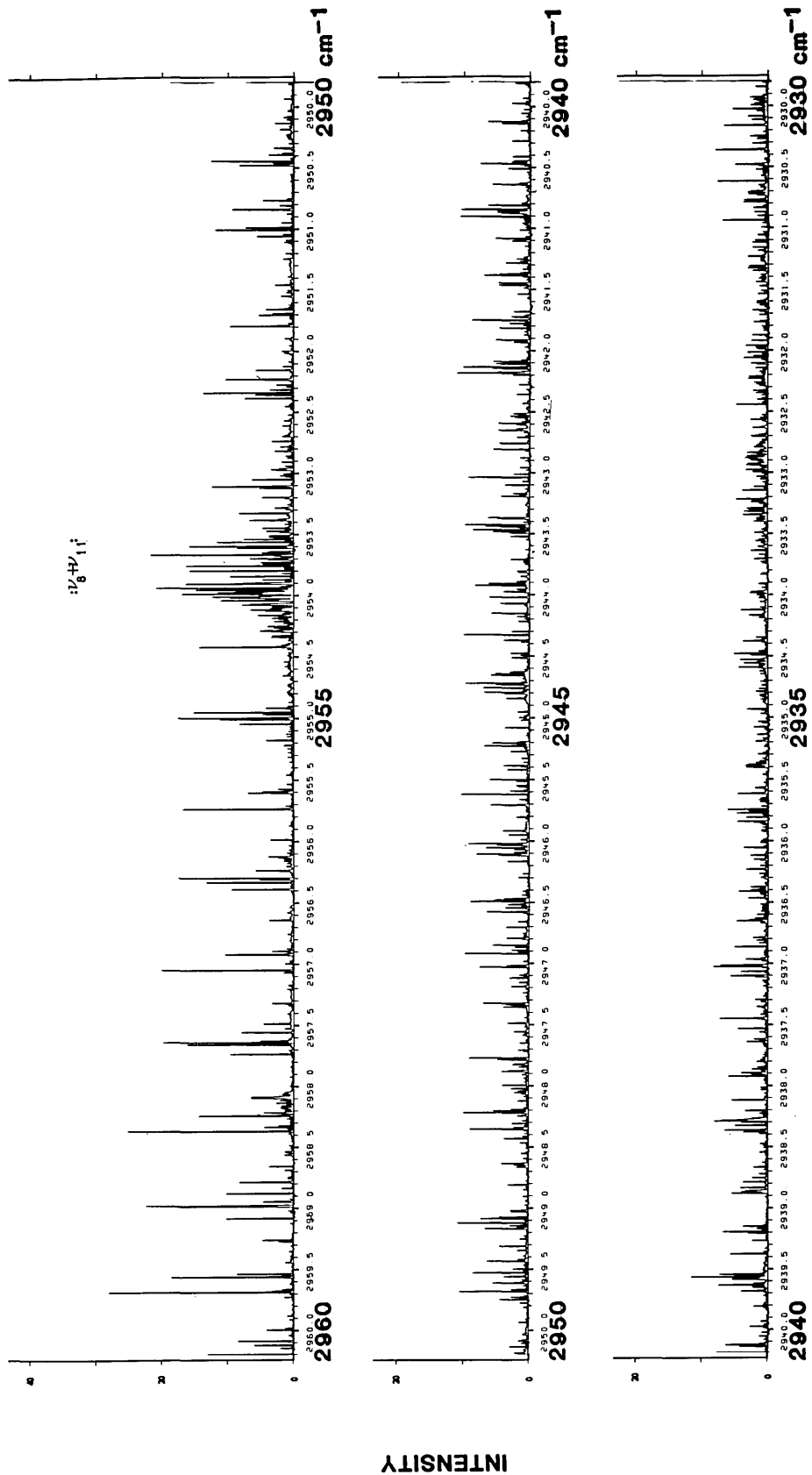


FIGURE 6. Continued

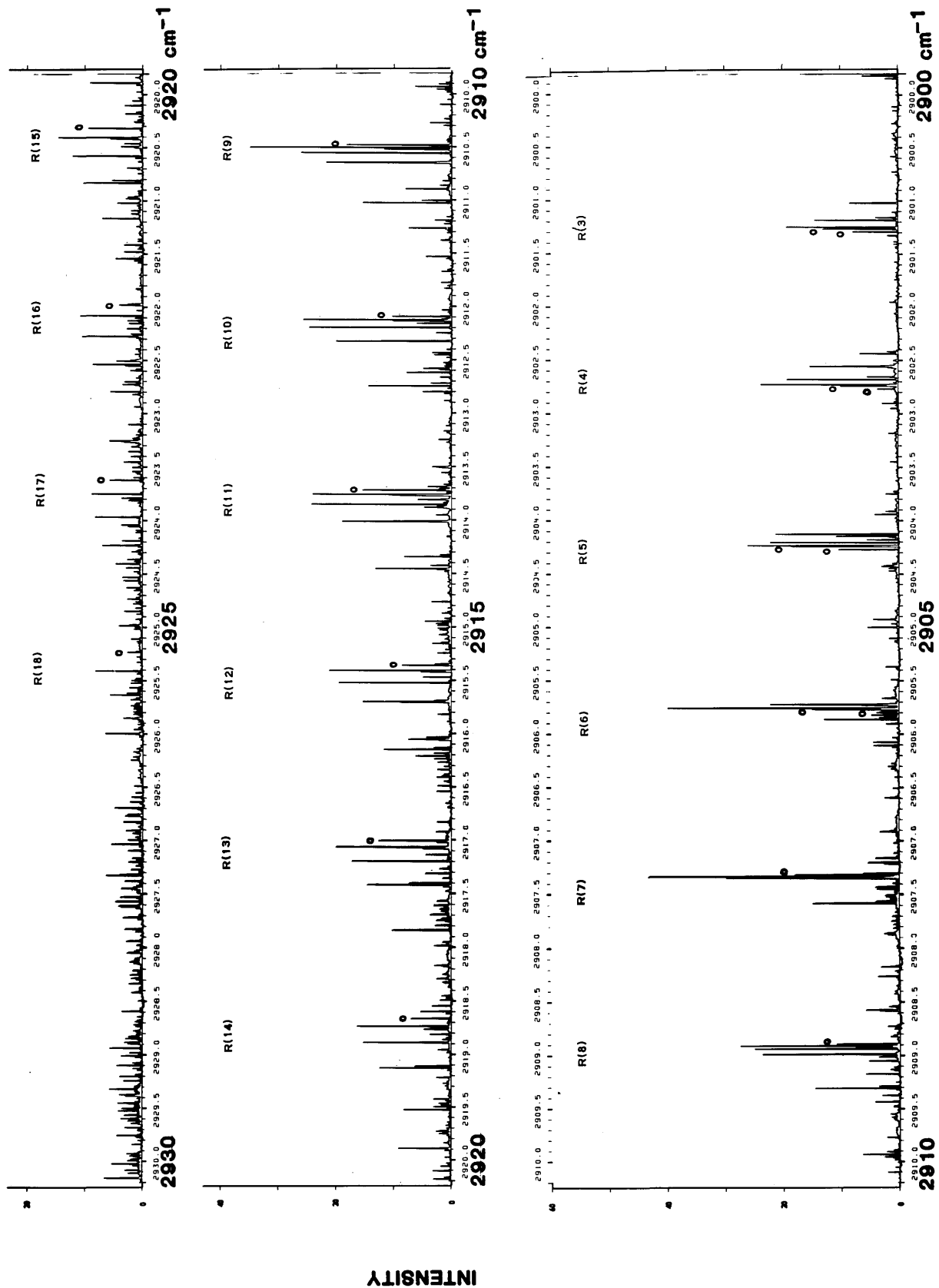


FIGURE 6. Continued

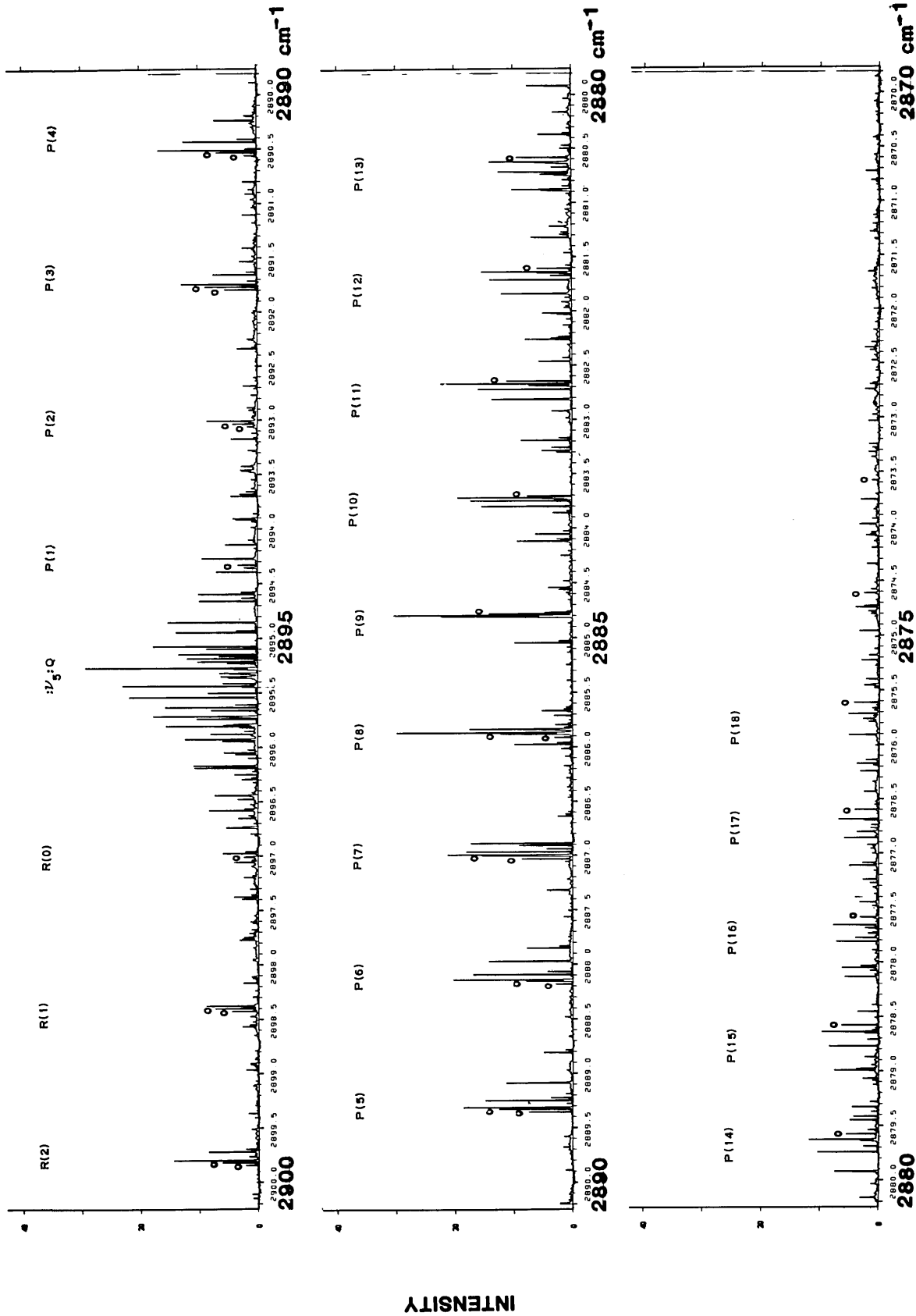


FIGURE 6. Continued











TABLE 2. continued

WAVELENGTH	INT	TRANSITION	STN	BAWD	E LOWER	WAVELENGTH	INT	TRANSITION	STN	BAWD	E LOWER
2875 7629	23 5					2871 2123	12 4				
2875 7720	9 2					2870 8206	11 8				
2875 7166	46 4	17 1 18 1	C	229 115		2870 7258	19 8	13 5 14 4	D	181 848	
2875 6660	10 2					2870 4183	9 0				
2875 6147	36 5	17 0 18 0	C	226 466		2869 8572	6 1	18 6 19 6 A1,2 C		347 694	
2875 6548	21 8	16 6 15 6 A1,2 C		235 106		2869 8607	2 2	18 6 19 6 E3,4 C		347 694	
2875 6478	12 1	14 6 15 6 E3,4 C		255 106		2869 5820	9 2				
2875 5900	19 2	18 6 19 6	C	294 293		2869 2293	11 4				
2875 2520	25 6	18 3 19 3 A1,2 C		275 401		2869 0962	15 2	14 5 15 4	D	201 703	
2875 1807	14 9	18 3 19 3 E3,4 C		275 401		2867 7530	9 7				
2874 9581	28 6	18 2 19 2	C	262 348		2867 6389	11 6				
2874 8036	11 9					2867 4641	14 9	15 5 16 4	D	222 875	
2874 7816	10 2					2866 5375	9 7				
2874 7802	15 9					2866 0385	10 9				
2874 7622	36 0	18 1 19 1	C	254 237		2865 8316	7 5	16 5 17 4	D	245 365	
2874 7288	21 8	13 5 14 5 G	C	205 881		2864 7715	8 7				
2874 6781	8 0	13 5 14 5 E1 C		205 881		2864 6353	14 4				
2874 6129	24 3	18 0 19 0	C	251 566		2864 4327	8 7				
2874 5785	12 9					2864 3029	8 7				
2874 3653	17 5	19 3 20 3 A1,2 C		302 036		2864 1960	12 2				
2874 1900	11 3	19 3 20 3 E3,4 C		302 036		2864 1133	9 7				
2874 0852	18 8	15 6 16 6 A1,2 C		276 278		2863 4629	9 9				
2874 0798	12 6	15 6 16 6 E3,4 C		276 278		2863 0641	8 5				
2874 0586	11 4					2863 0153	8 7				
2873 9876	28 1	13 5 12 4	D	146 098		2862 8202	9 9				
2873 9329	9 7										
2873 7563	26 1	18 1 20 1	C	280 673							
2873 5785	9 9	18 0 20 0	C	278 002							
2873 3648	10 9										
2873 3184	14 1										
2873 2785	8 9										
2873 2660	14 1	14 5 15 5	C	225 735							
2873 0337	15 8	20 3 21 2	C	318 433							
2872 9752	10 2										
2872 8855	8 4										
2872 8706	9 5										
2872 8576	8 7										
2872 7401	20 8	20 1 21 1	C	308 421							
2872 6940	13 9	16 6 17 6 A1,2 C		298 768							
2872 6816	9 7	16 6 17 6 E3,4 C		298 768							
2872 6747	13 4										
2872 5706	13 1										
2872 3581	20 9	12 5 13 4	D	163 313							
2872 3087	11 4										
2872 1935	8 5										
2871 8108	10 9	15 5 16 5	C	246 908							
2871 6566	16 4	21 1 22 1	C	337 483							
2871 2842	12 4	17 6 18 6 A1,2 C		322 573							
2871 2650	7 4	17 6 18 6 E3,4 C		322 573							
2871 2123	12 4										

6. References

[1] Cole, A. R. H.; Lafferty, W. J.; Thibault, R. J. J. *Mol. Spectrosc.* **29**, 365-374 (1969).  
 [2] Cole, A. R. H.; Cross, K.J.; Cugley, J. A.; Heise, H. M. J. *Mol. Spectrosc.* **83**, 233-244 (1980).  
 [3] Herzberg, G. *Infrared and Raman Spectra of Polyatomic Molecules*, D. Van Nostrand Co., New York, 1959, Chapter IV and V.  
 [4] Pitzer, K. S. *Dis. Faraday Soc.* **10**, 66-73 (1951).  
 [5] Pitzer, R. M. *Accounts of Chem. Res.* in press.  
 [6] Weiss, S.; Leroi, G. E. *J. Chem. Phys.* **48**, 962-967 (1967).  
 [7] Hirota, E.; Saito, S.; Endo, Y. *J. Chem. Phys.*  
 [8] Susskind, J. J. *Mol. Spectrosc.* **49**, 1-17 (1974).  
 [9] Wilson, E. B. J. *Chem. Phys.* **6**, 740-745 (1938).  
 [10] Patterson, C. W.; Flicker, H.; McDowell, R. S.; Nereson, N. *Mol. Phys.*  
 [11] Lafferty, W. J.; Hougen, J. T.; Valentin, A.; Henry, L.; Malathy-Devi, V.; Das, P. P.; Rao, K. N. 36th Symposium on Molecular Spectroscopy, Paper WE2, Columbus, Ohio, June 1981.  
 [12] Daunt, S. J.; Jennings, D. E.; Brault, J. W.; Susskind, J.; Reuter,

D.; Blass, W. E. 36th Symposium on Molecular Spectroscopy, Paper WE3, Columbus, Ohio, June 1981.  
 [13] Westcott, M. R. Alberta Research Council and Hinkley, E. D. Jet Propulsion Laboratory, private communication.  
 [14] Toth, R. A. Jet Propulsion Laboratory, private communication.  
 [15] Tokunaga, A. T.; Knacke, R. F.; Ridgway, S. T.; Wallace, L. *Astrophysical J.* **222**, 603-615 (1979).  
 [16] Pine, A. S. *J. Opt. Soc. Amer.* **64**, 1683-1690 (1974).  
 [17] Pine, A. S. *J. Opt. Soc. Amer.* **66**, 97-108 (1976).  
 [18] Pine, A. S. in *Laser Spectroscopy III*, (J. L. Hall and J. T. Carlsten, Eds.), pp. 376-381, Springer-Verlag, New York, 1977.  
 [19] Coulombe, M. J.; Pine, A. S. *Appl. Opt.* **18**, 1505-1512 (1979).  
 [20] Tarrago, G.; Dang-Nhu, M.; Poussigue, G.; Guelachvili, G.; Amiot, C. *J. Mol. Spectrosc.* **57**, 246-263 (1975).  
 [21] Hougen, J. T. *Can. J. Phys.* **42**, 1920-1937 (1964).  
 [22] Nakagawa, I.; Shimanouchi, T. *J. Mol. Spectrosc.* **39**, 255-274 (1971).  
 [23] Hougen, J. T. *J. Chem. Phys.* **38**, 1167-1173 (1963).  
 [24] Olson, W. B., private communication.  
 [25] Hougen, J. T. *J. Mol. Spectrosc.* **82**, 92-116 (1980).  
 [26] Lepard, D. W.; Shaw, D. E.; Welsh, H. L. *Can. J. Phys.* **44**, 2353-2362 (1966).

# Mechanism of the Electrical Conductivity in Potassium Croconate Violet

Lawrence M. Doane\*,† and Alexander J. Fatiadi\*

National Bureau of Standards, Washington, DC 20234

September 9, 1981

Based on crystallographic analysis and results of the solution electrochemistry, a mechanism for electron conduction is proposed.

Key words: conductivity; croconates; crystallographic; electrical; electrochemical; mechanism;  $\pi$ -acceptors; semiconduction.

## 1. Introduction

The search for non-metallic electrical conductors has brought about the synthesis of organic compounds that ordinarily are not thought of as good electrical conductors. For example, ionic crystals [1]<sup>1</sup> and polymeric solids [2] have been made to behave as good conductors. Among the best-conducting organic materials synthesized are the charge-transfer salts based on the tetrathiofulvalene (TTF)-tetracyanoquinodimethene (TCNQ) skeleton [1,3]. In an effort to make additional complexes of higher electrical conductivity, many new donors and acceptors have been prepared. The pseudo-oxocarbon croconates are examples of new  $\pi$ -electron acceptors that behave as typical semiconductors and exhibit good conductivity when complexed with TTF [4]. We have reported the solution electrochemistry of several croconate salts in *N,N*-dimethylformamide (DMF) [5] and in a preliminary communication [6] we briefly discussed an electron conduction mechanism for crystalline croconate salts. Based on crystallographic analysis [7] and results of the solution electrochemistry [5] a detailed conduction mechanism for potassium croconate violet is proposed in this paper.

## 2. Discussion

A general feature of crystalline non-metallic conductors is the formation of molecular stacks in which interplanar separations are van der Waals distances (ca.

3.5 Å) [8]. The assumption made is that within this distance the molecular geometry in the stack favors intermolecular orbital overlap. This overlap forms the bridge which permits electron transfer between the molecules of the stack. Generally, the bridgeheads are redox centers. For our purposes, points of closest approach are intermolecular atomic sites that are potentially electrochemically active and are separated by no more than a van der Waals distance. Points of closest approach are therefore the bridgeheads from which intermolecular electron conduction starts or terminates.

### 2.1 Anionic crystal structure

Potassium croconate violet crystallizes with triclinic symmetry [7]. The cyclopentene rings form stacks parallel to the *a*-axis with an angle of approximately 32° formed between the plane defined by the cyclopentene ring (ring plane) and the *a*-axis. A portion of the stack illustrating the two rings of the unit cell along with the rings directly above and below the unit cell are shown in figure 1. Within the unit cell, the perpendicular separation between ring planes is 3.32 Å. However, the perpendicular distance between adjacent ring planes of separate but adjoining unit cells is 3.42 Å. In addition, adjacent rings are rotated approximately 180° to the axis of the stack. This rotation is shown clearly in figure 2a,b, in which projections normal to the ring plane are illustrated.

### 2.2 Points of closest approach

By viewing ring projections normal to the ring plane, overlapping atomic sites are selected as possible points of closest approach. The atomic sites considered are those

\*Center for Analytical Chemistry, National Measurement Laboratory.

†Present address: IBM Corporation, Dept. 323, Bldg. 970, Essex Jct, VT 05452.

<sup>1</sup>Figures in brackets indicate literature references at the end of this paper.

that exhibit electrochemical activity. From the solution electrochemistry of potassium croconate violet [5], the dicyanomethylene groups and the alkene bond have been shown to be electrochemically active. It is clear

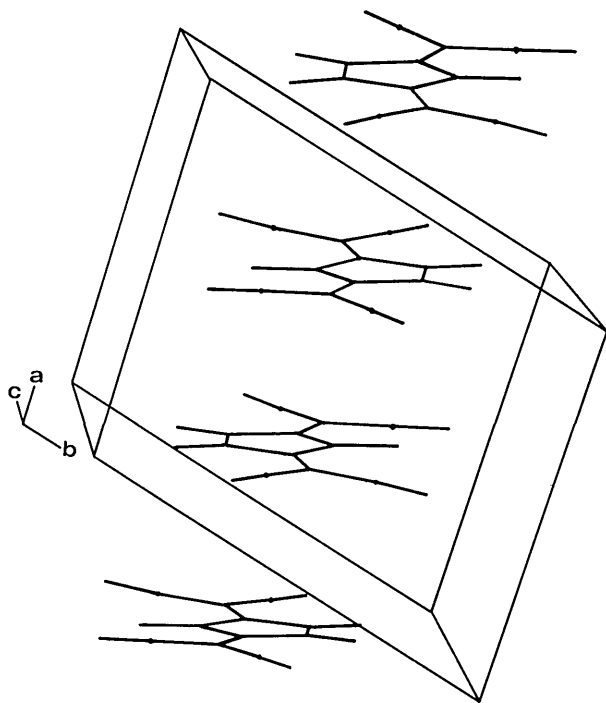


FIGURE 1. View of anionic stack of crystalline potassium croconate violet.

from figure 2b that in adjacent rings of separate but adjoining unit cells there is overlap of the dicyanomethylene group of one ring with one of the ring carbon atoms that forms the alkene bond in the other ring (indicated by an asterisk). Similar overlap of adjacent rings within the unit cell is impossible (see fig. 2a). However, overlap of the dicyanomethylene groups of opposing rings is possible. From crystallographic data, atomic distances were determined for the atoms designated by the asterisk in figure 2a,b. The distances of closest approach, shown in figure 3, are within the van der Waals distance (3.5 Å).

### 2.3 Proposed electron conduction mechanism

The solution electrochemistry of croconate violet [5] shows that the only reversible electrochemical reaction occurring in the molecule is the redox process at the 4,5-alkene bond. Although in solution electrochemistry the solvation sheath can change significantly after an electron transfer, a general feature of reversible electrochemical processes is the molecule undergoing electron gain or loss changes little structurally. It is apparent then that electron transfer must be initiated and terminated at the alkene bond, since this is the only redox process that leaves the molecule structurally unaltered. In the crystalline croconate salt charge migration may also be considered to proceed from one molecule to another by reversible electron transfer at the alkene bond.

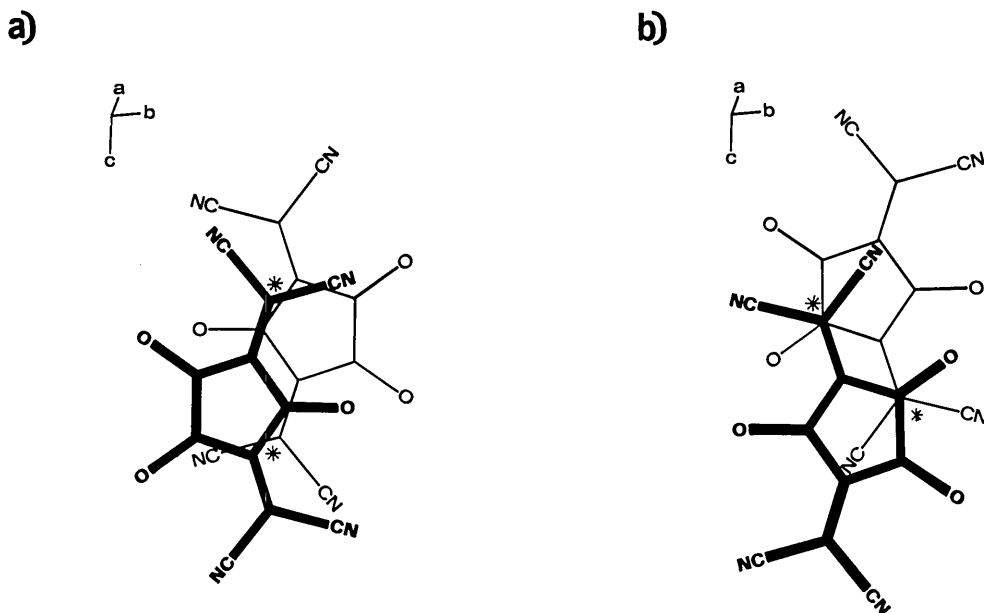


FIGURE 2. View of projections (normal to the ring plane) of potassium croconate violet: (a) the ring pair within the unit cell and (b) adjacent ring pair of separate but adjoining unit cells. The heavy-lined ring designates the upper of the two croconates. The asterisks designate redox centers of potential overlap.

Electron migration in crystalline croconate violet is rationalized in the following manner. Consider the stacking arrangement in figure 4 where the cyclopentene rings are parallel and adjacent rings are rotated approximately  $180^\circ$  to the axis of the stack. The two cyclopentene rings that define the unit cell have their dicyanomethylene groups nearly opposite each other (see fig. 2a). The adjacent ring of the next unit cell is shifted slightly so that one of the dicyanomethylene groups of each ring is opposite the alkene bond of the other ring (see fig. 2b). Electron migration would therefore occur between a di-

cyanomethylene group and the alkene bond of adjacent unit cells and between dicyanomethylene groups within the unit cell as illustrated in figure 4. But, based on the solution electrochemistry of croconate violet the dicyanomethylene group cannot transfer an electron reversibly. However, two rationales can be invoked to explain electron conductivity within the dicyanomethylene group:

(i) Suppose we consider electron movement within the dicyanomethylene group to be a concerted process.

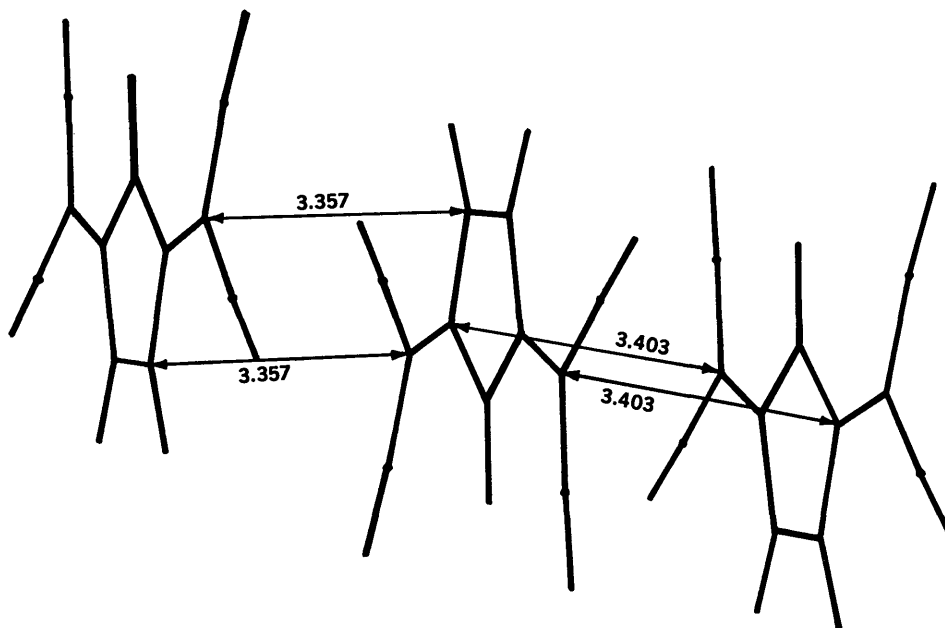


FIGURE 3. View of three stacked croconates indicating atomic distances ( $\text{\AA}$ ) of centers of closest approach.

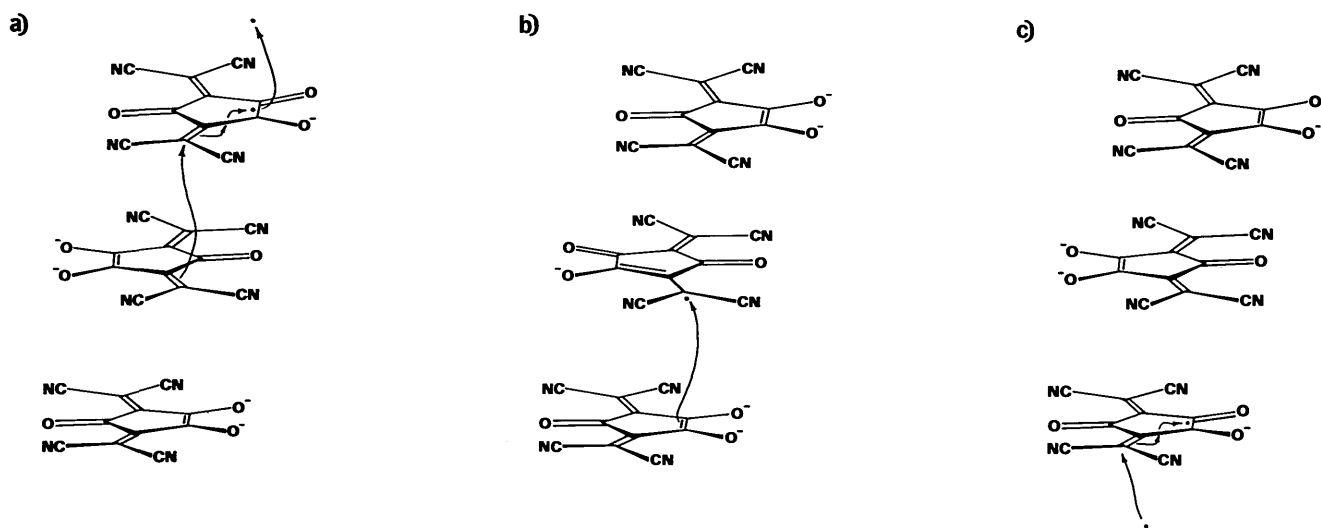


FIGURE 4. Views of three stacked croconates showing proposed: (a) initial electron abstraction and intermolecular electron conduction between dicyanomethylene groups, (b) intermolecular electron conduction between the alkene carbon atom and the dicyanomethylene group (shown as a resonance from here), and (c) intramolecular electron conduction between the alkene carbon atom and dicyanomethylene group.

In this case an electron is injected into one end of the dicyanomethylene group as another electron is simultaneously abstracted from the other end of the dicyanomethylene group. The dicyanomethylene group could then be considered not to have undergone a redox process.

(ii) Resonance structures for the radical anion can be written (Fig. 5) where the dicyanomethylene group participates in delocalizing the unpaired electron. In this case the dicyanomethylene group can participate in intramolecular electron movement in either croconate oxidation state without participating in the actual redox process.

Invoking either explanation for electron conduction within the dicyanomethylene group does not alter the conduction process. The effect is to make the dicyanomethylene group the conduction arm of the molecule while the alkene bond provides the redox mechanism.

One additional comment is in order: since resonance forms can be written for both the dianion and radical anion, there appears to be no migration of resonance in the stack. Mixed valency is therefore not a requisite of electron migration in crystalline croconate violet as has been suggested for other organic conductors. [1].

The authors wish to thank Drs. Alan D. Mighell and William T. Yap for their assistance in obtaining the crystallographic projections and Pam Leech for the artwork.

### 3. References

- [1] Perlstein, J. P. *Angew. Chem., Int. Ed. Engl.*, **16** (1977) 519.
- [2] Nigrey, P. J.; MacDiarmid, A. G.; Heeger, A. J. *J. C. S. Chem. Commun.* (1979) 594.
- [3] Ferraris, J. P.; Cowan, D. O.; Walatka, V.; Perlstein, J. P. *J. Am. Chem. Soc.*, **95** (1973) 948; L. B. Coleman, M. J. Cohen, D. J. Sandman, F. G. Yamagishi, A. F. Garito, and A. J. Heeger, *Solid State Commun.*, **12** (1973) 1125.
- [4] Fatiadi, A. J.; in R. West (Ed.), *Oxocarbons*, Academic Press, New York, 1980, Ch. 4.
- [5] Doane, L. M.; Fatiadi, A. J., *J. Electroanal. Chem.* **135** (1982) 193.
- [6] Doane, L. M.; Fatiadi, A. J. *Agnew. Chem.* (in press).
- [7] Hines, V. L.; Mighell, A. D.; Hubbard, C. R.; Fatiadi, A. J. *J. Res. Natl. Bur. Stand.*, **85** (2): 87-97, (1980 March-April).
- [8] Soos, Z. G.; Klein, D. L. in R. Foster (Ed.), *Molecular Association*, Academic Press, New York, 1975, Ch. 1.

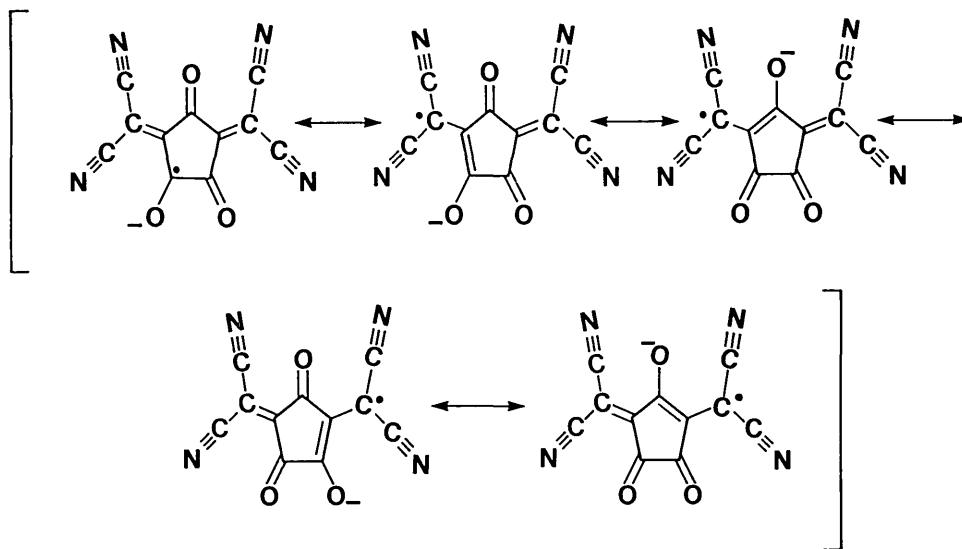


FIGURE 5. Several possible resonance forms of the croconate violet radical anion.